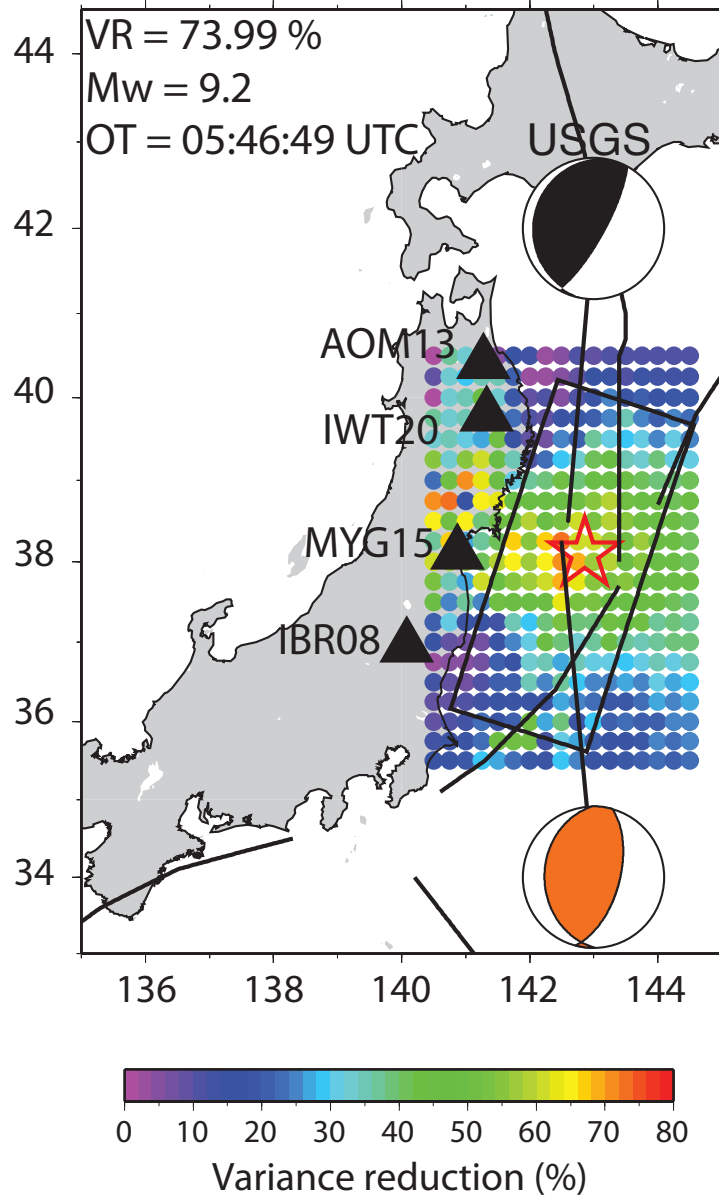


# Berkeley Seismological Laboratory



**Annual Report**  
**July 2010 - June 2011**



**Berkeley Seismological Laboratory**  
**Annual Report**  
**July 2010 - June 2011**

### Cover Picture

From Research Section 6: Rapid characterization of great subduction zone earthquakes, such as the 2011 M9.0 Tohoku-oki, Japan, event, is vital for quickly assessing the likelihood of tsunami generation. We have developed an approach, called GridMT, that continuously scans a grid of possible sources along the subduction zone surface.

When energy arrives at the seismic stations it is used to estimate the location, size and mechanism of the earthquake. We applied it to the 2011 Tohoku-oki earthquake. This figure shows a map of virtual sources distributed along the slab. They are color-coded by the best variance reductions (VR) that are obtained from the continuous moment tensor analysis of long-period (100-200 sec) strong-motion data recorded at four K-NET stations (triangles).

The best GridMT solution (Mw9.2 and VR=73.99)

# Contents

<b>1</b>	<b>Director's Report</b>	<b>1</b>
1	Introduction . . . . .	1
2	History and Facilities . . . . .	2
3	BSL Staff News . . . . .	3
4	Acknowledgements . . . . .	4
<b>2</b>	<b>Research Studies</b>	<b>5</b>
1	ElarmS Earthquake Early Warning . . . . .	6
2	ShakeAlert: A Unified EEW System for California . . . . .	8
3	Validation of Coda-derived Source Parameters using Strong and Weak Ground Motion Records of the 2008 Wells, Nevada Sequence . . . . .	10
4	Quantitative Analysis of Coda Window Length: How Much Length of Coda is Enough for Stable Amplitudes? . . . . .	12
5	Source Characterization of Mendocino Offshore Earthquakes for Improvements in Monitoring Active Deformation and Estimates of Earthquake Potential in the Mendocino Triple Junction Region . . . . .	14
6	Detecting the 2011 M9.0 Tohoku Earthquake with Moment Tensors . . . . .	16
7	Time-Lapse Monitoring for Detection of Transient Stress Changes in Geysers Geothermal Field . . . . .	18
8	Measuring Fault-Zone Rheology at Depth from Characteristically Repeating Earthquakes . . . . .	20
9	Free-Surface Vanishing Traction Effects on Shallow Sources . . . . .	22
10	Moment Tensors for Aftershocks of the M 7.9 Wenchuan Earthquake . . . . .	24
11	Focal Depth of the 2008 Panzhihua Earthquake from Depth Phase sPL and Joint Inversion of Local and Teleseismic Waveforms . . . . .	26
12	Deviatoric Moment Tensor Analysis at The Geysers Geothermal Field . . . . .	28
13	Slip Transients, Deficit and Release from Repeating Earthquakes . . . . .	30
14	Immediate Triggering of Small Repeating Earthquakes at Parkfield . . . . .	32
15	Joint Inversion of Seismic and Geodetic Data for the Source of the 4th March 2010 $M_w$ 6.3 Jia-Shian, SW Taiwan, Earthquake . . . . .	34
16	Tidal Triggering of LFEs near Parkfield, CA . . . . .	36
17	TremorScope: Imaging the Deep Workings of the San Andreas Fault . . . . .	38
18	Search for Transient Deformation Following an Earthquake Sequence near San Juan Bautista . . . . .	40
19	Probing the Deep Rheology of Tibet: Constraints from 2008 $M_w$ 7.9 Wenchuan, China Earthquake . . . . .	42
20	Joint Seismic and Geodetic Analysis of the 2009 Padang, Sumatra Intraslab Earthquake . . . . .	44
21	Rapid Detection of Large Earthquakes Using Quasi-Finite-Source Green's Functions in Moment Tensor Analysis . . . . .	46
22	Identifying Undetected Early Aftershocks Associated with the 12 August 1998 $M_w$ 5.1 San Juan Bautista Earthquake . . . . .	48
23	Persistent Scatterer InSAR Analysis of Berkeley Hills Landslides . . . . .	50
24	Toward Global Waveform Tomography with the SEM: Improving Upper-Mantle Images at Shallow Depths . . . . .	52
25	On the Interpretation of SKS Splitting Measurements in the Presence of Several Layers of Anisotropy . . . . .	54
26	Anisotropic Stratification in the Continental Upper Mantle . . . . .	56
27	Refining the Cratonic Upper Mantle Using RegSEM . . . . .	58
28	Investigating Upper Mantle Discontinuities Beneath Subduction Zones . . . . .	60
29	Small-scale Variation of SS Precursors Observed by US Transportable Array . . . . .	62
30	Investigation of Cascadia Segmentation with Ambient Noise Tomography . . . . .	64

31	Characterization of the Pacific Superplume Boundary . . . . .	66
32	An Automated Despiking Algorithm for Seismic Normal Mode Data . . . . .	68
33	Seismic Imaging of the San Andreas Fault in Northern California using Receiver Functions . . . . .	70
<b>3</b>	<b>BSL Operations</b>	<b>73</b>
1	Berkeley Digital Seismic Network . . . . .	75
2	California Integrated Seismic Network . . . . .	85
3	Northern Hayward Fault Network . . . . .	90
4	Parkfield Borehole Network (HRSN) . . . . .	99
5	Bay Area Regional Deformation Network . . . . .	110
6	Northern California Earthquake Data Center . . . . .	115
7	Data Acquisition and Quality Control . . . . .	125
8	Northern California Earthquake Monitoring . . . . .	135
9	Outreach and Educational Activities . . . . .	141
	<b>Glossary</b>	<b>143</b>
	<b>Appendix I Publications, Presentations, Awards, and Panels 2010-2011</b>	<b>145</b>
	<b>Appendix II Seminar Speakers 2010-2011</b>	<b>157</b>
	<b>Appendix III Organization Chart 2010-2011</b>	<b>159</b>

# Chapter 1

## Director's Report

### 1 Introduction

As in previous years, I am pleased to introduce the 2010-11 Berkeley Seismological Laboratory Annual Report, the last one under my tenure as BSL director. This report covers two coupled activities at BSL: basic research and real-time earthquake monitoring operations. Chapter 2 describes the research accomplishments; Chapter 3 details progress in our development of infrastructure and facilities.

The basic research spans many topics in seismology and tectonics. They range from studies of the earth's deep structure and dynamics to various aspects of earthquake physics; from microearthquakes and tremor studies to studies of earthquake mechanisms and rupture spanning different time scales; and from slow tectonic deformation to real-time seismology and earthquake early warning. These are described in 32 "two-pager" contributions in Chapter 2 of this report.

A highlight of this year has been the participation of BSL scientists in a symposium: "Earthquakes, Tsunamis, and Nuclear Fallout: Is California at Risk Like Japan?" hosted by the Berkeley Institute for the Environment, the Department of Earth and Planetary Science, the Berkeley Seismological Laboratory, and the Pacific Earthquake Engineering Research Center following the March 11, 2011 disastrous M9 Great Tohoku earthquake. The BSL also hosted a successful Earthquake Early Warning Summit on April 4-5, 2011, in response to the increased interest in real-time earthquake information and early warning specifically following the Japan earthquake.

Another highlight of this year is the funding by the Gordon and Betty Moore Foundation of "Tremorscope," a program which aims at understanding deep tremor activity on the San Andreas Fault near Parkfield, right below the nucleation zone of the great 1857 Fort Tejon ("Los Angeles") earthquake. The program includes the deployment of eight stations, of which four will be in boreholes, centered on the tremor source.

On the operational side of the BSL, owing to significant funding received through the USGS in the framework of the American Recovery and Reinvestment Act (ARRA),

the focus has been on upgrading the recording systems at many of our broadband and borehole stations. These upgrades were much needed, as many of the recording systems were more than 15 years old, well beyond the expected lifetime of computer hardware. At the time of the writing of this report, we have completed the upgrade of our broadband stations with state of the art Quanterra Q330 data loggers, while the upgrade of our borehole stations with Kinometrics BASALT data loggers is well under way. We also received funding to upgrade receivers at our 29 BARD stations and to add GPS receivers at 7 of our BDSN stations. The new receivers allow us to stream high rate (1 Hz sampling) GPS data and to start implementing the use of GPS data in our real-time earthquake analysis procedures. At the time of this report, 12 stations have been upgraded with TopCon receivers. When these receivers were originally delivered, they did not have all the needed functionalities for smooth remote real-time continuous operation. It took many months of tests and iterations with the manufacturer to get them to work to our satisfaction. Given these difficulties, the USGS approved a six month extension on this ARRA grant. The work will be completed by the end of December, 2011. Notwithstanding this situation with upgrades, all BARD stations have been streaming 1 Hz continuous data since December 2010. These data are available through the recently redesigned BARD webpage at the Northern California Earthquake Data Center (NCEDC).

The joint BSL/USGS earthquake notification system had been redesigned in previous years. The new integrated Northern California Earthquake Management Center (NCEMC) has now been in operation for two years. We had an opportunity to thoroughly test the robustness of the new AQMS software on two occasions: (1) when the USGS component of our joint system was shut down for a test of the USGS power system and (2) when upgrades to Warren Hall at UC Berkeley impacted the operations of the Berkeley component. In both cases, all operations were transferred seamlessly to the single operational component for the duration of the disturbance.

The redesign of the STS-1 very broad band seismometer under Metrozet's leadership has been completed, with

funding from the NSF EAR-Instruments and Facilities Program. The M9 03/11/2011 Tohoku (Japan) earthquake was well recorded on the entire BDSN network as well as at test sites for the new STS-1's at Harvard (HRV) and the Albuquerque Seismological Laboratory, providing an opportunity to confirm the superior performance of the new instruments at very low frequencies.

The following sections give a brief historical overview of the BSL, and finally some BSL staff news.

## 2 History and Facilities

The Berkeley Seismological Laboratory (BSL), formerly the Berkeley Seismographic Stations (BSS), is the oldest Organized Research Unit (ORU) on the UC Berkeley campus. Its mission is unique in that, in addition to research and education in seismology and earthquake-related science, it is responsible for providing timely information on earthquakes (particularly those that occur in Northern and Central California) to the UC Berkeley constituency; to the general public; and to various local and state governments, and private organizations. The BSL is therefore both a research center and a facility/data resource, which sets it apart from most other ORUs. A major component of our activities is focused on developing and maintaining several regional observational networks, and participating, along with other agencies, in various aspects of the collection, analysis, archival, and distribution of data pertaining to earthquakes, while maintaining a vigorous research program on earthquake processes and Earth structure. In addition, the BSL staff spends considerable time on public relations activities, including tours, talks to public groups, response to public inquiries about earthquakes, and World-Wide-Web presence (<http://seismo.berkeley.edu/>).

UC Berkeley installed the first seismograph in the Western Hemisphere at Mount Hamilton (MHC) in 1887. Since then, it has played a leading role in the operation of state-of-the-art seismic instruments and in the development of advanced methods for seismic data analysis and interpretation. Notably, the installation, starting in 1927, of Wood-Anderson seismographs at four locations in Northern California (BKS, ARC, MIN, and MHC) allowed the accurate determination of local earthquake magnitude ( $M_L$ ) from which a unique historical catalog of regional earthquakes has been maintained to this day, providing crucial input to earthquake probabilities studies.

Over the years, the BSS continued to keep apace of technological improvements. The first centrally telemetered network using phone lines in an active seismic region was installed by BSS in 1960. The BSS was the first institution in California to operate a 3-component "broadband" system (1963). It played a major role in

the early characterization of earthquake sources using "moment tensors" and source-time functions. The BSS also made important contributions to the early definitions of detection/discrimination of underground nuclear tests and, jointly with UCB Engineering, to earthquake hazards work. Starting in 1986, the BSS acquired four state-of-the-art broadband instruments (STS-1), while simultaneously developing PC-based digital telemetry, albeit with limited resources. As telecommunication and computer technologies made rapid progress, in parallel with broadband instrument development, paper record reading was completely abandoned in favor of largely automated analysis of digital data.

The current facilities of BSL have been built progressively over the last two decades, with efforts initiated by significant "upgrade" funding from UC Berkeley in 1991-1995. The BSL currently operates and acquires data, continuously and in real time, from over 60 regional observatories. These house a combination of broadband and strong motion seismic instrumentation installed in vaults, borehole seismic instrumentation, the permanent GPS stations of the Bay Area Regional Deformation (BARD) network, and electromagnetic sensors. The seismic data are fed into the BSL real-time processing and analysis system. Since 1996, they are used in conjunction with data from the USGS Northern California Seismic Network (NCSN) in the joint earthquake notification program for Northern California. This program capitalizes on the complementary capabilities of the networks operated by each institution to provide rapid and reliable information on the location, size and other relevant source parameters of regional earthquakes. In recent years, a major emphasis in BSL instrumentation has been in densifying the state-of-the-art seismic and geodetic networks. At the same time, research efforts have been directed toward the development of robust methods for quasi-real time, automatic determination of earthquake source parameters and predicted strong ground motion, using a sparse network combining broadband and strong motion seismic sensors, as well as permanent geodetic GPS receivers. Recently, research emphasis has been directed toward the development of "earthquake early warning" capabilities.

The Berkeley Digital Seismic Network (BDSN), a regional network of 32 digital broadband and strong motion seismic stations with continuous telemetry to UC Berkeley, is the backbone of the BSL operations. This network contributes basic regional data for real-time estimation of location, size and rupture parameters for earthquakes in Central and Northern California. It is the Berkeley contribution to the California Integrated Seismic Network (CISN). In June 2009, our operational software, the Rapid Earthquake Data Integration (REDI) program, was replaced by the CISN, now AQMS, software (see Chapter 3, Operational Section 8). The data

from the BDSN also provide a fundamental database for the investigation of three-dimensional crustal structure and its effects on regional seismic wave propagation. This is ultimately crucial for estimating ground shaking for future earthquakes. Most stations also record auxiliary temperature/pressure channels, valuable in particular for background noise quality control. Complementing this network is a  $\sim 25$  station “high-resolution” network of borehole seismic sensors located along the Hayward Fault (HFN) and under the Bay Area bridges, operated jointly with the USGS/Menlo Park and linked to the Bridge Safety Project of the California Department of Transportation (Caltrans). The latter has facilitated the installation of sensor packages at 15 bedrock boreholes along 5 East Bay bridges in collaboration with Lawrence Livermore National Laboratory (LLNL). A major science goal of this network is to collect high signal-to-noise data for micro-earthquakes along the Hayward Fault to gain insight into the physics that govern fault rupture and its nucleation. The BSL also operates and maintains the 13 element Parkfield borehole seismic array (HRSN). This array provides high quality data on micro-earthquakes, clusters and, most recently, tremors, and is an important reference for the San Andreas Fault Observatory at Depth (SAFOD). Since April 2002, the BSL collaborates with MBARI on the operation of a permanent broadband ocean bottom station, MOBB.

In addition to the seismic networks, the BSL operates, maintains and processes data from the 26 permanent geodetic stations of the BARD Network. It archives and distributes this data as well. Where possible, BARD sites are collocated with BDSN sites to minimize telemetry costs. In particular, all sites have now been upgraded to 1 Hz sampling. This supports one focus of BSL research, the development of analysis methods which combine seismic and geodetic data to rapidly estimate source parameters of significant earthquakes.

Finally, two of the BDSN stations (PKD, SAO) also share data acquisition and telemetry with 5-component electromagnetic sensors installed with the goal of investigating the possibility of detection of tectonic signals. In 2002-2003, automated quality control software was implemented to monitor the electromagnetic data.

Archival and distribution of data from these and other regional networks is performed at the Northern California Earthquake Data Center (NCEDC), operated at the BSL in collaboration with USGS/Menlo Park. The data reside on a mass-storage device (current holdings  $\sim 58$  terabytes), and are accessible online over the Internet (<http://www.ncedc.org>). Among others, data from the USGS Northern California Seismic Network (NCSN), are archived and distributed through the NCEDC. The NCEDC also maintains, archives and distributes the ANSS earthquake catalog.

Core University funding to our ORU has until now

provided salary support for one staff scientist and several technical and administrative staff members, representing about 30% of the total infrastructure support. The remaining support comes from extramural grants and contracts, primarily from the USGS, the NSF, and the State of California, through its Emergency Management Agency (CalEMA, formerly OES). We acknowledge valuable recent contributions from other sources such as Caltrans and PEER, as well as our Earthquake Research Affiliates. The effects of drastic budget cuts in FY09-10 are temporarily being offset by ARRA funding from the USGS.

### 3 BSL Staff News

Changes in BSL staff in 2010-11 are as follows.

In the past year, none of the graduate students associated with BSL completed their PhD’s.

One new graduate student, Andrea Chiang, joined the BSL as a graduate student in the fall of 2010. We also have one new post-doc, Seung-Hoon Yoo.

BSL hosted a number of visiting scientists and students in 2010-11. Ruiqing Zhang joined us from the Chinese Earthquake Administration in Beijing, China. Visiting graduate students included Xiangdong Lin, from the Beijing Earthquake Administration and graduate student at the Institute of Geophysics of the China Earthquake Administration; and Jiajun Chong, from the University of Science and Technology in China. In January, Ling Lei returned to School of Electronic and Information Engineering (EIE) at Beihang University to complete her Ph.D. Matt Wilks, an undergraduate at Imperial College London, spent the academic year at the BSL. Matthias Obrebski left his post-doc position at the BSL to join IFREMER Brest in France, while another post-doc, Paul Cupillard, is now at now a post-doctoral researcher in the Institute de Physique du Globe de Paris seismology group.

There have been major changes in the administration of the BSL: Kate Lewis left in January 2011 to work for SPO. Following a year under Research Enterprise Services (RES), BSL administration has now been regrouped in a joint EPS/BSL administrative unit headed by Earth and Planetary Science Department (EPS) Manager Judith Coyote. The administrative functions are now coordinated between the two units, with Dawn Geddes taking on the responsibility of the BSL operational budget and its associated grants and contracts and Raluca Iordache and Clarissa Foreman taking on the research grant administration for BSL PIs. Micaelee Ellswythe now assists PI Romanowicz with administrative tasks related to the CIDER program. Two new members of the EPS/BSL administrative team have joined Dawn in the BSL administrative office: Marion Banks, who started in May 2011 and is in charge of reception and travel, and Matt

Carli, who started in June 2011 and deals with purchasing. Owing to Judith's efforts, the reorganization is now complete and we are finally able to resume smooth administrative operations.

There have also been significant changes in the field engineering staff at the BSL. Rick Lellinger and Jarrett Gardner left mid-year, accepting job offers at LBNL and from a private company, respectively. Since then, assistant engineers Josh Miller and Aaron Enright have joined the team. Finally, John Friday retired in June 2011. We miss him and hope he will come back part time this fall!

In the IT team, Oleg Khainovsky left in January 2011, and Ivan Henson joined the team in April 2011, to work on software development for the Earthquake Early Warning project and the CISN.

Tom Weldon joined the research staff in January 2011.

The greater BSL family has continued to grow in the past year, when baby Roger Brown was born to Holly Brown and her husband Tom in December 2010.

## 4 Acknowledgements

I wish to thank our technical and administrative staff, scientists and students for their efforts throughout the year and their contributions to this annual report. Individual contributions to activities and report preparation are mentioned in the corresponding sections, except for the appendix sections, which were prepared by Jennifer Taggart.

I also wish to specially thank the individuals who have regularly contributed to the smooth operation of the BSL facilities: Mario Aranha, Doug Dreger, Aaron Enright, John Friday, Jarrett Gardner, Peggy Hellweg, Ivan Henson, Ingrid Johanson, Bill Karavas, Oleg Khainovski, Rick Lellinger, Josh Miller, Pete Lombard, Rick McKenzie, Bob Nadeau, Doug Neuhauser, Charley Paffenbarger, Jennifer Taggart, Taka'aki Taira, Stephen Thompson, Bob Uhrhammer, Tom Weldon, and Stephane Zuzlewski, and, in the administrative office, Marion Banks, Matt Carli, Judith Coyote, Dawn Geddes, Kate Lewis, and Gretchen vonDuering. I also wish to thank our undergraduate assistants, Chris Rawles, David Tang, Landon Turner, Ryan Turner, and Tam Visher, for their contributions to our research and operations activities.

I am particularly grateful to Jennifer Taggart and Peggy Hellweg for their help in putting together this annual report and bringing it to completion.

The Annual Report of the Berkeley Seismological Laboratory is available on the Web at [http://seismo.berkeley.edu/annual\\_report](http://seismo.berkeley.edu/annual_report).

# Chapter 2

## Research Studies

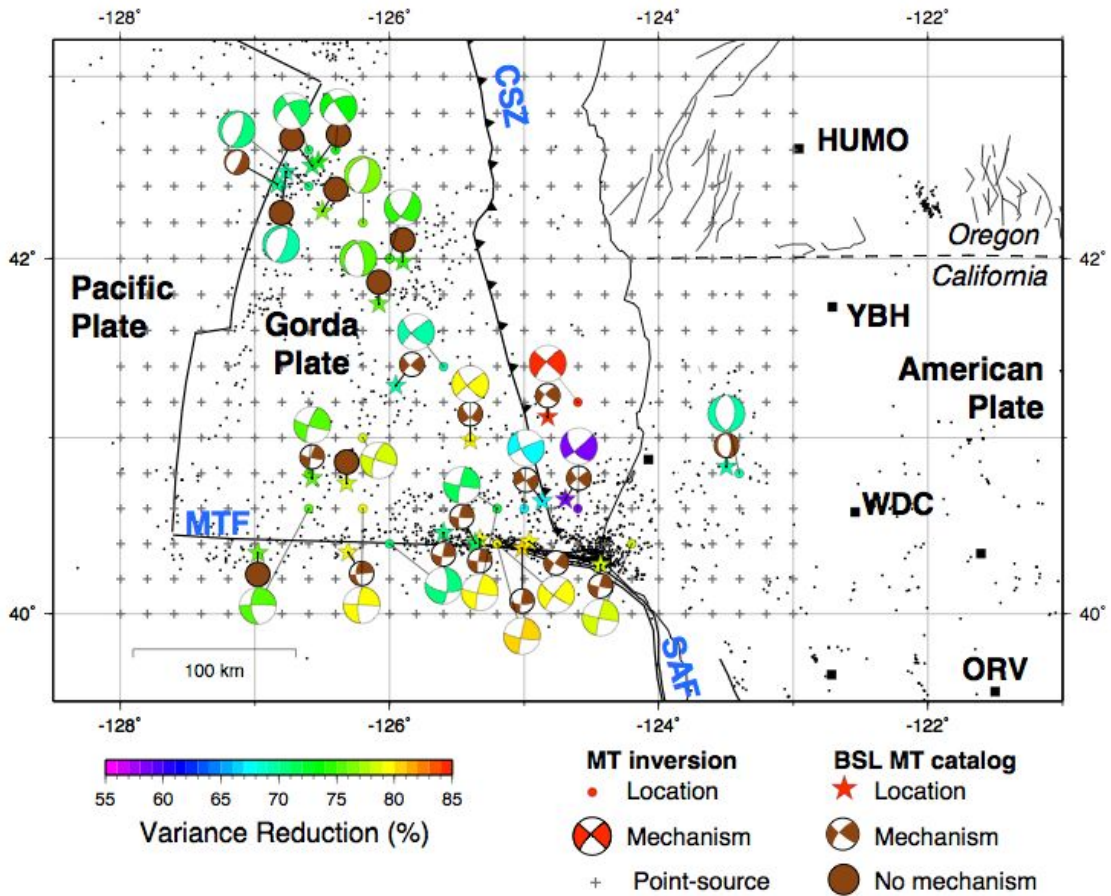


Figure 2.1: For large earthquakes that may produce tsunamis, it is important to determine the size and type of faulting of the event rapidly. We have developed a method to continuously scan an offshore region for earthquakes, and quickly determine their size and mechanism (see Research Section 21). The method is currently being applied to the region of the Mendocino Triple Junction, using data from four BDSN stations (HUMO, ORV, WDC and YBH). The pluses are the grid locations used in the search, while black dots show the region's seismicity since 1990. Mechanisms for the events studied are given from this analysis (large, light gray) and compared with solutions from the Berkeley moment tensor catalog (small, dark gray). For a color version of this figure see Research Section 21.

# 1 ElarmS Earthquake Early Warning

Holly Brown, Richard Allen, Douglas Neuhauser, Ivan Henson, Margaret Hellweg, Lim InSeub (KIGAM), Alon Ziv (BenGurion University)

## 1.1 Introduction

ElarmS is a network-based earthquake early warning (EEW) algorithm developed at UC Berkeley for rapid earthquake detection, location and hazard assessment. ElarmS operates as part of the greater ShakeAlert EEW system, an ongoing project by the California Integrated Seismic Network (CISN). ShakeAlert combines three different EEW algorithms, one of which is ElarmS, into a unified system for providing warnings for events throughout the state. Output from the three algorithms is compared and consolidated by the ShakeAlert Decision Module into a single alert messaging system. In fiscal year 2011-2012, these alert messages will be sent to industrial test users of the ShakeAlert system.

ElarmS consists of two primary parts: (1) a waveform processing algorithm, which runs in parallel at UC Berkeley, Caltech, and USGS Menlo Park to continuously filter real time seismic data, and (2) a single state-wide event detection algorithm which operates at UC Berkeley. The event detection module analyzes the incoming data from the three waveform processing streams and identifies earthquakes in progress.

## 1.2 Current Progress

In March 2011, ElarmS began sending event messages to the ShakeAlert Decision Module for events in the greater San Francisco Bay Area and Central Coast. Between March 17th and July 26th, 2011, there were 49 events of magnitude 3.0 or greater in the ElarmS alert region. ElarmS sent alert messages for 45 of them, and missed 4 (Figure 2.2). ElarmS also sent two false alerts. In both false alert cases, there was a single real event which ElarmS processed as two separate events - associating some triggers with one event and some triggers with the other. The alert message sent for the second “event” is thus a false alarm, although based on real seismic activity.

In 2010 and 2011, we developed second generation ElarmS waveform processing and event detection algorithms, based in C++ for speed and adaptability. The new event detection module (E2) utilizes the established location and magnitude relations, but has an updated method of associating triggers together to form events. One goal of the new associator is to prevent split events such as those that caused the false alerts mentioned above. E2 has been processing statewide real-time data in test mode since December 2010 and will become the authoritative ElarmS version in fall 2011.

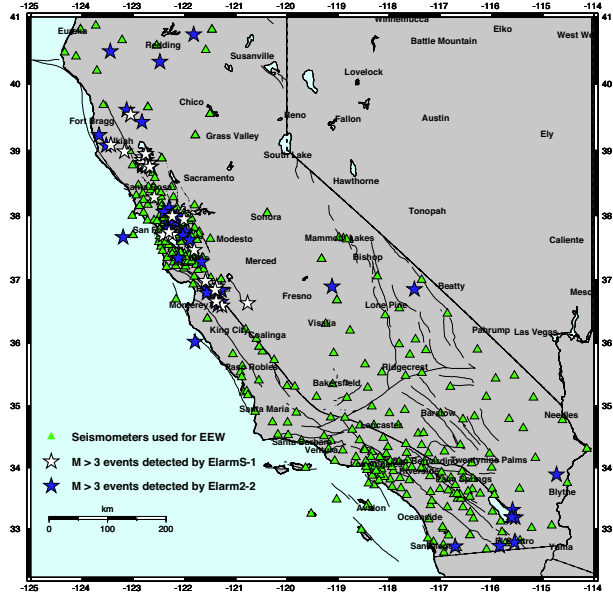


Figure 2.2: ElarmS events, March 17 - July 26, 2011

In addition to the second generation ElarmS algorithms, we developed a KML-based method of visually inspecting and assessing system performance. The assessment software automatically evaluates station latencies, promptness of alerts, accuracy of magnitude/location/ground-shaking estimates, and number of successful event detections, false alarms, and missed events. This information is displayed in Google Earth for quick, intuitive understanding of system health.

## 1.3 Investigation of GPS

In 2011 we also began investigating the use of GPS for earthquake early warning, focusing on the  $M_w$  7.2 El Mayor-Cucapah earthquake, which had both real-time GPS and seismic data available. We developed a simple algorithm to extract the permanent displacement at GPS sites starting one oscillation after triggering on the dynamic long period signal. The estimate is continually improved with time. These permanent displacements can then be inverted for source characteristics given an approximate estimate of the fault plane. Initial results suggest that GPS would provide a valuable contribution to EEW. The new approach provides an independent estimate of magnitude, which is particularly important for the largest events.

## 1.4 Acknowledgements

This project is funded by USGS/NEHRP award 06HQAG0147.

## 1.5 References

Brown, H., R.M. Allen, M. Hellweg, O. Khainovski, D. Neuhauser, and A. Souf, Development of the ElarmS methodology for earthquake early warning: Realtime application in California and offline testing in Japan, *Soil Dynamics and Earthquake Engineering*, 31, 188-200, 2011.

Allen, R.M., Seconds before the big one, *Scientific American*, 2011.

Allen, R.M. and A. Ziv, On the potential implementation of real-time GPS in earthquake early warning systems: The Mw 7.2 El Mayor-Cucapah Earthquake test case, *Geophys. Res. Lett.*, in review.

## 2 ShakeAlert: A Unified EEW System for California

Margaret Hellweg, Richard Allen, Maren Böse (Caltech), Holly Brown, Georgia Cua (ETH), Egill Hauksson (Caltech), Thomas Heaton (Caltech), Margaret Hellweg, Ivan Henson, Doug Neuhauser, Kalpesh Solanki (Caltech), Michael Fischer (ETH)

### 2.1 Introduction

Earthquake Early Warning (EEW) is a method of rapidly identifying an earthquake in progress and transmitting alerts to nearby population centers before damaging ground shaking arrives. The first few seconds of the initial P-wave arrivals at one or more stations are used to detect the event, and predict magnitude and peak shaking. Detections from several stations are combined to locate the event. A warning of imminent shaking can be used to activate automatic safety measures, such as slowing down trains, isolating sensitive factory equipment, or opening elevator doors. Warnings can also be sent directly to the public via cell phone, computer, television, or radio.

With support from the United States Geological Survey (USGS), the California Integrated Seismic Network (CISN) hosted a three-year proof of concept project for EEW algorithms in 2006-2009. Following that successful project, the Berkeley Seismological Laboratory (BSL) together with its CISN EEW partners, the California Institute of Technology (Caltech), and the Swiss Institute of Technology Zürich (ETH), are collaborating to build a single, integrated, end-to-end system for testing real-time EEW in California. The new system, called CISN ShakeAlert, will be capable of continuous long-term operation and rapidly provide alerts to test users across the state.

### 2.2 Project Status

The new ShakeAlert system combines the best aspects of the three methods from the proof-of-concept project. Caltech's OnSite algorithm uses P-wave data from the single station nearest the epicenter to provide extremely rapid estimates of likely ground shaking. The BSL's ElarmS algorithm and ETH's Virtual Seismologist algorithm use data from several stations around an event epicenter to produce a slightly slower but more reliable estimate of magnitude and location. Combining these methods produces an algorithm which has the speed of a single-station method but is then promptly confirmed and adjusted by additional station data to form a more accurate description of the event. When an identified event exceeds a defined combination of magnitude threshold, ground shaking intensity and statistical likelihood, information is broadcast to system users. Currently, during the development phase, only project participants receive event information. By the fall of 2011, event information will be sent to a small group of test users outside

the seismological community.

These tasks of the end-to-end system are accomplished in four primary software components (Figure 2.3). First, the Waveform Processing (WP) Module receives seismic waveforms from all early-warning capable seismic equipment in California. It identifies P-wave arrivals, and calculates the relevant P-wave parameters necessary for EEW magnitude estimation. Next, the Event Monitoring (EM) Module comprising the OnSite, Virtual Seismologist, and ElarmS algorithms recognizes events in progress and calculates event magnitude and location. It passes this information to the third component, the Decision Module (DM). The DM can receive event notifications from several systems, including the three algorithms of the EM module. It reviews events and determines whether to send warnings to users. The final component is the User Display (UD), which will be installed at an EEW user's site. When the UD receives a warning from the DM, it sounds an alarm and generates an alert message, a map of expected ground shaking intensities, or other output, depending on the user's settings.

The end-to-end system is now in operation. Caltech programmers developed the UD, while Berkeley programmers built the DM. The three CISN EEW partners (Caltech, BSL, ETH) are working together to jointly build a new, quicker and robust Waveform Processing Module.

### 2.3 Perspectives

During the coming year, the CISN EEW project members will continue to operate and improve the elements of the end-to-end system, including efforts to improve the speed and accuracy of alerts. We will recruit a group of test users outside of the seismology community and interact with them to develop improvements to the system, as well as to learn about the advantages of EEW to users and to society. Finally, results from the prototype system will flow into the CISN Testing Center (CTC) software, so that the results and output can undergo objective evaluation.

### 2.4 Acknowledgements

This project is supported at UC Berkeley by USGS Cooperative Agreement G09AC00259, at Caltech by Agreement G09AC00258, at USC/SCEC by Agreement G09AC00255 and at ETH Zürich by Agreement G09AC00256.

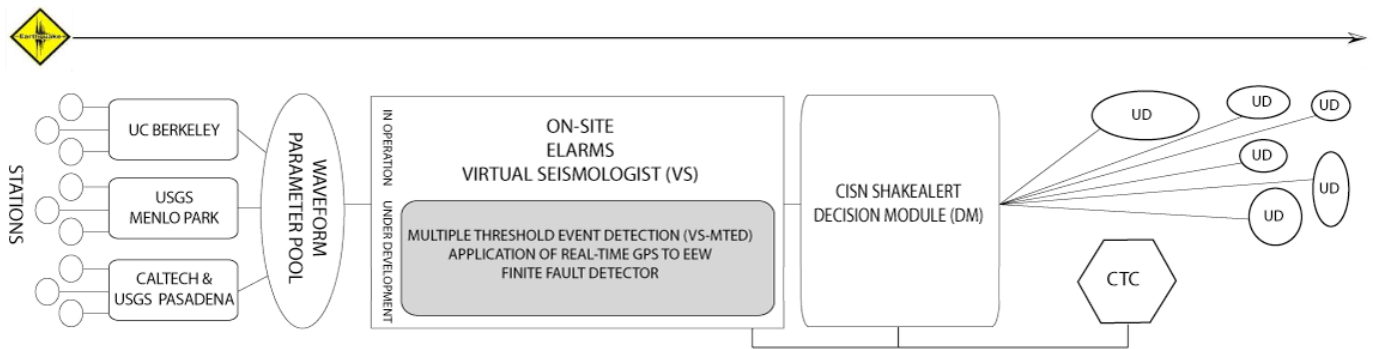


Figure 2.3: Components of the new ShakeAlert EEW System. From left to right the elements of the system are waveform processing, event detection, decision module (DM), CISN ShakeAlert user displays (UD), and the CISN testing center (CTC) software. *Waveform Processing:* Each data center processes telemetered digital waveform data collected from seismic stations throughout California. Critical waveform parameters are calculated from this data, then dumped into a statewide parameter pool. *Event Detection:* From the parameters, CISN’s EEW algorithms rapidly detect and characterize an event within seconds of its initiation. Several EEW detection algorithms run in parallel to provide the Decision Module with the best available source parameters. *Decision Module:* The DM combines earthquake information from each algorithm and delivers a “ShakeAlert” xml message about an earthquake in progress to subscribed users. *CISN ShakeAlert User Displays:* The ShakeAlert UD receives xml messages from the DM and displays their content in a simple and easily understandable way. *CISN Testing Center Software:* The CTC Software provides automated and interactive performance evaluations of ShakeAlert forecasts.

### 3 Validation of Coda-derived Source Parameters using Strong and Weak Ground Motion Records of the 2008 Wells, Nevada Sequence

Seung-Hoon Yoo, Douglas S. Dreger, and Kevin Mayeda

#### 3.1 Introduction

Well-determined source parameters, such as corner frequency and stress drop, and their scaling relation, can play an important role in assessing the seismic hazard in a specific region, especially in regions where we do not have enough strong ground motion records. In general, ground motions at higher frequencies (1-10 Hz), which may cause damage to surface structures, can be considerably varied depending upon the stress drop of the earthquake, even for events with similar moment magnitude.

*Petersen et al.* (2011) found that while observed ground motions from the 2008 Wells mainshock are similar to values predicted by the Next Generation Attenuation (NGA) equation by *Campbell and Bozorgnia* (2008), the ground motion from the M 4.7 ( $M_w$  4.4 from the Saint Louis University Earthquake Center moment tensor catalog, courtesy of *R. B. Herrmann* and this study) aftershock, which occurred the day after the mainshock, are much lower than values from the NGA equation. However, they estimated this aftershock’s stress drop as 220 bars, which is much higher than typical stress drops observed in the Basin and Range.

In this study, we revisited the 2008 Wells, Nevada sequence to examine a marked discrepancy in the observed strong and weak ground motion with the NGA predictions. We estimated the source parameters of the seismic sequence using the coda spectral ratio method (*Mayeda et al.*, 2007). And, we examined the observed strong and weak ground motion with the derived parameters and self-similar scaling relation.

#### 3.2 Data and Method

We calculated source spectral ratios between the mainshock and the six aftershocks using the coda spectral ratio method (*Mayeda et al.*, 2007). We used a grid-search scheme to estimate the source parameters from the source spectral ratios. The program finds a corner frequency of the mainshock, and the corner frequency and adjusted seismic moment of the aftershocks from a given ratio dataset, simultaneously. To get the optimum source parameters and their errors, we performed bootstrap tests, which sample four event pairs of the six total ratio curves (~67 % sampling of a population), then calculated the averages and standard deviations for the results of the 15 possible combinations (Figure 2.4). Next, we calculated theoretical source ratios for periods of 0.2, 0.5, and 1 second using the derived source parameters. And we also calculated the theoretical values based on

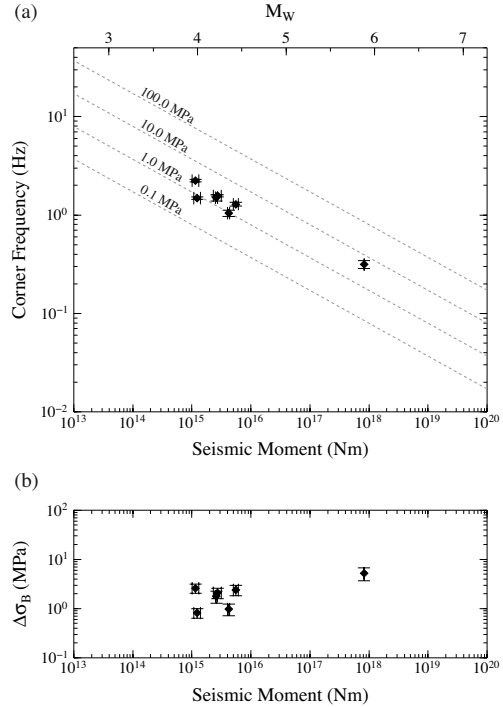


Figure 2.4: Estimates of the (a) corner frequency and (b) stress drop for the 2008 Wells, Nevada seismic sequence. The dotted lines in (a) represent the corner frequencies from the self-similar scaling for a given stress drop,  $\Delta\sigma_B$ .

the self-similar scaling with respect to the mainshock.

The Fourier amplitude spectrum of ground acceleration,  $A(M_0, R, f)$ , can be expressed as

$$A(M_0, R, f) = CM_0 (2\pi f)^2 S(f) D(R, f) P(f) I(f),$$

where  $C$  is a constant of proportionality,  $M_0$  is the seismic moment,  $S(f)$  is the source spectrum,  $D(R, f)$  is an attenuation term as a function of distance  $R$  due to the geometrical spreading and anelastic attenuation,  $P(f)$  is a high-cut filter,  $I(f)$  is a filter used to shape the spectrum to correspond to the particular ground motion (e.g., *Boore*, 1983). If we calculate a ratio of the ground motions between the two collocated events, the ratio can be simply approximated by a source spectral ratio between the two events.

We computed the 5% damped pseudo spectral acceleration (SA) for the periods 0.2, 0.5, and 1 seconds as a geometric mean of two horizontal components (Figure 2.5a). Then, we calculated the ratios between the mainshock and the aftershocks for a given period and averaged

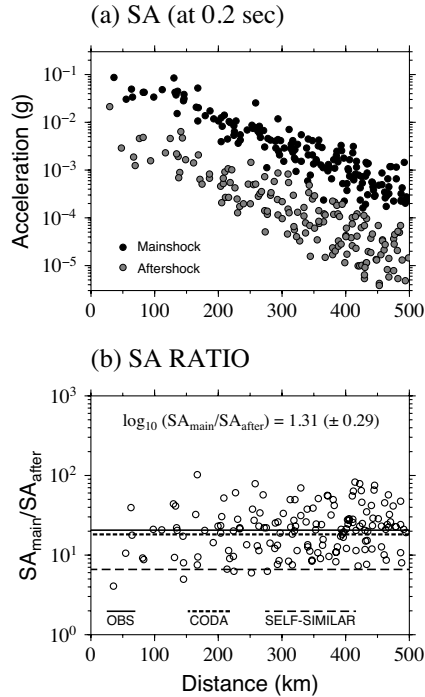


Figure 2.5: (a) The 5 % damped pseudo spectral acceleration (SA) of the mainshock (MS; black solid circles) and the aftershock (A3; gray solid circles), (b) comparison of the observed SA ratio (open circle and solid line) with the two theoretical values from the coda-derived source parameters (fine dotted line) and self-similar scaling relation (coarse dotted line).

using all the stations (Figure 2.5b).

### 3.3 Results and Discussions

The stress drop of the mainshock,  $5.20 (\pm 1.52)$  MPa, is consistent with 7.2 MPa from an empirical Green's function finite fault inversion by *Mendoza and Hartzell* (2009), more or less. However, the stress drop of the aftershock A3,  $1.00 (\pm 0.27)$  MPa, is much smaller than 22 MPa from Fourier spectra analysis by *Petersen et al.* (2011), and it is also about five times smaller than that of the mainshock in our estimation.

We compared the averaged SA ratio,  $\log(SA_{\text{main}}/SA_{\text{after}})$ , with theoretical values from the coda-derived source parameters and the self-similar scaling relation with respect to the mainshock. For the MS/A3 event pair, the observed SA ratio values at 0.2, 0.5, and 1 second periods are 1.31, 1.38, and 1.52, respectively, which are much more consistent with the theoretical values, 1.26, 1.34, and 1.53, from the coda estimates, than 0.82, 1.02, and 1.36 from the self-similar source scaling relation (Figure 2.5). For all the other event pairs, the theoretical values from coda estimates are more consistent with the observations than those from the self-similar scaling (Figure 2.6).

In conclusion, the stress drops of the aftershocks are 2-5 times smaller than that of the mainshock in this seis-

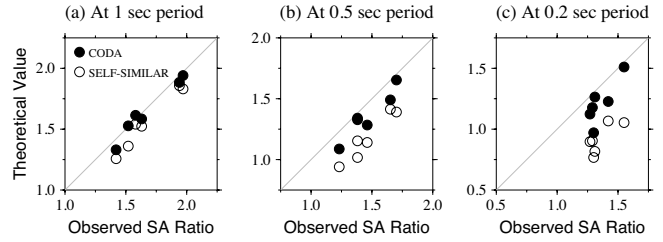


Figure 2.6: Comparisons of the theoretical source ratios for the coda-derived source parameters (solid circles) and self-similar scaling (open circles) with the observed SA ratios between the mainshock and six aftershocks at the 1, 0.5, and 0.2 second periods.

mic sequence. This indicates that weak ground motion of the aftershocks can be overestimated to be higher than the real observation using strong ground motion of the mainshock based on a self-similar scaling relation. Assuming that the scale-dependent stress drop is real, at least in some specific regions, predicting ground motion using weak ground motion records without considering the scaling relation could lead to an underestimate of strong ground motions for future large earthquakes. For the region, considering the differences in the stress drop between the small and large earthquake might help to enhance the prediction capability of the strong ground motion.

### 3.4 Acknowledgements

S.-H Yoo was partially supported by the National Research Foundation of Korea under Grant NRF-2010-357-C00135. S.-H. Yoo would like to thank Taka'aki Taira for beneficial comments and discussions.

### 3.5 References

- Boore, D. M., Stochastic simulation of high-frequency ground motions based on seismological models of the radiated spectra, *Bull. Seismol. Am.*, *73*, 1865-1894, 1983.
- Campbell, K. W., and Bozorgnia, Y., NGA ground motion model for the geometric mean horizontal component of PGA, PGV, PGD, and 5 % damped linear elastic response spectra for period ranging from 0.01 to 10 s, *Earthquake Spectra*, *24*, 139-172, 2008.
- Mayeda, K., Malagnini, L., and Walter W. R., A new spectral ratio method using narrow band coda envelopes: Evidence for non-self-similarity in the Hector Mine sequence, *Geophys. Res. Lett.*, *34*, L11303, doi:10.1029/2007/GL030041, 2007.
- Mendoza, C., and Hartzell, S., Source analysis using regional empirical Greens functions: The 2008 Wells, Nevada, earthquake, *Geophys. Res. Lett.*, *36*, L11302, doi:10.1029/2009GL038073, 2009.
- Petersen, M., Pankow, K., Biasi, G., Meremonte, M., Harmsen, S., Mueller, C., and Zeng, Y., Ground motions from the 2008 Wells, Nevada earthquake sequence and implications for seismic hazard, *Nevada Bureau of Mines and Geology Special Publication*, *36*, 163-172, 2011.

# 4 Quantitative Analysis of Coda Window Length: How Much Length of Coda is Enough for Stable Amplitudes?

Seung-Hoon Yoo, Kevin Mayeda, and William R. Walter (LLNL)

## 4.1 Introduction

In earthquake source estimation, coda-derived source methods provide more stable source parameters than methods using direct waves due to the inherent averaging nature of coda waves (Mayeda and Walter, 1996; Mayeda *et al.*, 2007). Unlike conventional direct-phase regional measurements (e.g., *Pg* or *Lg*), which take peak amplitude at the specific arrival time, the coda amplitude measurement through a relatively long time window can dramatically reduce the inter-station scattering by smoothing out 3-D path variability, source radiation pattern, and directivity effects (Mayeda and Malagnini, 2010).

Although a number of studies have shown this stability of the coda measurement, it is still unclear how much length of coda is enough for accurate measurements of coda amplitudes. Inappropriate short window measurement can not only lead to higher inter-station scatter of coda amplitudes, but can also give a distorted amplitude by using only earlier parts of a coda envelope, which shows a radical change in energy density with increasing lapse time. But long-lasting coda, which guarantee a stable measurement, are not always easy to obtain, because of small magnitude, low signal to noise ratio, and interfering aftershocks.

In this study, to address this unsettled question and quantify the optimum window length for accurate coda measurements, we analyze inter-station standard deviation of the coda ratios as a function of the time window length using an earthquake sequence data set that was well-recorded by a dense broadband seismic array. This allows us an in-depth look at the effects of coda on averaging over source radiation pattern and directivity and can help serve as a guide to future coda-based studies regarding how much window length is needed to get good measurements.

## 4.2 Data and Method

We use the broadband records of the 2008 Wells, Nevada seismic sequence to quantify the window length effect for coda amplitudes and source ratios in terms of reducing variance due to radiation pattern and directivity. Fortunately, because the EarthScope USArray temporary seismic network was operating in this region at the time of the earthquakes, this sequence can offer a great opportunity with a number of high-quality records and perfect distances and azimuthal coverage.

The seismic sequence consists of an M 6 mainshock

and its six aftershocks with magnitudes ranging between M 4.0 and 4.5. We select 162 broadband stations within about 500 km epicentral distance of the Wells mainshock. For each event at each station, we measure the coda amplitude for 24 narrowband frequencies ranging from 0.05 to 15 Hz. All amplitudes are measured from a one second window length to the end of the possible record for coda measurement based on signal to noise or existence of an interfering aftershock.

## 4.3 Preliminary Results and Discussions

Figure 2.7 shows the amplitude ratio between the mainshock and an M 4.4 aftershock for the direct *Lg* and coda waves. In general, the direct *Lg* amplitude ratios vary considerably with azimuth due to the source radiation pattern or directivity effects of the two events. The coda amplitude ratios with a relatively short window length (2nd row entries in Figure 2.7) behave similarly to the direct *Lg* ratio. With increasing window length ( $T_L$ ), however, the azimuthal variations of the coda amplitude ratio decrease significantly.

To quantify a reduction of the standard deviation, we normalize the standard deviation values with the standard deviation values at the 1 second window length and divide the window length ( $T$ ) by a central period ( $T_0$ ). We found that normalized standard deviations linearly decrease with  $\log_{10}$  scales of  $T/T_0$ , and the reduction rates depend on the central frequency (Figure 2.8). The higher frequency bands show a larger slope of reduction than lower frequency bands.

To find a best fitting curve, we used an empirical equation,

$$\sigma(\tau = T/T_0) = \begin{cases} 1 & (\tau < \tau_0) \\ 1 - p \log_{10}(\tau/\tau_0) & (\tau > \tau_0) \end{cases},$$

where  $p$  represents a reduction rate, while  $\tau_0$  represents a starting point of decay with reduction rate  $p$ .

Though these preliminary results show very interesting properties of coda stability for the Wells, Nevada sequence, they leaves us with other questions and ideas that we wish to pursue in the near future, namely: 1) To what extent does the reduction rate,  $p$ , behave the similarly for other parts of the world? 2) Can a single functional form that is frequency-dependent be used to characterize coda amplitude error as a function of measurement window length? 3) We would like to study other sequences with good signal-to-noise ratio in a variety of different tectonic settings. 4) We plan to test the methodology

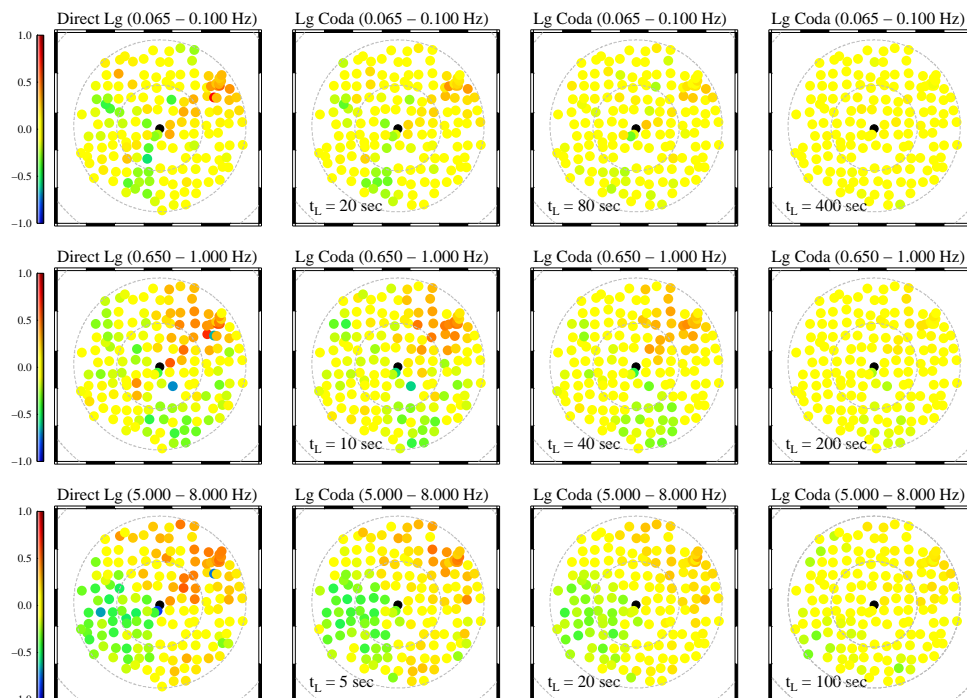


Figure 2.7: Coda amplitude ratios between the 2008 Wells mainshock and M 4.4 aftershock. Rightmost plots show the direct  $Lg$  amplitude ratios for given narrowband frequencies. The left side plots of the direct  $Lg$  ratio plots show the coda amplitude ratios with different window length ( $T_L$ ) for the same frequency bands. The black circles in the subplot represent the location of the mainshock, and each colored circle represents a station. The small and large dotted circles represent 250 and 500 km iso-epicentral distance, respectively.

using a much smaller subset of stations, since the large amounts of data are not usually common.

#### 4.4 Acknowledgements

S.-H Yoo was supported by the National Research Foundation of Korea under Grant NRF-2010-357-C00135. K. Mayeda was partially funded through LLNL’s GNEM program.

#### 4.5 References

Mayeda, K., and Malagnini L., Source radiation invariant property of local and near-regional shear-wave coda: Application to source scaling for the Mw 5.9 Wells, Nevada sequence, *Geophys. Res. Lett.*, *37*, L07306, doi:10.1029/2009GL042148.

Mayeda, K., Malagnini, L., and Walter W. R., A new spectral ratio method using narrow band coda envelopes: Evidence for non-self-similarity in the Hector Mine sequence, *Geophys. Res. Lett.*, *34*, L11303, doi:10.1029/2007/GL030041, 2007.

Mayeda, K. and Walter, W. R., Moment, energy, stress drop, and source spectra of western United States earthquakes from regional coda envelopes, *J. Geophys. Res.*, *101*(B5), 11195-11208, 1996.

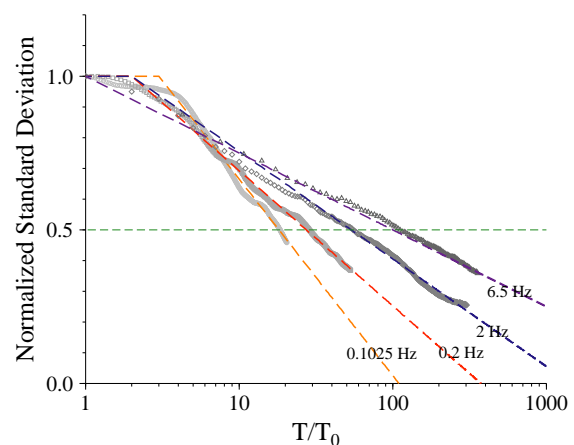


Figure 2.8: Normalized standard deviation versus normalized window length,  $T/T_0$ , for the mainshock and M 4.4 aftershock pair. The dotted lines represent a best fit model for each data set (gray symbols). The reduction rates of normalized standard deviation vary with frequency and linearly decrease in a  $\log_{10}$  scale with  $T/T_0$ . To reach 50 % reduction, higher frequencies need much larger  $T/T_0$  values than lower frequencies.

# 5 Source Characterization of Mendocino Offshore Earthquakes for Improvements in Monitoring Active Deformation and Estimates of Earthquake Potential in the Mendocino Triple Junction Region

Taka'aki Taira and Robert M. Nadeau

## 5.1 Introduction

The Mendocino Triple Junction (MTJ), a fault-fault-trench junction, is one of the most seismogenic regions of California. The MTJ region has experienced a number of different fault slips (Figure 2.9), such as aseismic slip events (Szeliga *et al.*, 2004), non-volcanic tremors (Boyarko and Brudzinski, 2010), slow/low-stress-drop earthquakes (Guilhem *et al.*, 2007), deep low-frequency earthquakes (Boyarko and Brudzinski, 2010), and characteristically repeating microearthquakes (Waldhauser and Schaff, 2008). Apparently, the small-magnitude ambient seismicity (regular and characteristically repeating microearthquakes) is spatially anticorrelated with the distribution of non-volcanic tremor sources and low-frequency events (Boyarko and Brudzinski, 2010). However, the locations of those fault slips are not well constrained because of greater distances between the offshore fault slips and the available land seismic stations. Subsequently, the nature of interactions between seismic and aseismic deformation processes remains unclear.

We seek to integrate secondary phase arrivals with a local three-dimensional structure (Hole *et al.*, 2000) for improving the locations of fault slips, especially characteristically repeating earthquakes whose locations would delineate regions of locked fault zones. Additionally, repeating earthquake systematics (frequency and magnitude) can be used to estimate deep fault creep rates. Here we show an example of results from our frequency-wavenumber analysis and the preliminary result for the identification of characteristically repeating earthquakes.

## 5.2 Frequency-Wavenumber Analysis

We make use of seismic data from the Canadian Yellowknife Array (YKA), a small-aperture array consisting of 19 short-period stations, in order to identify secondary phase arrivals, particularly depth phases (pP and sP phases) and their phase conversions for  $M > 4$  MTJ earthquakes (Figure 2.10). It appears that the YKA recorded depth phases from MTJ earthquakes well - particularly sP phases - because of larger S-wave energy from the source due to the combination of geometry between YKA and MTJ earthquakes and the majority of right lateral strike-slip faulting in the MTJ fault zone (Figure 2.10b). With the depth phase identified from the YKA seismic array data, we were able to constrain the focal depth of the 2007  $M_w$  5.0 MTJ event to be 24 km (Fig-

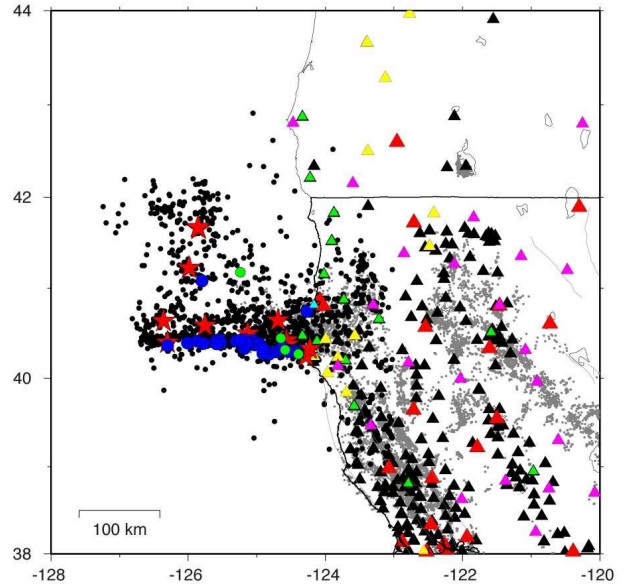


Figure 2.9: Location of the MTJ earthquakes (gray circles) during 1984-current from the NCEDC catalog. Back dots are  $M > 3$  earthquakes analyzed in our preliminary analysis to identify characteristically repeating earthquakes. Blue circles are identified repeating earthquakes. Also shown are slow/low-stress-drop earthquakes (green circles) (Guilhem *et al.*, 2007) and  $M > 6$  earthquakes (red stars). Triangles are seismic stations. Red triangles are the broadband stations of BDSN. Black and green ones are USGS's short-period and broadband seismic stations, respectively. Yellow triangles are the PBO borehole seismometers and the light blue one is the CGS borehole seismic array. Also shown are broadband seismometers of EarthScope Transportable Array (purple triangles).

ure 2.10c).

## 5.3 Characteristically Repeating Microearthquake

Our preliminary search for repeating microearthquakes in the MTJ region has revealed numerous and distributed sites of repeating microearthquake activity in the MTJ region (Figures 2.9 and 2.11). In the preliminary work, we have focused on  $M > 3$  earthquakes in the MTJ region. We are currently extending our analysis to smaller earthquakes and are particularly interested in detecting temporal changes in fault creep rates inferred from re-

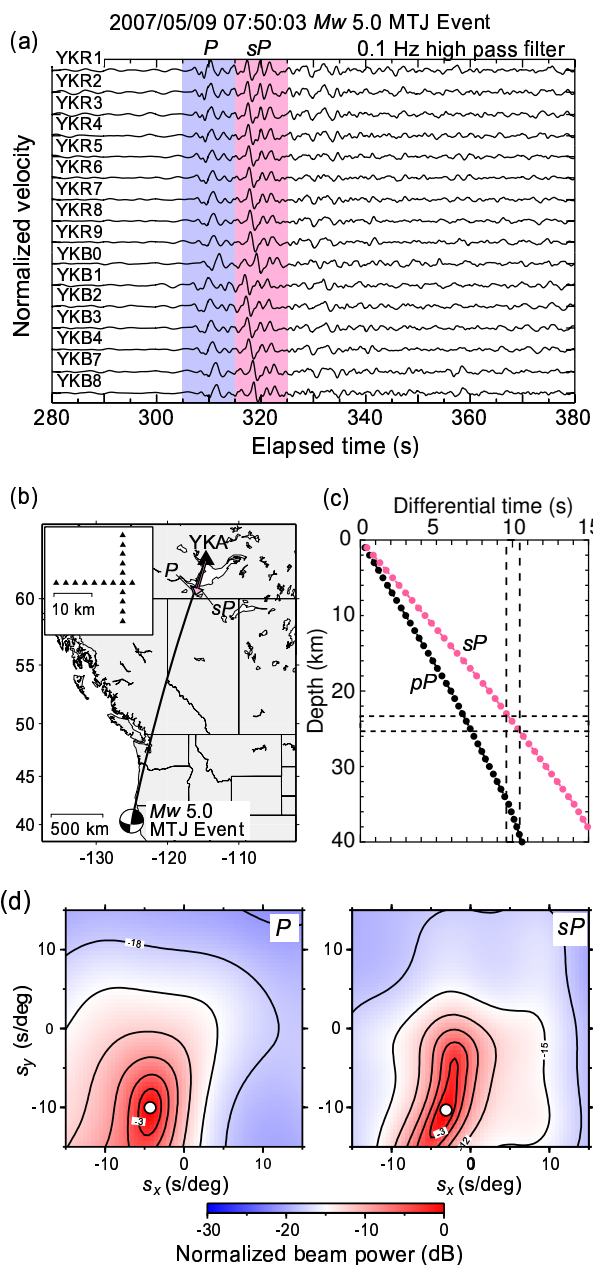


Figure 2.10: (a) An example of observed YKA data for the 9 May 2007  $M_w$  5.0 MTJ earthquake. The direct P and sP phases are seen at 310 s and 320 s, respectively. (b) Map view of the MTJ event and the YKA. Also shown are estimated back azimuths for P and sP phases. (c) Predicted time difference between P and sP (and pP) phases as a function of source depth using the ak135 velocity model (Kennett *et al.*, 1995). The time difference between sP and P phases of 10 s indicates the focal depth to be 24 km. (d) Frequency-wavenumber diagrams for P and sP phases. The slowness and back azimuth of the maximum power is marked by the white circle.

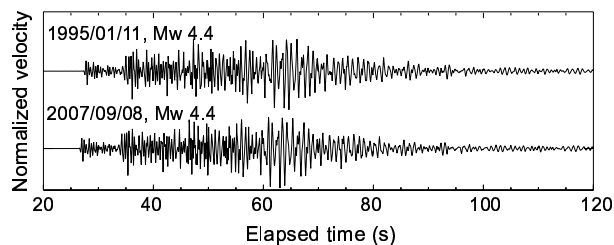


Figure 2.11: Characteristically repeating earthquakes identified from our preliminary analysis. An example of vertical seismograms recorded at station WDC for an earthquake doublet in the MTJ region. This earthquake doublet has the largest magnitude ( $M_w$  4.4) among the identified repeating earthquake sequences. A 1-4 Hz bandpass filter was applied.

peating microearthquakes accompanying tectonic events (for example, the 9 January 2010  $M$  6.5 Gorda Plate earthquake).

## 5.4 Acknowledgements

We thank J. Hole for sharing the three-dimensional seismic velocity model with us. This work is supported by the U.S. Geological Survey NEHRP program under grant number G11AP20168.

## 5.5 References

- Boyarko, D.C. and M.R. Brudzinski, Spatial and temporal patterns of nonvolcanic tremor along the southern Cascadia subduction zone, *J. Geophys. Res.*, *115*, B00A22, doi:10.1029/2008JB006064, 2010.
- Guilhem, A., D.S. Dreger, and R.M. Nadeau, Scanning of unusual seismic activity in the Mendocino Triple Junction region, *EOS Trans. AGU*, *88*(52), Fall Meet. Suppl., Abstract S43-1047, 2007.
- Hole, J.A., B.C. Beaudoin, and S.L. Klemperer, Vertical extent of the newborn San Andreas fault at the Mendocino triple junction, *Geology*, *28*, 1111-1114, 2000.
- Kennett, B.L.N., E.R. Engdahl, and R. Buland, Constraints on seismic velocities in the Earth from traveltimes, *Geophys. J. Int.*, *122*, 108-124, 1995.
- Szeliga, W., T.I. Melbourne, M.M. Miller, and V.M. Santillan, Southern Cascadia episodic slow earthquakes, *Geophys. Res. Lett.*, *31*, L16602, doi:10.1029/2004GL020824, 2004.
- Waldhauser, F. and D.P. Schaff, Large-scale relocation of two decades of Northern California seismicity using cross-correlation and double-difference methods, *J. Geophys. Res.*, *113*, B08311, doi:10.1029/2007JB005479, 2008.

# 6 Detecting the 2011 M9.0 Tohoku Earthquake with Moment Tensors

Aurelie Guilhem and Douglas S. Dreger

## 6.1 Introduction

The M9 Tohoku earthquake offshore Japan that occurred on May 11, 2011 triggered strong local and regional shaking as well as a large-scale tsunami that caused major damage in both the near- and far-field. The Japanese earthquake and tsunami warning systems were able to detect and locate the earthquake; however information regarding the focal mechanism of the event was unknown until the moment tensor from the W-phase was published about 20 minutes after the event. Because of the dense Japanese seismic network of strong-motion stations (K-NET), this event gives us the opportunity to test the approach proposed by *Guilhem and Dreger, 2011* to rapidly detect, locate, and obtain the moment magnitude and mechanism of megathrust earthquakes.

## 6.2 Method

We use the method proposed by *Guilhem and Dreger (2011)* to automatically compute moment tensors on a grid of virtual sources distributed every 0.25 in latitude and longitude and at the slab depth, following a streaming data procedure. Here, the grid is defined by 357 nodes and overlaps the rupture of the M9 Tohoku earthquake (Figure 2.12). Moment tensors are computed every second, and the detection of the earthquake and its source information (location, seismic moment, mechanism, origin time) is obtained once the variance reduction (VR), which measures the fit between the data and the synthetics, reaches a maximum value and is above a threshold value (65%, for example). Velocity Green's functions (GFs) for each virtual source, and corresponding slab depths are pre-calculated using a 1D velocity model used by *Tsuruoka et al. (2009)* for the GridMT technique used in Japan. Because we target a large-scale earthquake, we include a source time duration in the GFs of 150 seconds.

## 6.3 Data

We download the strong-motion records of the M9 earthquake from the K-NET database, corresponding to a dataset of three-component acceleration seismograms for 273 stations. We select a set of 12 stations distributed along the earthquake rupture that recorded 300 seconds of data at 100 samples per second. We first correct the data for the instrumental gain and decimate them to 1 sample per second. Because the proposed method of *Guilhem and Dreger (2011)* for the rapid detection of  $M > 7$  earthquakes uses very long-period (100-200 second) data and inverts 8 minutes of records, we extend the

strong-motion records by adding zeros to generate seismograms of 30 minutes in length; then we integrate them to velocity and use a causal bandpass filter with corner frequencies of 0.005 and 0.01 sec.

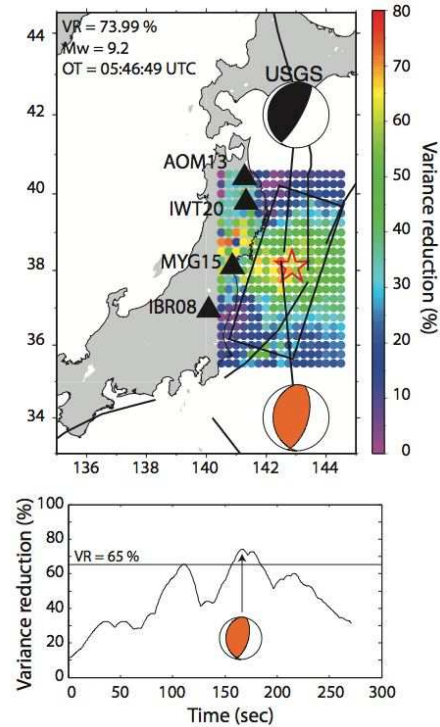


Figure 2.12: Map of the best moment tensor solutions using a set of strong motion stations distributed along the rupture. The star shows the JMA location, the black beach ball diagram shows the Global CMT USGS solution and the colored mechanism corresponds to the best solution using the grid. (See color version of this figure on the front cover.)

We use sets of four strong-motion stations per calculation, and we test the sensitivity of the moment tensor analysis for different limited station coverages (Figure 2.12).

## 6.4 Results

Figure 2.12 shows that the long period single point-source GFs used in the moment tensor approach allow the detection and characterization of the megathrust event with a high level of confidence (i.e.  $>70\%$ ) even if the station coverage is limited. The best solutions are cen-

tered within the rupture segment, and our best solutions (i.e. with the largest VRs) are in close proximity to the USGS CMT solution (black mechanism in Figure 2.12) and to the JMA epicenter (red star). The origin time, the moment magnitude, and the mechanism that we find are in agreement with other datasets (USGS CMT, USGS W-phase, Global CMT). This shows that this analysis that uses a 100-200 sec passband does not suffer from saturation, which is a common problem observed for such large earthquakes, and was observed again for the M9 Tohoku earthquake. Also, the higher variance reduction estimates do appear to define the limits of the main slip area.

Finally, we find similar results when using restricted data coverage; i.e. when we use stations that are only located in the northern part of the rupture and inversely with stations located to the south of it (Figure 2.13). However, as Figure 2.13 shows, having stations located along the entire rupture enables us to better define the area of slip with the best VRs for the earthquake.

## 6.5 Conclusion

These results are very promising for the rapid detection and characterization of the major M9 Tohoku earthquake and other large magnitude subduction zone earthquakes. The 100-200 sec period strong-motion data do not saturate, and, as a consequence, the seismic moment and mechanism can be obtained within 8 minutes of the origin time. Because the M9 Tohoku earthquake had a compact slip region over a relatively small rupture length for similar sized earthquakes, the single point-source GFs work well. However, for more elongated slip models with multiple large slip areas, the use of quasi-finite-source GFs might provide better constraints on the events, as demonstrated by *Guilhem and Dreger* (2011).

## 6.6 Acknowledgements

Strong motion data for the 2011 M9.1 Japan earthquake are from the K-NET, National Research Institute for Earth Science and Disaster Prevention (NIED).

## 6.7 References

Guilhem, A., and D. S. Dreger, Rapid detection and characterization of large earthquakes using quasi-finite-source Green's functions in continuous moment tensor inversion, *Geophys. Res. Lett.*, 38, L13318, doi:10.1029/2011GL047550, 2011.

Tsuruoka, H., H. Kawakatsu, and T. Urabe, GRiD MT (grid-based real-time determination of moment tensors) monitoring the long-period seismic wavefield, *Physics of the Earth and Planetary Interiors*, 175, 8-16, doi:10.1016/j.pepi.2008.02.014, 2009.

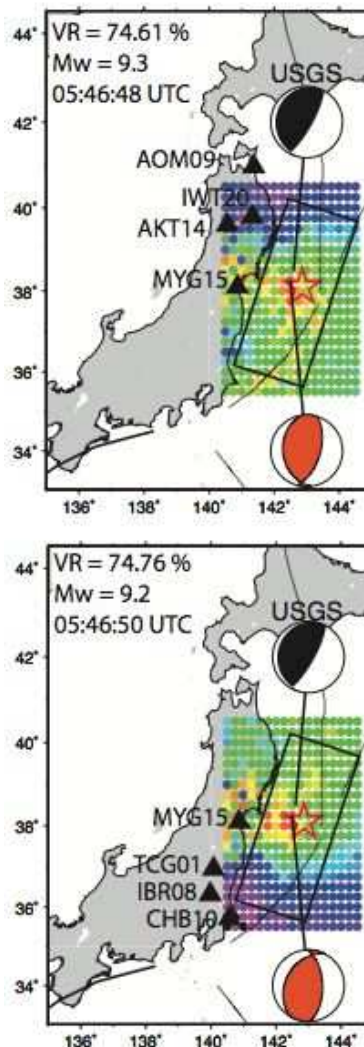


Figure 2.13: Map of the best moment tensor solutions using a set of strong motion stations distributed along the rupture.

# 7 Time-Lapse Monitoring for Detection of Transient Stress Changes in Geysers Geothermal Field

Taka'aki Taira

## 7.1 Introduction

Temporal changes in the properties of seismic structures are indicators of stress changes at depth, providing a means of continually monitoring the state of stress at seismogenic depth. At the Geysers geothermal field, we investigate stress-induced structural changes by making use of continuous seismic data at high sampling rates from dense seismic networks operated by LBNL and the USGS. Of particular importance to our work is the LBNL seismic network that contains 28 seismic stations distributed over the geothermal field (Figure 2.14). Each station consists of 3-component sensors with a natural frequency of 4.5 Hz sampled at 500 Hz.

## 7.2 Seismic Velocity Change

Our principal focus is on the imaging of time-varying properties of the seismic noise wavefield. Following *Bensen et al.* (2007), we analyzed data from August to December 2006, spanning the time of the 20 October 2006  $M_w$  4.6 Geysers earthquake. A reference Green's function was computed for each station pair by stacking the daily cross-correlations for the entire 5-month period (Figures 2.15a and b). The changes in seismic structure were determined by measuring time delays between the reference Green's function and 30-day stacks of cross-correlation functions in the frequency range from 0.1 to 0.9 Hz. Our preliminary result shows a change in cross-correlation function immediately after the 2006  $M_w$  4.6 Geysers earthquake, indicating that the delay time was increased by 0.08 s (Figure 2.15c). We infer the increased delay time to be a change in seismic velocity structure due to fluid redistribution around the fault resulting from a combination of both post-seismic stress relaxation and fault-zone damage induced by the  $M_w$  4.6 earthquake.

## 7.3 Seismic Anisotropy Change

We additionally explore changes in seismic anisotropy properties through rotation of quasi-Rayleigh and quasi-Love wave polarization angles. In our preliminary analysis, we calculated the average noise cross-correlation functions between all components of the seismic noise wavefield between LBNL stations FUM and STY (Figure 2.16). Our result shows that a strong Rayleigh pulse at 0.4 s for both the vertical and radial point-force sources and a Love pulse at 0.3 s for the transverse point-force source are retrieved, which will allow us to investigate temporal changes in seismic anisotropy in this area.

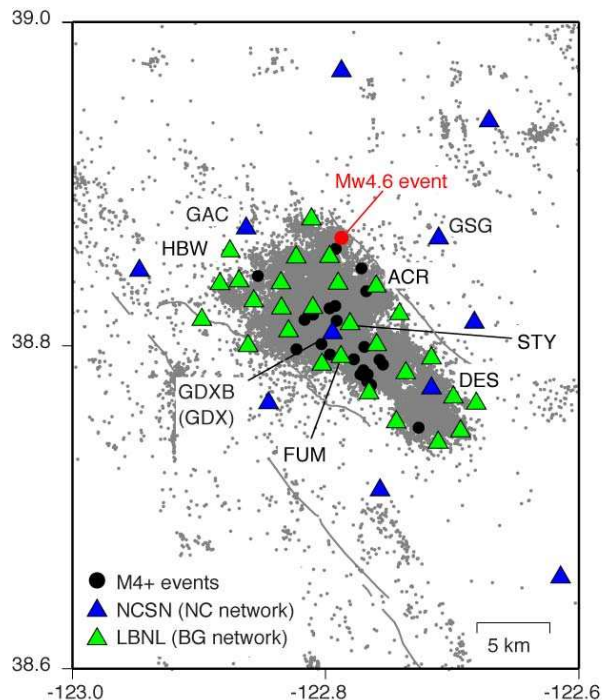


Figure 2.14: Map view of the Geysers area showing the 28 LBNL (green triangles) and USGS (blue triangles) seismic stations. Gray dots are locations of relocated earthquakes in this area during 1984 - 2008 (*Waldhauser and Schaff, 2008*). Also shown are  $M_4+$  earthquakes (solid circles) since 1984. Red circle is the epicenter of the 2006  $M_w$  4.6 Geysers earthquake.

## 7.4 Acknowledgements

We thank P. Cupillard for discussion, and the NCEDC and LBNL for data collection and distribution. This work is supported by the National Science Foundation grant EAR-1053211.

## 7.5 References

Bensen, G.D., M.H. Ritzwoller, M.P. Barmin, A.L. Levshin, F. Lin, M.P. Moschetti, N.M. Shapiro, and Y. Yang, Processing seismic ambient noise data to obtain reliable broadband surface wave dispersion measurements, *Geophys. J. Int.*, 169, 1239-1260, doi:10.1111/j.1365-246X.2007.03374.x, 2007.  
Waldhauser, F. and D. P. Schaff, Large-scale relocation of two decades of Northern California seismicity using cross-correlation and double-difference methods, *J. Geophys. Res.*, 113, B08311, doi:10.1029/2007JB005479, 2008.

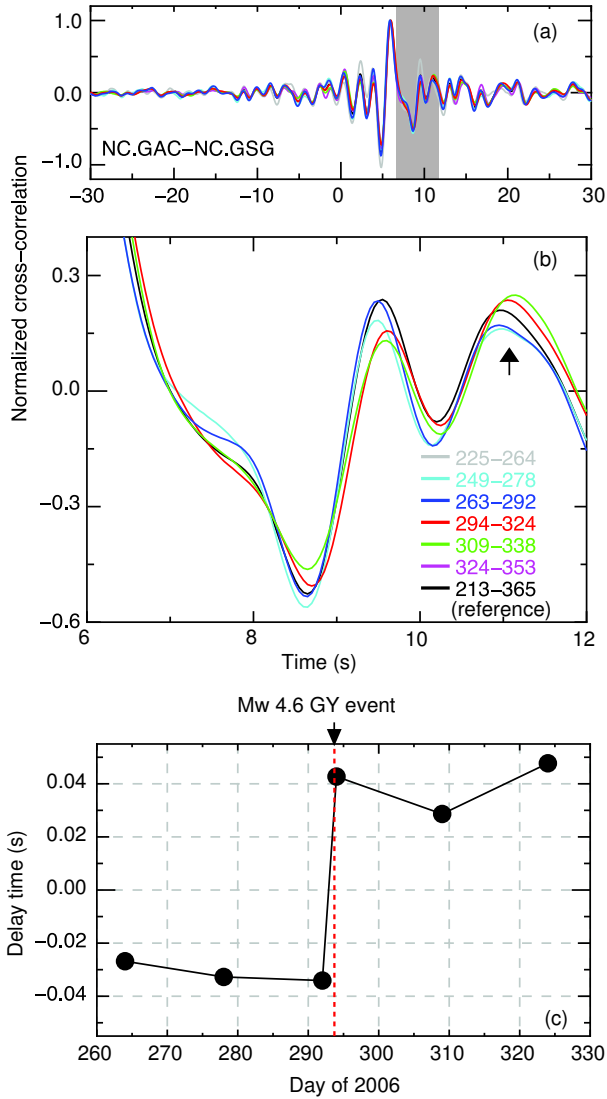


Figure 2.15: Stacked cross-correlation function between stations GAC and GSG. (a) Black waveform is the reference Green's function determined by noise cross-correlation functions during a 5-month period from August to December 2006. Other colored waveforms are stacked 30-day cross-correlation functions. (b) Enlarged view of five noise cross-correlation functions (the reference Green's function and four cross-correlation functions from day of year, 249 through 338), shown in the gray area in Figure 2.15a. Note that a change in cross-correlation function occurred after the 20 October 2006  $M_w$  4.6 Geysers earthquake (day of year 293), which strongly suggests a change in seismic structure associated with this earthquake. (c) Delay time measurement from noise cross-correlation analysis. An abrupt temporal change in delay time is seen around the occurrence of the  $M_w$  4.6 Geysers earthquake.

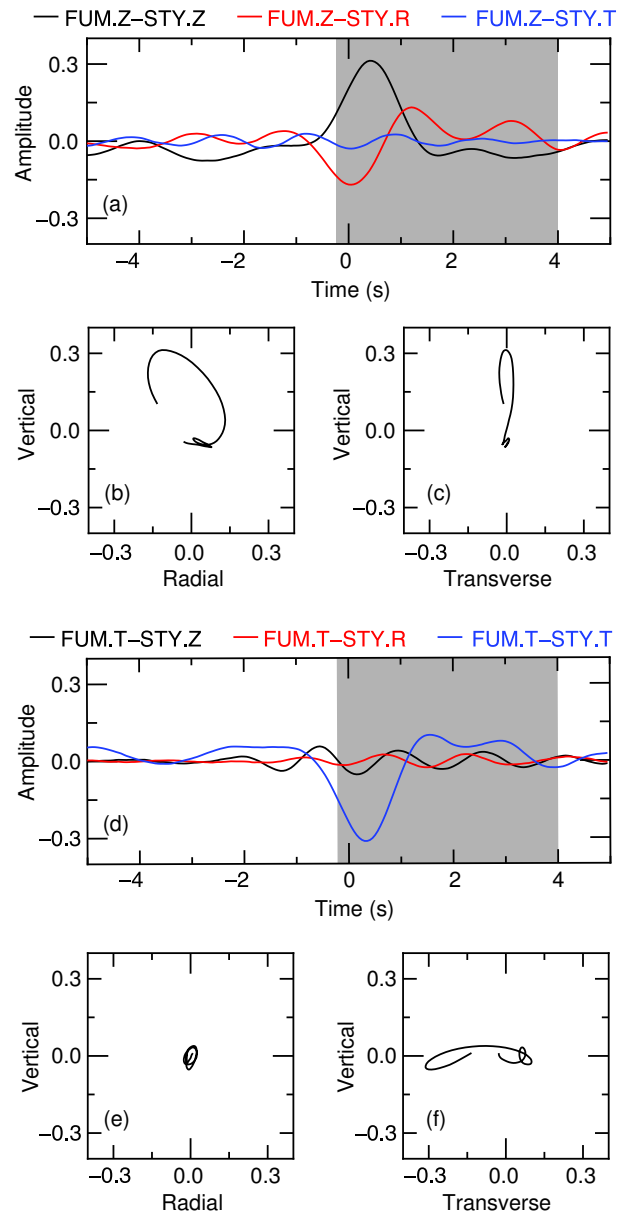


Figure 2.16: Recovered Rayleigh and Love pulses. (a) Measured Green tensor from vertical-component records at station FUM and vertical (black), radial (red), and transverse (blue) component records at station STY. Particle motion plots for (b) vertical-radial and (c) vertical-transverse planes in the gray area in Figure 2.16a. (d) Measured Green tensor from transverse-component records at station FUM and vertical (black), radial (red), and transverse (blue) component records at station STY. Particle motion plots for (e) vertical-radial and (f) vertical-transverse planes in the gray area in Figure 2.16d.

# 8 Measuring Fault-Zone Rheology at Depth from Characteristically Repeating Earthquakes

Taka'aki Taira, Robert M. Nadeau, Douglas S. Dreger

## 8.1 Introduction

Measuring fault-zone rheological properties at *in-situ* conditions is a crucial key to understanding the mechanics of postseismic deformation, aftershocks and the occurrence of triggered earthquakes following larger seismic events. However, it is fundamentally difficult to infer rheological properties at greater depth from surface measurements of strain. Here we introduce a methodology for directly measuring *in-situ* fault-zone rheological parameters at seismogenic depth that makes use of time evolutions of fault creep inferred from time-dependent recurrence intervals and seismic moments of characteristically repeating microearthquakes as deep creepmeters.

## 8.2 Transient Deep Fault Creep Induced by the 2004 Parkfield Mainshock

We observe the deep creep response to the abrupt change of stresses triggered by the 2004  $M_w$  6.0 Parkfield earthquake from time-varying source properties of repeating earthquake sequences. Frequencies of repeating earthquakes in sequences were greatly accelerated by the 2004 Parkfield earthquake. Subsequently they decayed through the stress relaxation process (Figure 2.17a).

Temporal changes in fault creep rate inferred from repeating earthquakes have been thought to be the result of localized transient stress changes near sequences (Nadeau and McEvilly, 2004). In this interpretation, temporal evolutions of inferred stress-driven creep events will be controlled by a single rheological model in the subsequent postseismic period, compared with geodetic measurements of surface displacement that are likely the result of combinations of multiple postseismic relaxation processes such as pore fluid diffusion, frictional slip and viscoelastic stress relaxation. This sensitivity to near-field deformation, in principle, provides a means of directly measuring *in-situ* fault-zone rheological properties.

## 8.3 Modeling Deep Fault Creep

We inverted calculated cumulative seismic slips of the postseismic time series over four years to resolve the rheology model controlling the temporal behavior of the individual fault creep events, using the postseismic relaxation law introduced by Montési (2004). In this constitutive relation in Montési (2004), frictional slip and the viscoelastic relaxation process are the two end-members of the stress-driven creep rheology model that are determined through the estimation of the stress exponent

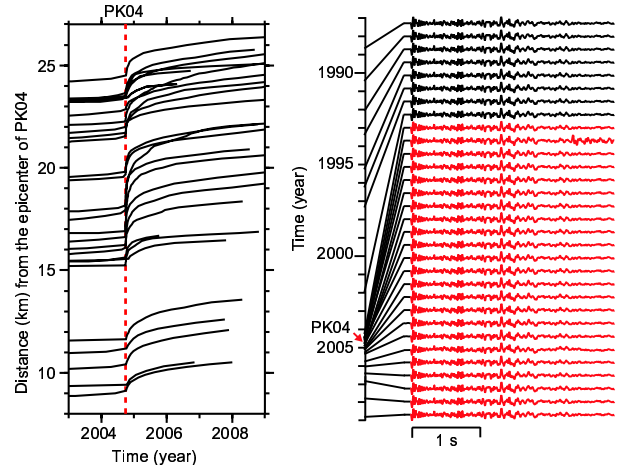


Figure 2.17: (a) Transient deep fault creeps inferred from characteristically repeating earthquake sequences. (b) Waveforms recorded at one of the HRSN borehole stations for one repeating earthquake sequence.

$n$ . For viscoelastic creep,  $n$  ranges from 1 to 4, and for frictional sliding,  $n \gg 1$ .

We utilized six subsets of repeating earthquake sequences that are spatially clustered (Figure 2.18), determining the best-fitting  $n$  and other constants using a simultaneous inversion approach with the assumption that all sequences in individual subsets have the same value of  $n$ , but with different other constants. Of the six subsets, five subsets yield  $n$  larger than 10, indicating that the time evolutions of the inferred fault creep events from those five subsets can be governed by frictional sliding (Figure 2.19). On the other hand, the evolution of the deep fault creep events inferred from the remaining deepest subset shows that it is most consistent with ductile creep ( $2 < n < 4$ ) rather than frictional sliding (Figure 2.20).

## 8.4 Rate-Strengthening Frictional Sliding

We estimated the friction parameter,  $A = a\sigma_n$ , where  $a$  is a constitutive parameter and  $\sigma_n$  is the effective normal stress, surrounding the fault patches in which the characteristically repeating earthquakes occur, with the co-seismic Coulomb stress change ( $\Delta CFF$ ) (Figure 2.18a) based on the source model of the 2004 Parkfield mainshock (Kim and Dreger, 2008). In the rate-

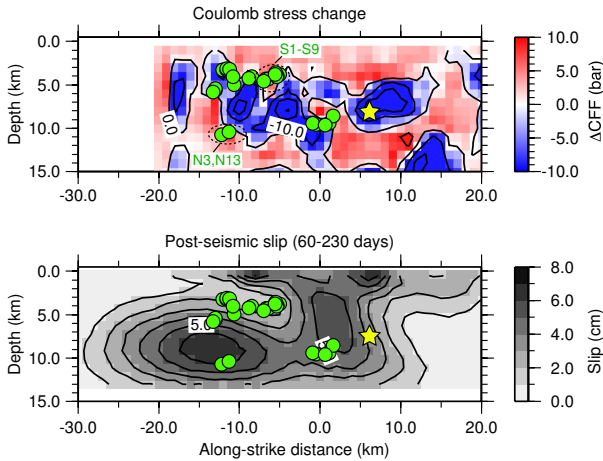


Figure 2.18: Cross-section views of (a) the Coulomb stress change computed from the coseismic model (*Kim and Dreger, 2008*) and (b) the postseismic slip model (*Murray and Langbein, 2006*) between days 60 and 230 of the postseismic period. Green circles are the locations of the repeating earthquake sequences. Yellow star is the hypocenter of the 2004 Parkfield mainshock.

strengthening sliding model in *Perfettini and Avouac (2004)*, the friction parameter  $A$  can be written as  $A = \Delta CFF / \ln(V_+ / V_{pl})$  where  $V_+$  and  $V_{pl}$  are the sliding velocity immediately after the mainshock and the interseismic slip rate. We estimated  $V_+$  and  $V_{pl}$  from time evolutions of seismic slip with a least-squares method for individual subsets. Resulting  $A$  are estimated to be 0.05 to 0.15 MPa.

## 8.5 Viscoelastic Relaxation

Our result shows that the evolution of seismic slips from the deepest subset sequence exhibits viscoelastic creep response (Figure 2.20), suggesting that they may be governed by viscous flow in the ductile lower crust. The resulting 6-cm deep postseismic deformation between days 60 and 230 of the postseismic period near this deepest subset sequence (Figure 2.18b) could be a response to ductile deformation.

## 8.6 Acknowledgements

We thank A. Kim for providing us with the coseismic slip model and J. Murray for the postseismic slip model. This work is supported by the National Science Foundation grant EAR-0910322 and by the USGS NEHRP program under grant number 07HQAG0014.

## 8.7 References

Kim, A. and D.S. Dreger, Rupture process of the 2004 Parkfield earthquake from near-fault seismic wave-

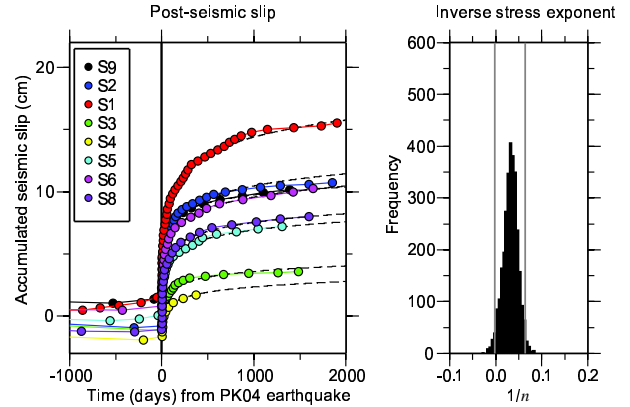


Figure 2.19: (a) Inferred deep fault creeps (circles) from eight clustered repeating earthquake sequences. Dashed lines are predicted fault creeps with the best-fitting  $n$ . (b) Bootstrap distributions for  $n$ , with 3,000 subsample data sets. Gray lines are 95% confidence intervals.

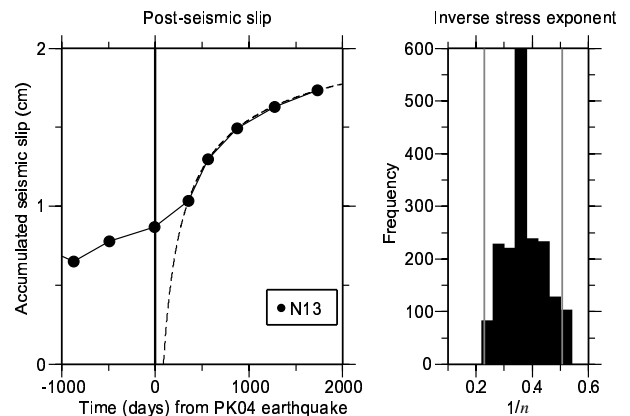


Figure 2.20: Same as Figure 2.19 except for the deep repeating earthquake sequence N13 (focal depth is 10 km).

form and geodetic records, *J. Geophys. Res.*, *113*, B07308, doi:10.1029/2007JB005115, 2008.

Montési, L.G., Controls of shear zone rheology and tectonic loading on postseismic creep, *J. Geophys. Res.*, *109*, doi:10.1029/2003JB002925, 2004.

Murray, J. and Langbein, J., Slip on the San Andreas Fault at Parkfield, California, over two earthquake cycles, and the implications for seismic hazard, *Bull. Seismol. Soc. Am.*, *96*, S283-S303, 2006.

Nadeau, R. M. and T.V. McEvilly, Periodic pulsing of characteristic microearthquakes on the San Andreas Fault, *Science*, *303*, 220-222, 2004.

Perfettini, H. and J.-P. Avouac, Postseismic relaxation driven by brittle creep: A possible mechanism to reconcile geodetic measurements and the decay rate of aftershocks, application to the Chi-Chi earthquake, Taiwan, *J. Geophys. Res.*, *109*, B02304, doi:10.1029/2003JB002488, 2004.

## 9 Free-Surface Vanishing Traction Effects on Shallow Sources

Andrea Chiang and Douglas S. Dreger

### 9.1 Introduction

Waveform inversion to determine the seismic moment tensor is a standard approach in determining the source mechanism of natural and man-made seismicity. The moment tensor is a general representation that includes the double-couple (DC) and non-double-couple sources such as explosions, opening and closing cracks, and volume compensated linear vector dipoles (CLVD). Previous studies (*Ford et al.*, 2009; *Ford et al.*, 2009; *Ford et al.*, 2010) have shown that regional full waveform moment tensor inversion can discriminate isotropic events due to nuclear explosions from other seismic sources such as earthquakes and mine collapses. The method is robust and capable for source-type discrimination applications at regional distances. There can be complications, however, and as part of our continuing efforts to investigate and improve the capabilities of regional full waveform moment tensor inversion for source-type identification purposes, we address the issue of the effect of free-surface vanishing traction on recovering the seismic moment tensor, scalar seismic moment, and explosive yield.

### 9.2 Problem of Vanishing Traction for Shallow Sources

For shallow seismic sources that are effectively at the free surface, the vanishing traction at the free surface will cause the associated Green's function coefficients to have vanishing amplitude (*Julian et al.*, 1998). This results in the indeterminacy of the  $M_{xz}$  and  $M_{yz}$  components of the moment tensor, and bias in the isotropic and total scalar seismic moments.

### 9.3 Source Depth Sensitivity Analysis

Using the Song velocity model (*Song et al.*, 1996), we generate Green's functions at regional distance (100 km) with source depths ranging from 1200 m to 200 m and compute the ten fundamental Green's function time series at each depth. The Green's functions were bandpass-filtered between 10 and 50 seconds period. As shown in Figure 2.21, there is strong source depth sensitivity on the vertical dip-slip (DS) Green's functions associated with the  $M_{xz}$  and  $M_{yz}$  elements for all three components (ZDS, RDS and TDS) in which there is a systematic reduction in displacement amplitude with shallowing source depth. This effect was noted in a study on fundamental Love and Rayleigh waves for nuclear explosions and associated tectonic release (*Given and Mellan*, 1986). In contrast, the vertical strike-slip Green's functions for all three components (ZSS, RSS and TSS) and the explosion Green's functions for the vertical and radial components (ZEP, REP) show little to no variation in amplitude

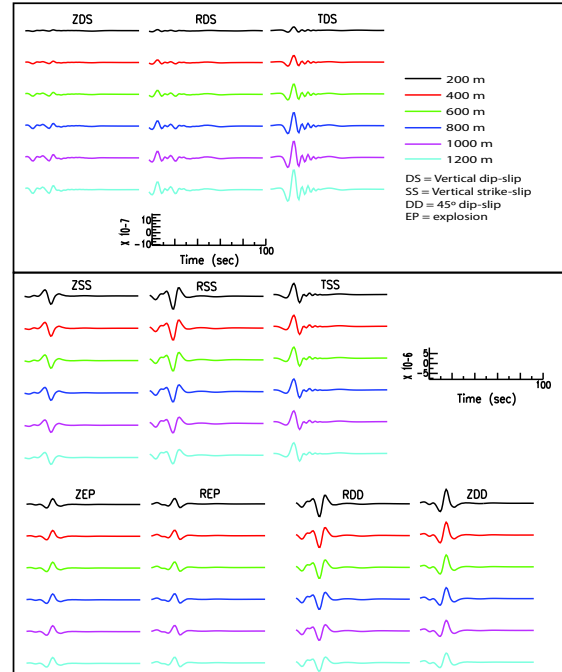


Figure 2.21: Fundamental displacement Green's functions calculated using the *Song et al.* (1996) velocity model and bandpass-filtered between 10-50 seconds. Z, R and T are the vertical, radial and tangential components, respectively.

and waveform. The 45° dip-slip Green's functions (ZDD and RDD) show minor variations in waveforms due to the constructive and destructive interference of waves interacting with the free surface. While this interference appears minor in the 10 to 50 second period passband (Figure 2.21) it is more pronounced in the unfiltered synthetics.

The weak DS component Green's functions can lead to bias in seismic moment tensor results, particularly when noise in the data is considered. However, we note that while there are strong effects on amplitude, the waveforms remain similar and there is little effect on the phase of the waveforms on these components. This suggests that it should be possible to develop correction terms for seismic moment tensor results when source depth is not known. Additionally, it suggests that pure-explosion models should not suffer from the free-surface bias. We will investigate both possibilities by introducing a correctional term to scale the Green's functions for shallow sources prior to the moment tensor inversion, or to incorporate a damping factor in the inversion to minimize the free-surface vanishing traction effect on shallow sources.

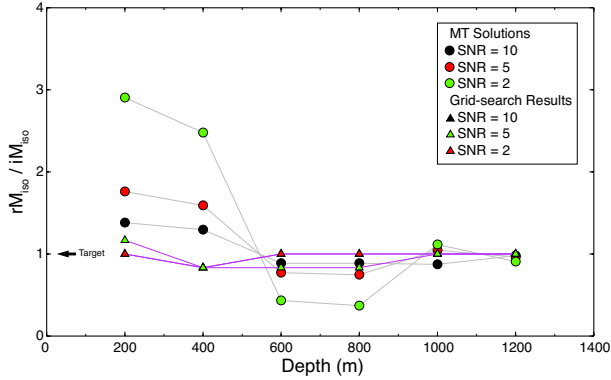


Figure 2.22: Depth sensitivity analysis where the ratios (circle and triangles) between recovered isotropic moment ( $rM_{iso}$ ) and the input value ( $iM_{iso}$ ) are shown over the depth range for different SNR scenarios. Results for SNR of 10 and 5 using the grid-search method overlaps.

## 9.4 Scalar Seismic Moment Sensitivity

A second set of synthetic tests is performed using complete moment tensor inversion (*Minson and Dreger, 2008*) and a grid-search method. This is an attempt to explore the free-surface effects on isotropic moment estimation and hence the yield. Since the vanishing traction at the free-surface shows little effect on the explosion Green’s functions, we expect the inversion to be stable. However, noise and tectonic release associated with the explosion will bias the full moment tensor estimates. Using the same set of Green’s functions calculated in the waveform analysis, we generate synthetic data for a pure explosion case with different signal-to-noise ratios (SNR) by adding random Gaussian white noise. The synthetic data is then inverted using the Green’s functions at the correct source depths, ranging from 1200 m to 200 m.

For a four-station, semi-ideal coverage (source-station distance distributed at regular intervals and in semi-regular azimuths) we see a strong effect on the isotropic moment at depths shallower than 400 m (Figure 2.22) for  $SNR \leq 5$ . At 200 m and 400 m depths, the inversion over-estimates the isotropic moment by a factor of  $\sim 3$ , depending on the SNR. However, the effect diminishes rapidly at depths  $\geq 600$  m, and with relatively good SNR of 5 and 10 the inversion method can recover the isotropic moment, while with an SNR of 2 it is not possible to recover the isotropic moment at depths  $< 1000$  m. Based on the moment tensor analysis, it is possible to recover the isotropic moment for long period waves (10-50 second) with SNR down to 5 at depths  $\geq 600$  m, and possibly shallower sources with a SNR of 10 or at depths  $\geq 1000$  m with a SNR of 2. We also invert the synthetic data using a grid-search method for a pure explosion model at each depth. Using this method, we can recover the isotropic moment at each depth for all three different SNR scenarios (Figure 2.22). In this case, a

simpler explosion model can better recover the isotropic moment.

## 9.5 Conclusions

Preliminary results indicate that the DS Green’s functions associated with the  $M_{xz}$  and  $M_{yz}$  components are affected by the vanishing traction effect at the free-surface, and this leads to biases in the recovered full moment tensor solutions. The amplitude of the Green’s functions decrease systematically, and the waveforms look similar over the targeted depth range with little phase distortion. Initial synthetic testing shows a dependence on source depth and SNR regarding the waveform moment tensor inversion’s ability to recover the isotropic moment of a pure explosion source. The inversion can recover the isotropic moment at all depths with a SNR of 10 and at depths  $\geq 600$  m for a SNR of 5. However, noise and the free-surface have minor effects on the isotropic moment recovery for a simple explosion model using a grid-search method. The next step is to continue testing different velocity models and compare their waveforms, and to introduce a correctional term either applied directly to the Green’s function calculations or in the moment tensor inversion to minimize the vanishing traction effect and improve the stability of the inversion for shallow sources.

## 9.6 Acknowledgements

This work is supported by the Air Force Research Laboratory (Award No. FA9453-10-C-0263).

## 9.7 References

- Ford, S.R., D.S. Dreger, and W.R. Walter, Source analysis of the Memorial Day explosion, Kimchaek, North Korea, *Geophys. Res. Lett.*, *36*, L21304, 2009. doi:10.1029/2009gl040003.
- Ford, S.R., D.S. Dreger, and W.R. Walter, Identifying isotropic events using a regional moment tensor inversion, *J. Geophys. Res.*, *114*, B01306, 2009. doi:10.1029/2008jb005743.
- Ford, S.R., D.S. Dreger, and W.R. Walter, Network Sensitivity Solutions for Regional Moment-Tensor Inversions, *Bull. Seismol. Soc. Amer.*, *100*, 1962-1970, 2010.
- Given, J.W., and G.R. Mellman, Estimating explosion and tectonic release source parameters of underground nuclear explosions from Rayleigh and Love wave observations, *Air Force Geophysics Laboratory Technical Report No. AFGL-TR-86-0171(I)*, 1986.
- Julian, B.R., A.D. Miller, and G.R. Foulger, Non-double-couple earthquakes 1. Theory, *Rev. Geophys.*, *36*, 525-549, 1998. doi:10.1029/98rg00716.
- Minson, S.E. and D.S. Dreger, Stable inversions for complete moment tensors, *Geophys. J. Int.*, *174*, 585-592, 2008. doi:10.1111/j.1365-246X.2008.03797.
- Song, X.J., D.V. Helmberger, and L. Zhao, Broad-Band Modelling of Regional Seismograms: the Basin and Range Crustal Structure, *Geophys. J. Int.*, *125*, 15-29, 1996. doi:10.1111/j.1365-246X.1996.tb06531.

# 10 Moment Tensors for Aftershocks of the M 7.9 Wenchuan Earthquake

Xiangdong Lin and Douglas Dreger

## 10.1 Introduction

On 12 May 2008, a magnitude 7.9 earthquake occurred beneath the steep eastern margin of the Tibetan plateau in Sichuan. This earthquake and its aftershocks caused huge losses in human life and property. To mitigate disasters caused by great earthquakes in the future, it is necessary to study the source properties and triggering mechanisms of the Wenchuan earthquake and its aftershocks. In this study, we use the wave field expression produced by the dislocation of a point source in the lateral layer and the frequency-wavenumber integration (F-K) method (Wang, *et al.*, 1980) to calculate the theoretical surface displacement caused by the earthquake. We obtain the seismic moment tensor solution, using the linear least squares method to minimize the fitting residual between theoretical and observational displacement of the fixed source depth earthquake (Dreger, 1993.)

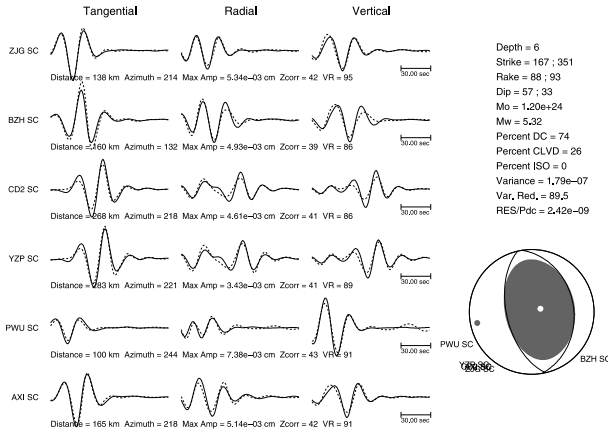


Figure 2.23: The moment tensor solution for the ninth Wenchuan aftershock in our study.

## 10.2 Data

In this study, we collect about 200 high signal-to-noise ratio waveforms (Zheng *et al.*, 2010) ( $M_s \geq 4.0$ ) of Wenchuan series' aftershocks from the local seismic network. The stations involved are the broadband stations within 500 km of the epicenter. We remove the instrument response and trend; integrate the waveforms to displacement; and rotate the three component waveforms into the vertical, radial and tangential direction for the inversion.

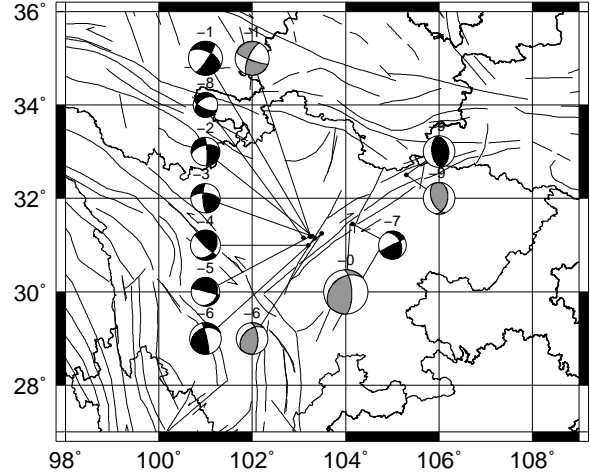


Figure 2.24: Moment tensor solutions for the mainshock and for the nine aftershocks in our study (red beach balls represent moment tensors calculated in this study, while green ones are cited from GCMT solutions.)

## 10.3 Preliminary results

In the vicinity of the 12 May 2008 earthquake, hereafter referred to as the Wenchuan earthquake, the eastern margin of the Tibetan plateau rises steeply westward from 500 m to  $> 4000$  m elevation. Mountain peaks within the Longmen Shan reach elevations higher than 6000 m (Burchfiel *et al.*, 2008). The eastern plateau margin formed by the Longmen Shan coincides with steep gradients in crustal thickness (from 60~65 km in the west to  $\sim 40$  km in the east; Xu *et al.*, 2007) and seismic wave speed changes from slow in the west to fast in the east, showing that the tectonic structure is very complex in this region. Following previous velocity structure study results, we established four 1-D models for the basin area and for the southwest, northeast and northwest mountain areas, respectively. Using these models, we obtained nine aftershock moment tensor solutions (see Figures 2.23 and 2.24.) The moment tensor solutions for aftershocks No. 1, No. 6, and No. 9 in our study are very close to results from the USGS (Figure 2.24.) The rupture plane and the aftershock sequence extend northeast of the Longmen Shan range, and the faulting geometry along the rupture appears to be complex. Reverse and right-slip components are of comparable magnitude along the southwestern portion of the rupture, but right-slip dominates the northeastern portion of the rupture (Zhao *et al.*, 2010). The nine aftershocks solutions also coincide with results

Table 2.1: The catalog of studied earthquakes

No.	Occurrence time	Latitude	Longitude	Magnitude	Depth
1	20080512191100.1	31.18	103.25	$M_S$ 6.0	9
2	20080512230529.3	31.15	103.34	$M_S$ 5.1	13
3	20080512230542.6	31.19	103.28	$M_S$ 5.2	15
4	20080512232852.3	31.00	103.20	$M_L$ 5.3	11
5	20080513012904.4	31.18	103.23	$M_L$ 5.1	9
6	20080513040848.5	31.25	103.49	$M_S$ 5.6	10
7	20080513044530.8	31.45	104.15	$M_S$ 5.0	7
8	20080513050812.1	31.16	103.10	$M_S$ 4.4	6
9	20080724035443.7	32.50	105.30	$M_S$ 5.6	17

from Zhao *et al.*, 2010; earthquakes No. 1~8 have a large strike-slip component, while No. 9 is reverse.

## 10.4 Future work

In the future, we intend to calculate moment tensor solutions for our full set of ~200 Wenchuan aftershock waveforms for use in our investigation of the dynamic crustal characteristics of this area.

## 10.5 Acknowledgements

Waveform data for this study are provided by the Data Management Centre of the China National Seismic Network at the Institute of Geophysics, China Earthquake Administration.

## 10.6 References

Burchfiel, B.C., L.H. Royden, R.D. vander Hilst, and B.H. Hager, A geological and geophysical context for the Wenchuan earthquake of 12 May 2008, Sichuan, People's Republic of China, *GSA Today*, 18(7), doi: 10.1130/GSATG18A.1, 2008.

Dreger, D. Determination of Source Parameters at Regional Distances With Three-Component Sparse Network Data, *J. Geophys. Res.*, 98(B5), 8107-8125, doi:10.1029/93JB00023, 1993.

Xu, L., S. Rondenay, and R.D. Van der Hilst, Structure of the crust beneath the southeastern Tibetan Plateau from teleseismic receiver functions, *Phys. Earth Planet. In.*, 165, 176193, 2007.

Wang, C.Y., L. Zhu, H. Lou, et al., Crustal thicknesses and Poisson's ratios in the eastern Tibetan Plateau and their tectonic implications, *J. Geophys. Res.*, 115, B11301, doi:10.1029/2010JB007527, 2010.

Wang C.Y., R.B. Herrmann, A numerical study of P, SV, SH-wave generation in a plane layered medium. *Bull. Seismol. Soc. Am.*, 70, 1015-1036, 1980.

Zhao CP, ZL Chen, et al., Rupture process of the Wenchuan M8.0 earthquake of Sichuan, China: the segmentation feature, *Chinese Science Bulletin* 55(3), 284-292, doi: 10.1007/s11434-009-0425-7, 2010.

Zheng X.F., Z.X. Yao, J.H. Liang and J. Zheng, The role played and opportunities provided by IGP DMC of China National Seismic Network in Wenchuan earthquake disaster relief and researches. *Bull. Seismol. Soc. Am.*, 100(5B), 2866-2872, doi: 10.1785/0120090257, 2010.

# 11 Focal Depth of the 2008 Panzhihua Earthquake from Depth Phase sPL and Joint Inversion of Local and Teleseismic Waveforms

Jiajun Chong, Zhenjie Wang (USTC), Sidao Ni (KLDG), Barbara Romanowicz

## 11.1 Introduction

On August 30th, 2008, an  $M_s$  6.1 earthquake occurred near Panzhihua city and Huili county, Sichuan Province (hereafter referred to as the Panzhihua earthquake). Proposed to be on the Yuanmou-Lvzhijiang fault, this earthquake sequence provides us an opportunity to study properties of the Yuanmou-Lvzhijiang fault and thus helps us to understand the seismogenic processes of this region. However, there is a controversy over the focal depth of the main shock. The focal mechanisms given by USGS and GCMT are similar, but the focal depths are quite different: 17.0 km and 24.1 km for the USGS and GCMT solutions, respectively. Moreover, some waveform based studies suggest a much shallower depth (Long *et al.*, 2010). Thus, it is important to study focal depths of the Panzhihua earthquake sequence, which may be crucial parameters for constraining the brittle - ductile transition depth in this region and also important for strong ground motion studies. In this study, two approaches are employed to obtain a reliable focal depth of the Panzhihua earthquake. First, whole waveform inversion of local and teleseismic waveforms with CAP (Cut and Paste) method (Zhu and Helmberger, 1996) is used to invert for the focal mechanism and focal depth of the mainshock. Then, a waveform comparison method (WCM) with a recently proposed depth phase sPL (Chong *et al.*, 2010) is verified with the focal depth from waveform inversion. After that, we estimate depths of six  $M_L4+$  aftershocks using the sPL phase observed at a station located about 37 km from the mainshock.

## 11.2 Focal depth and mechanism from waveform inversion

We use a modified version of the CAP method to invert for focal mechanism and focal depth by fitting local and teleseismic waveforms simultaneously (Wang *et al.*, 2011). Local and teleseismic data from the mainshock are collected from 6 local broadband stations and 17 IRIS/GSN teleseismic stations. The velocity model for calculating local and teleseismic Greens functions is constructed by taking the average of a 2D profile from deep seismic sounding in west Panzhihua. It is adjusted so as to try and get the same focal depth from both waveform inversion and depth phase sPL (Wang *et al.*, 2011).

The joint inversion shows that the Panzhihua earthquake is a predominantly strike-slip earthquake, and the best focal depth is 11km (Figure 2.25); at this depth both local and teleseismic datasets are matched by synthetic seismograms very well (Figure 2.26). Our best fault plane solutions (strike/dip/rake) for the mainshock

are, I:  $194^\circ/78^\circ/12^\circ$  and II:  $102^\circ/78^\circ/168^\circ$ ; they are similar to that of USGS (I:  $195^\circ/89^\circ/19^\circ$ , II:  $104^\circ/71^\circ/179^\circ$ ) and GCMT (I:  $190^\circ/90^\circ/4^\circ$ , II:  $100^\circ/86^\circ/180^\circ$ ), but different in dip angle (fault plane I should be the ruptured fault plane according to the fault geometry and the distribution of aftershocks). However, our focal mechanism is closer to the fault geometry according to field studies (Liu, 2008). This suggests that teleseismic waveforms can constrain the dip angle of near vertical faults very well because of their small take off angles. The moment magnitude is 5.9, which is consistent with  $M_w$  6.0 from GCMT, and the minor difference in moment magnitude may be due to inaccurate  $t^*$  used in computing the teleseismic body waves (for our study,  $t^*p$  is chosen to be 1.0 second, and  $t^*s$  is 4.0 seconds, which is usually adopted in teleseismic waveform modeling, Kikuchi and Kanamori, 1982).

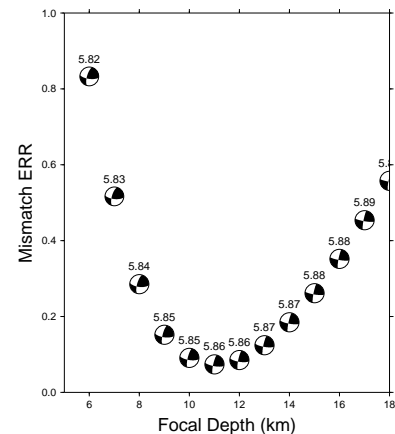


Figure 2.25: Variation of scaled misfit with focal depth in inversion the focal mechanism of the Panzhihua earthquake. Moment magnitude and focal mechanism are shown for each depth as well.

## 11.3 Focal depths from depth phase sPL

sPL is a local seismic phase that is usually well observed in the distance range of less than 50km, depending on the focal depth and velocity structure. The differential time between sPL and direct P is insensitive to epicentral distance but increases almost linearly with focal depth, and it has been successfully used to determine focal depth with only one station at near distance (Chong *et al.*, 2010). With the obvious observations of sPL at station PZH, which is 37km away from the mainshock, we determined focal depths of the mainshock and

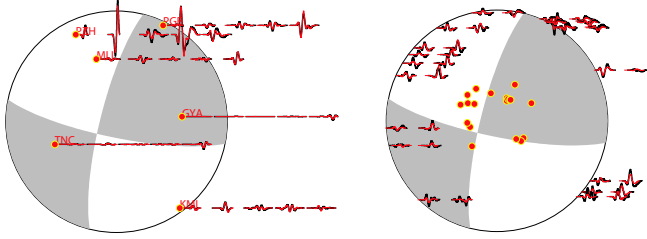


Figure 2.26: Waveform fitting between synthetics (red) and observations (black) for the Panzhihua earthquake with focal depth at 11km for synthetics. (a) Five segments of local waveforms: vertical Pnl, radial Pnl, vertical, radial and tangential surface wave, filtered in the frequency range 0.03~0.1 Hz with a 4th order Butterworth filter. (b) Teleseismic waveforms: vertical P and SH, filtered in the frequency range 0.02~0.1 Hz with 4th order Butterworth filter.

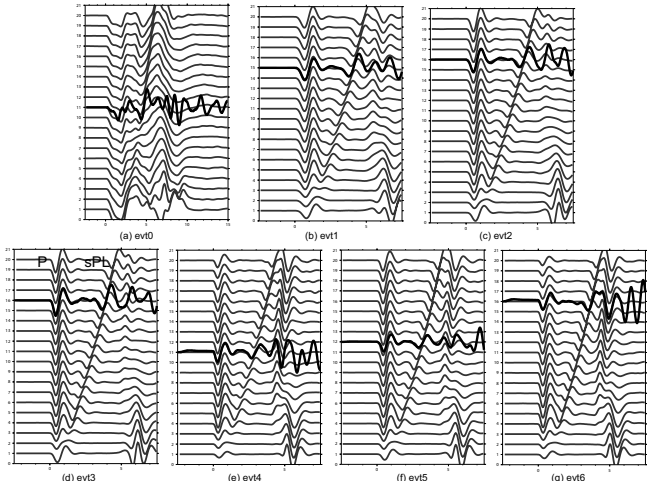


Figure 2.27: Focal depth determination for mainshock and six aftershocks. Radial component waveforms (velocity) are used for waveform comparison by fitting the differential time between sPL and direct P. Gray for synthetics and black for data, filtered in the frequency range 0.01~1 Hz.

Table 1 Focal depths from sPL and from catalog by China Earthquake Network Center (CENC)

Event ID	Origin time (UTC)	Longitude (degree)	Latitude (degree)	Depth from sPL (km)	Depth from CENC (km)	Source duration time (Sec)
Evt_0	2008 08 30 08:30:52	102.06	26.30	11	19	3.5
Evt_1	2008 08 31 08:31:10	102.06	26.27	15	13	1.0
Evt_2	2008 08 31 09:34:49	102.06	26.25	16	12	0.6
Evt_3	2008 08 31 11:00:30	101.99	26.16	16	14	0.4
Evt_4	2008 09 05 08:24:15	101.98	26.23	11	16	0.2
Evt_5	2008 09 30 01:16:38	101.94	26.24	12	13	0.4
Evt_6	2008 10 25 02:13:59	102.01	26.21	16	15	0.2

its six aftershocks following the approach of *Chong et al.* (2010). As shown in Figure 2.27, differential times between sPL and the direct P phase are well fitted for all events. And as a comparison, in Table 1, we see that focal depths of some events such as evt0 (mainshock), evt2, and evt4, from our study are quite different from those of the CENC catalog. Since the differential time between sPL and P is insensitive to epicentral distance but increases almost linearly with focal depth, we can arrange aftershocks in the order of focal depth by comparing the differential times between sPL and P. So, we conclude that evt2, evt3 and evt6 are at almost the same depth and deeper than other events, while evt0 and evt4 are at almost the same depth but shallower than the other earthquakes.

## 11.4 Conclusions

Our study indicates that the focal depth of the mainshock of the 2008 M6 Panzhihua earthquake sequence can be well constrained with two approaches: (1) using the depth phase sPL and (2) using whole waveform inversion of local and teleseismic data. We also show that precise focal depths of aftershocks can be determined using the depth phase sPL with only one broadband seismic station. Our study indicates that the mainshock is located at a depth of 11km, which is much shallower than those from other studies, confirming that the earthquake occurred in the upper crust. Aftershocks are located in the depth range 11-16 km, which is consistent with a ruptured near-vertical fault whose width is about 10 km, as expected for an M6 earthquake.

## 11.5 Acknowledgements

Supported by China Earthquake Administration fund 200808078, and NSFC funds 40821160549 and 41074032

## 11.6 References

Chong, J.J., Ni, S.D., Zeng, X.F., sPL, an effective seismic phase for determining focal depth at near distance, *Chinese J. Geophys.*, (in Chinese), 53, 2620-2630, 2010

Liu, M.F., A Study on Genesis of Hongge Hot Spring in Yanbian, Sichuan Province, *Coal Geology Of China*, (in Chinese), 20, 45-48, 2008

Long, F., Zhang, Y.J., Wen, X.Z., Ni, S.D., Focal mechanism solutions of  $M_L \geq 4.0$  events in the  $M_s 6.1$  Panzhihua-Huili earthquake sequence of Aug 30, 2008, *Chinese J. Geophys.*, (in Chinese), 53, 2852-2860, 2010

Kikuchi, M., and Kanamori, H., Inversion of complex body waves, *Bull. Seismol. Soc. Am.*, 72, 491-506. 1982

Wang, Z.J., Chong, J.J., Ni, S.D., Romanowicz, B., Determination of focal depth by two waveform based methods, a case study for the 2008 Panzhihua earthquake, *Earthquake Science*, (accepted)

Zhu, L.P., Helmberger, D.V., Advancement in source estimation techniques using broadband regional seismograms, *Bull. Seis. Soc. Am.*, 86, 1631-1641, 1996

# 12 Deviatoric Moment Tensor Analysis at The Geysers Geothermal Field

Sierra Boyd, Douglas Dreger, Sean Ford (LLNL), Peggy Hellweg, Peter Lombard, Jennifer Taggart, and Tom Weldon

## 12.1 Introduction

Geothermal energy has been produced at The Geysers Geothermal Field in Northern California for more than forty years. It has been demonstrated that increased steam production and fluid injection correlates positively with changes in earthquake activity, resulting in thousands of tiny earthquakes each year with events ranging in magnitude up to 4.5. We determine source parameters for the largest of these earthquakes using a regional distance moment tensor method. We invert three-component, complete waveform data from broadband stations of the Berkeley Digital Seismic Network for the complete, six-element moment tensor. Some solutions depart substantially from a pure double-couple (DC), with some events having large volumetric components.

Care is needed in the assessment of the significance of the non-double-couple terms. We have worked to develop a systematic procedure for the evaluation of aleatoric and epistemic solution uncertainty (e.g. Ford *et al.*, 2009; Ford *et al.*, 2010). We will present the solutions for The Geysers events together with estimates of random errors and systematic errors due to imperfect station coverage and knowledge of the velocity structure, which are needed to compute Green's functions for the inversion. Preliminary results indicate that some events have large isotropic components that appear to be stable and suggestive of fluid or gas involvement during the rupture processes.

We are presently working to incorporate full moment tensor capability in the Berkeley Seismological Laboratory's automatic processing system and analyst interface. This upgrade will enable improved monitoring at The Geysers and volcanically active regions of California.

## 12.2 Methodology

In this investigation, two source models, namely a deviatoric moment tensor (DC + compensated linear vector dipole [CLVD]) and a full moment tensor (DC+CLVD+isotropic component [ISO]), are evaluated as possible source mechanisms for three M4+ events. The objective is to determine the best fitting source model, and then evaluate the significance and resolution of possible non-double-couple source types that might arise from fluid-related processes in the geothermal system.

We start by determining the deviatoric moment tensors for a range of possible source depths, from 2 to 11 km, using six seismic stations as shown in Figure 2.28. These stations provide good coverage of the focal sphere,

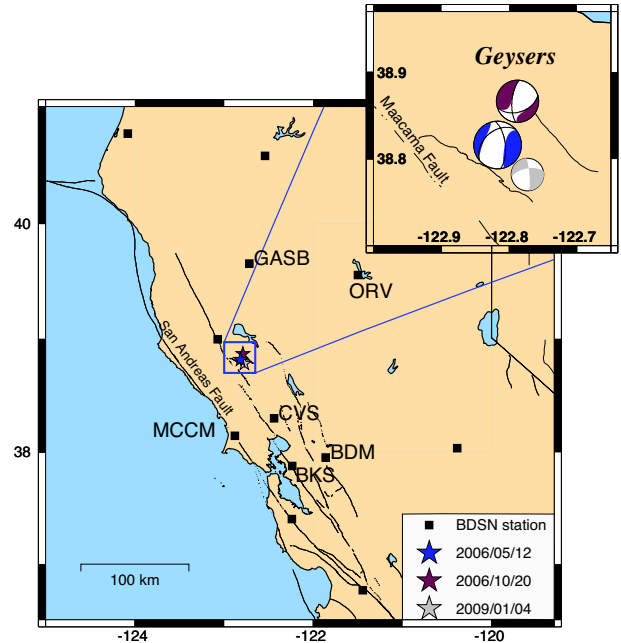


Figure 2.28: Map showing BDSN stations (squares) and analyzed Geysers events (colored stars).

and were chosen based on their signal to noise levels and availability for all the studied events to better enable event-to-event comparison.

We found that depth sensitivity using data filtered between 0.02 to 0.05 Hz is limited, so we therefore restrain our analysis to event depths determined from the Northern California Seismic System and Lawrence Berkeley National Laboratory catalogs. Following the determination of best-fit solutions for each category, we then evaluate the solutions using a battery of statistical, error estimation, and solution sensitivity tools. These tools include the statistical F-Test to evaluate the significance of improved fit with higher degrees of freedom in more complex source models, a bootstrap procedure to estimate aleatoric uncertainty, a station Jackknife test to assess solution stability and to possibly identify problematic source-receiver paths where additional velocity model calibration may be warranted, and tests using Green's functions for different velocity models. These tests provide good assessments of random (aleatoric) uncertainty as well as systematic or model (epistemic) uncertainties. This report explores the relevance of various source models, focusing on the Jackknife test and F-Test portion of this analysis.

## 12.3 Data Processing

Three M4+ earthquakes have been studied thus far with this battery of tests. The events occur on May 12, 2006, October 20, 2006 and January 4, 2009. We restrain the depths of the analysis to 3.5 km for the 2006 events and 4.5 km for the 2009 event.

Broadband seismic data are recorded from a sparse network operated by UC Berkeley. Five minutes of velocity data are downloaded from the Northern California Earthquake Data Center (NCEDC) for six stations ranging in distance from 55 to 140 km from the events of interest. The stations include BDM, BKS, CVS, MCCM, ORV, and GASB. Preprocessing of the seismic data includes removing the instrument response, integrating to ground displacement and filtering the data between 0.02 and 0.05 Hz. Synthetic waveforms are generated using FKRPROG, written by Chandan Saikia, and the GIL7 1D velocity model (e.g., *Pasyanos et al.*, 1996) and filtered between 0.02 and 0.05 Hz with an acausal Butterworth filter.

## 12.4 Deviatoric moment tensor analysis

The deviatoric moment tensor solution is composed of double-couple (DC) and compensated linear vector dipole (CLVD) components. The deviatoric moment tensor solutions derived from six stations show differences in the percentage of the non-double-couple component, with the highest percentage for the May 12, 2006 event. This event also has the lowest variance reduction. The deviatoric solutions for the 2006 events are shown in Figure 2.28.

The stability of the deviatoric moment tensor solutions is investigated with a Jackknife test using all possible groups of 5-, 4- and 3-stations. There are six groups of 5 stations, fifteen groups of 4 stations and twenty groups of 3 stations. The 5-station Jackknife analysis shows minor differences in the weighted variance reduction and percent double couple compared to the 4- and 3-station Jackknife plots. The fluctuations seen in the 4- and 3-station Jackknife plots may arise from imperfect station coverage and a velocity model that may not be ideal for all event-station paths. The variations are more evident when particular stations are grouped together.

Deviatoric	6-sta	5-sta	4-sta	3-sta
05-12 2006				
VRw%	77.6	78.1±1.6	78.7±2.3	79.7±3.3
%DC	30	31±5	31±9	34±14
10-20 2006				
VRw%	82.6	83.1±1.3	83.8±1.8	84.9±2.2
%DC	65	66±7	67±12	67±14
0-04-2009				
VRw%	81.8	82.8±1.8	84.0±2.6	85.7±3.5
%DC	67	68±6	68±10	69±14

The Jackknife analysis suggests overall stability in the deviatoric moment tensor solutions with fluctuations above and below mean trends, with consistently lower values of VRw and percent double-couple for the May 12, 2006 event.

## 12.5 Full moment tensor analysis

The 6-element full moment tensor solution includes the isotropic component and is representative for source processes with a volumetric response. The fits are higher when more degrees of freedom are used compared to the deviatoric solutions. The full moment tensor solutions for the 2006 events show higher percentages of non-double-couple components compared to the 2009 event. However, the F-Test reveals that the full moment tensor solution is somewhat significant for only the October 20, 2006 event, with a 91 percent confidence level of significance. A Jackknife test of this event shows the isotropic component to be stable at slightly above 40 percent for all groups of 5-, 4- and 3-stations, as shown below. In summary, the October 20, 2006 event exhibits a stable and somewhat significant (91% confidence level of significance) isotropic component of approximately 42 percent.

Full solution	6-sta	5-sta	4-sta	3-sta
10-20-2006				
VRw%	85.3	85.8±1.4	86.5±1.9	87.6±2.3
%DC	47	43±10	46±10	43±10
%CLVD	10	15±10	12±10	15±10
%ISO	43	42±2	43±2	42±3

Other models considered were the pure DC and DC+ISO. F-test results show the DC model to be most appropriate for the 2009 event. This initial analysis defines the framework with which we will determine and review moment tensor solutions for M>3 seismicity occurring in the region.

## 12.6 Acknowledgements

This work was supported by the Assistant Secretary for Energy Efficiency and Renewable Energy, Office of Geothermal Technologies, of the U.S. Department of Energy under Contract No. DE-EE0002756.

## 12.7 References

- Ford, S.R., D. S. Dreger, and W. R. Walter, Identifying isotropic events using a regional moment tensor inversion, *J. Geophys. Res.*, 114, B01306, 2009.
- Ford, S.R., D. S. Dreger, and W. R. Walter, Network Sensitivity Solutions for Regional Moment-Tensor Inversions, *Bull. Seism. Soc. Am.*, 100, 1962-1970, 2010.
- Pasyanos, M. E., D. S. Dreger, and B. Romanowicz, Toward real-time estimation of regional moment tensors, *Bull. Seism. Soc. Am.*, 86, 1255-1269, 1996.

# 13 Slip Transients, Deficit and Release from Repeating Earthquakes

Robert M. Nadeau and Ryan C. Turner

## 13.1 Introduction

To better understand interactions between seismic and aseismic deformation, deep aseismic fault slip rates (Vd) from characteristically repeating microearthquake sequences (CS) (Nadeau and McEvilly, 1999) along the central San Andreas Fault (SAF) were compiled and analyzed. Previous CS based Vd studies have shown that spatial and temporal variations in Vd can be resolved over large contiguous regions, in diverse tectonic settings, and back in time to well before the advent of satellite-based geodesy (e.g., GPS, InSAR) (Nadeau and McEvilly, 1999 and 2004; Bürgmann et al., 2000; Igarashi et al., 2003; Chen et al., 2008). Such studies have also revealed systematics in Vd indicative of slip transients associated with post-seismic deformation, slow-slip events, quasi-periodic slip pulsing, and regions of slip-deficit accumulation.

## 13.2 Activities

We searched for CSs along a 200 km stretch of the SAF in Central California and identified and compiled a catalog of 343 CSs comprised of 2854 microearthquakes ranging in magnitude from 1.5 to 3.5 and occurring over a 27.333 year period between 1984 and April of 2011 (inclusive). The CSs were located between the approximate southern terminus of the 1989 M6.9 Loma Prieta (LP) and the northern terminus of the 1857 M7.8 Ft. Tejon (FT) earthquakes, and the catalog includes CS activity associated with the 2004 M6.0 Parkfield earthquake (PF) rupture, its aftershock zone, and the aftershock zone south of the LP earthquake rupture.

We used the method of Nadeau and McEvilly (2004) to convert the the locations, times and magnitudes of the CS micro-events to map the time histories of Vd within the study region.

## 13.3 Findings

Figure 2.29 shows profiles of the CS derived short- and long-term Vd behavior in the study zone in the context of the spatio-temporal distributions of the 1989, M6.9 LP and 2004, M6.0 PF earthquake rupture zones. The locked (inferred rupture) zone associated with the 1857, M7.8 FT earthquake occurs immediately to the southeast.

Moving northwestward from 20 km along the long-term profile (left), a sharp reduction in long-term Vd is observed at  $\sim 95$  km. This corresponds to the bifurcation of the SAF system into the SAF and the sub-parallel Calaveras fault (not shown) strands. The sum of long-

term rates on these strands is comparable to the tectonic plate rate ( $\sim 3.0$  to  $3.5$  cm/yr), consistent with the sharing of tectonic load release by the strands.

Between 20 and 95 km, no significant difference between long-term Vd before PF (pre-PF) and Vd for the entire study period are observed. However, southeast of 20 km, long-term pre-PF rates are lower and are below the plate rate, indicating slip deficit accumulation. The reduced pre-PF rates are also apparent in the short-term contoured profile. Following PF, short-term Vd increases dramatically in the PF rupture and after-slip zones. By April 2011, long-term Vd southeast to  $-15$  km has caught up to the plate rate. A similar pattern is seen in the LP after-slip zone northwest of  $\sim 125$ km, suggesting a general pattern where slip deficit accumulates and releases both seismically (on rupture zones) and aseismically (on adjacent regions). This has important implications for estimating the dimensions of future earthquake rupture and magnitude from inter-seismic patterns of slip deficit accumulation or paleoseismic observations of fault slip from past earthquakes.

Southeast of  $-15$  km, long-term Vd lags behind the plate rate. Our search also revealed no CSs in the  $-35$  to  $-50$  km segment that was included in the 1857 FT rupture zone. This suggests considerable seismic and aseismic slip release in a future large event which, if it happened today, would average  $\sim 4.5$  meters of seismic slip.

## 13.4 Acknowledgements

Research supported by NSF grant EAR-0951430. Data provided by the Northern California Earthquake data center (NCEDC).

## 13.5 References

- Nadeau, R.M., and T.V. McEvilly, Fault slip rates at depth from recurrence intervals of repeating microearthquakes, *Science*, 285, 718-721, 1999.
- Nadeau, R. M. and T. V. McEvilly, Periodic Pulsing of Characteristic Microearthquakes on the San Andreas Fault, *Science*, 303, 220-222, 2004.
- Bürgmann, R., D. Schmidt, R.M. Nadeau, M. d'Alessio, E. Fielding, D. Manaker, T.V. McEvilly, and M.H. Murray, Earthquake Potential along the Northern Hayward Fault, California, *Science*, 289, 1178-1182, 2000.
- Igarashi, T., T. Matsuzawa and A. Hasegawa, Repeating earthquakes and interplate aseismic slip in the northeastern Japan subduction zone, *J. Geophys. Res.*, 108, 2249, doi:10.1029/2002JP001920, 2003.
- Chen, K. H., R.M. Nadeau and R.-J. Rau, Characteristic repeating earthquakes in an arc-continent collision boundary zone: The Chihshang fault of eastern Taiwan, *Earth Planet. Sci. Lett.*, 276, 262-272, doi:10.1016/j.epsl.2008.09.021, 2008.

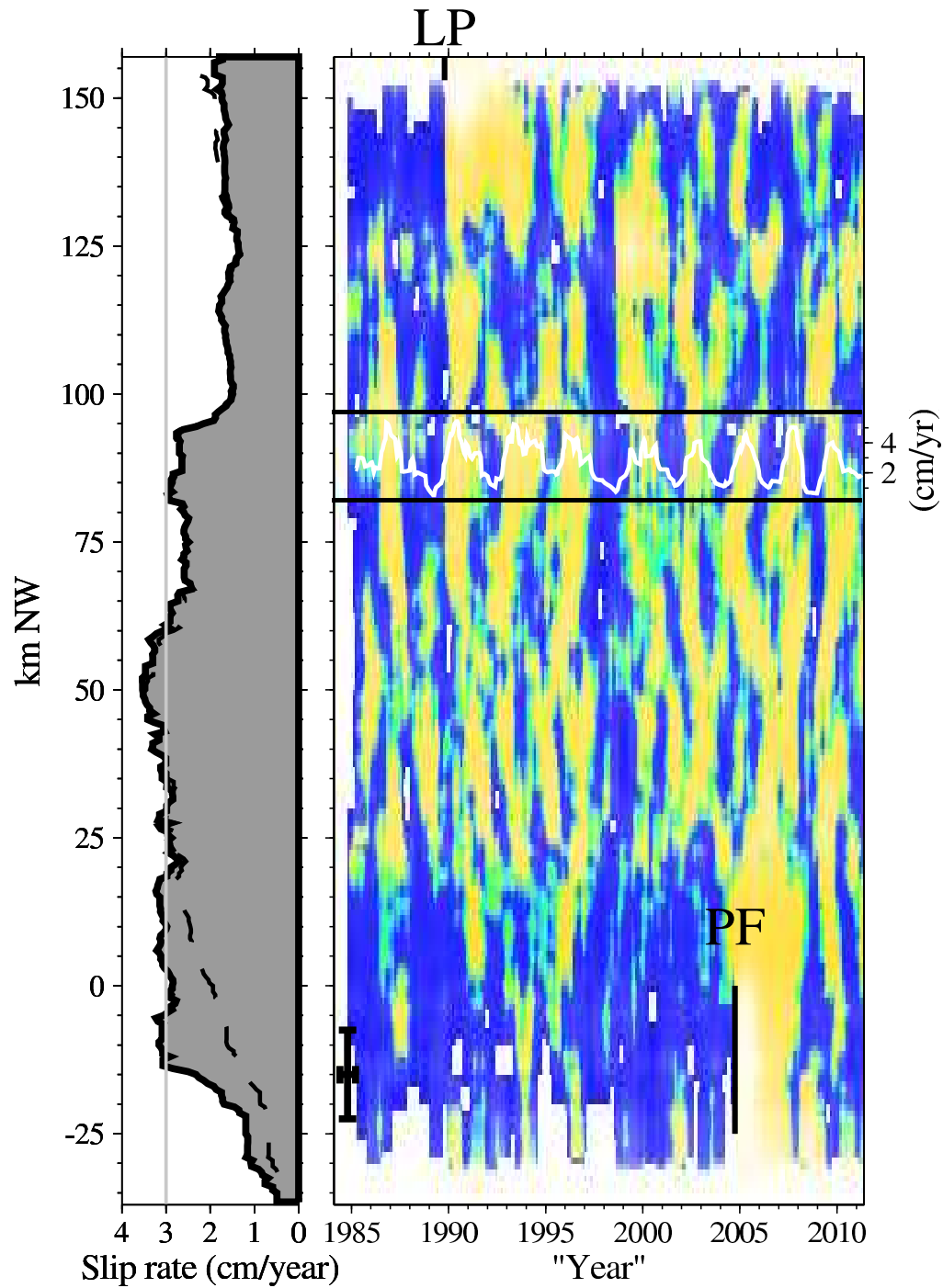


Figure 2.29: Profiles of the short- and long-term  $V_d$  behavior in the study zone in the context of the spatio-temporal distributions of the M6.9 LP and M6.0 PF earthquake rupture zones. The locked (inferred rupture) zone associated with the M7.8 FT earthquake occurs immediately to the southeast. Left panel: profiles of long-term  $V_d$  (15 km smoothing) along the SAF for the entire observation period (solid black curve with grey fill) and for the period preceding the 2004 PF event (dashed black curve). Thin gray line represents a tectonic plate-rate of 3.0 cm/yr. Right panel: colored/contoured profile of % variations in short-term  $V_d$  (0.8 year averaging window) relative to the long-term average (entire observation period). Light gray (yellow) regions show periods when short-term  $V_d$  exceeds the long-term average by 20% or more. Dark gray (blue) regions show periods when long-term rate is below average, and intermediate gray (blue-green) regions are those with  $V_d$  within  $\pm 20\%$  of average. Rupture zones of PF and LP events within the study area are black vertical lines, and the slip rate history (in cm/yr.) of a 15 km segment (centered at  $\sim 90$  km) with nine cycles of particularly periodic aseismic slip-transient pulsing is shown with a white curve.

# 14 Immediate Triggering of Small Repeating Earthquakes at Parkfield

Kate Huihsuan Chen (National Taiwan Normal Univ.), Roland Bürgmann, Robert M. Nadeau

## 14.1 Introduction

We analyze 112 M -0.4  $\sim$  3.0 repeating earthquake sequences (RESs) to examine the triggering effect from nearby microseismicity. For each RES event, the time difference (DT) with all other earthquakes within a distance of 5 km is considered, together with the stress change induced by preceding neighboring events (preshocks) and vice versa for events following the RES events (postshocks). We use the moment of RES and background events in the stress calculation (Equation 2.1) for the postshocks (DT < 0) and preshocks (DT > 0), respectively. Here we introduce a simple expression for the static shear stress change ( $\Delta\sigma$ ) (Aki and Richards, 1980):

$$\Delta\sigma = 1/6\pi M_o/r^3, \quad (2.1)$$

where  $r$  is the distance from a RES to the hypocenter of each neighboring event (with seismic moment  $M_o$ ). Empirical tests using the shear stress change calculated from an elastic-dislocation model (Okada, 1992) produce values of in-plane stress changes consistent with Equation 2.1. In this calculation, we assume that all earthquakes lie on a single plane and thus increase stress on their neighbors, which is clearly not always the case.

## 14.2 Short-term triggering by nearby events

The number and occurrence rate of events appears to be increased for DT  $\leq$  5 days, suggesting an apparent preponderance of triggering events over small time spans for both pre-RES events and postshocks. In 2.30a, we plot short-DT > 1kPa preshocks and postshocks showing clear evidence of immediate triggering by and of very close-by events. The close-by background events have a large magnitude range, as shown in Figure 2.30b. A cluster of M2 events occurs very close to the RESs in space and time, as illustrated by the circles near (0,0), whereas the M3 and M4-5 events do not show such an obvious tendency. This suggests that in the DT  $\leq$  1 window, very high stress changes are likely a result of small earthquakes triggering others over very short distances.

A remarkable difference between the number of preshocks and postshocks appears if only events with higher stress change are considered, as illustrated by the measures for the events with > 1 kPa stress in Figure 2.30c. The > 1 kPa preshocks are much more frequent within 5 days preceding the RES (solid line with filled square), whereas the rate of postshocks does not show much change with time following the RES (solid line with open circle). Given that the events used to determine

stress change in the preshock and postshock domains are background seismicity and repeating events (smaller magnitude in general), the larger number of higher stress changes for preshocks may be expected. After the 5-day time window, both  $\geq$  1-kPa preshocks and postshocks exhibit a similar occurrence rate, as shown by the similar slope of the solid lines in Figure 2.30c. Additionally, the event rates reveal a systematic decrease out to 30-300 day windows.

Do the trigger stresses need to be of a certain magnitude to lead to immediate triggering? To answer this, the data number in the varying DT window (<5000s, 5000s-1 day, 1-10 days, 10-20 days, 20-30 days, and 30-300 days) is divided by the total number of >1 kPa events. The percentage of high stress change preshocks is the greatest for the DT<5000 s window, with declining percentages for longer DT intervals. The largest difference in data percentage between DT< 5000s and  $\geq$  1 day, 30%, appears at log stress = 1.5 ( $\sim$  30 kPa), whereas the difference among the DT $\geq$  1 day windows is less than 7%. This may suggest that a stress increment of  $\sim$  30kPa or more is needed to produce effectively immediate triggering (DT $\leq$  1 day) of RES events.

## 14.3 Conclusion

We examined interactions between RESs and nearby earthquakes at a fine scale in an attempt to identify systematic interaction and to infer the possible physics behind it. The joint occurrence of RESs and nearby background earthquakes indicates that short-term triggering (<10% of its own average recurrence interval) between neighboring events may be taking place and influencing the timing of repeating events. Immediate triggering within a few seconds to minutes can happen when the separation distance is less than a few km. When earthquakes are separated by longer distances, their communication (triggering) becomes less efficient. An apparent preponderance of triggering of RES events over time spans as small as one day is more evident when the stress change imposed on the RES site is higher than  $\sim$  30 kPa.

## 14.4 References

- Aki, K., and P. G. Richards (1980), *Quantitative Seismology*, Freeman, New York.
- Chen, K. H., Bürgmann, R., and Nadeau, R. M. (2010), Triggering effect of M 4-5 earthquakes on the earthquake cycle of repeating events at Parkfield, *Bull. Seismol. Soc. Am.*, 100, 2, doi:10.1785/0120080369.
- Okada, Y. (1992), Internal deformation due to shear and tensile faults in a half space, *Bull. seismol. Soc. Am.*, 82, 1018-1040.

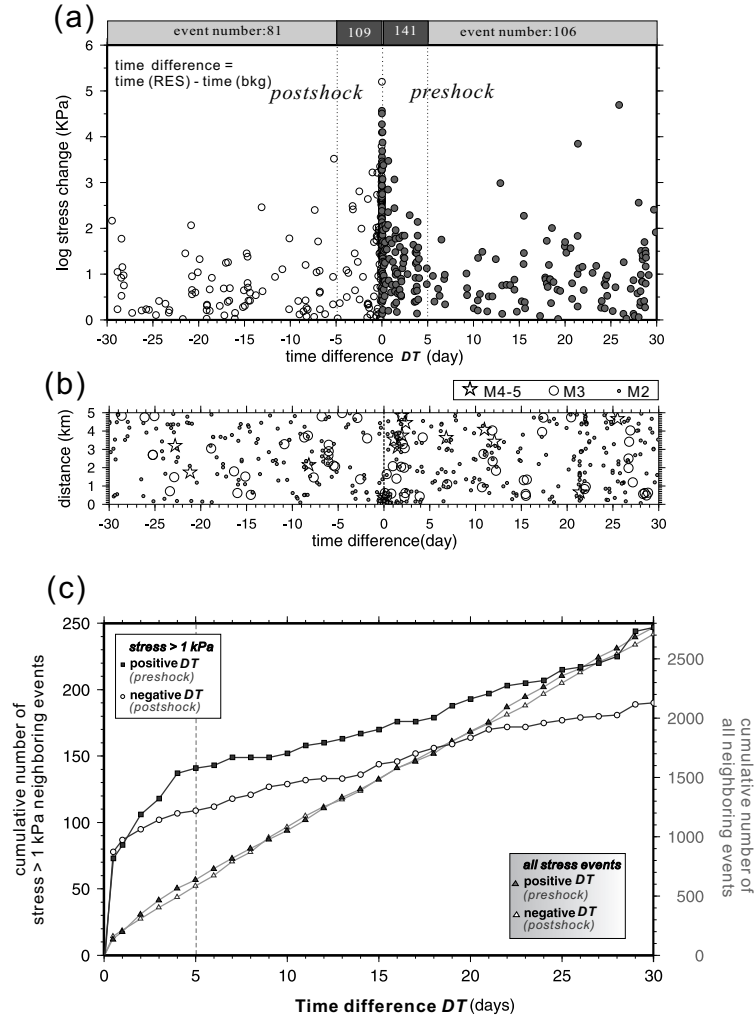


Figure 2.30: (a) Static stress change as a function of time difference between repeating events and nearby non-repeating background earthquakes (bkg) within 5 km distance. Stress changes computed in the postshock case are those imposed by the RES on the subsequent events, whereas in the preshock case the stress changes are those imposed on the RES event. The labels in the upper panel indicate the number of nearby events with stress changes  $> 1$  kPa within 5 days and 5-30 days following/preceding the RES shown by circles. The total number of preshocks and postshocks within 30 days and 5 km from all RES events (without considering their stress change) are 2763 and 2708, respectively. (b) Separation distance versus time difference between RESs and nearby  $M4 \sim 5$  (star),  $3 \leq M \leq 4$  (circle), and  $2 \leq M < 3$  (square) non-repeating events. (c) Cumulative number of background events with increasing time difference  $DT$  from RES events for preshocks and postshocks, as denoted by solid triangles and open triangles with dashed line, respectively. The measures for the events with higher stress changes ( $> 1$  kPa) are shown by a solid line, where the solid square and open circles denote the preshocks and postshocks, respectively. There is a large number of stress  $> 1$  kPa preshocks within 5 days of impending RES (solid squares) events, as shown by vertical dashed line. There are somewhat more high-stress preshocks than postshocks associated with the RES events during that period, which may partly be due to the smaller average magnitude of the RES events.

# 15 Joint Inversion of Seismic and Geodetic Data for the Source of the 4th March 2010 $M_w$ 6.3 Jia-Shian, SW Taiwan, Earthquake

Mong-Han Huang, Douglas Dreger, Seung Hoon Yoo, and Roland Bürgmann

## 15.1 Introduction

The 4th of March 2010 Jia-Shian ( $M_w$  6.3) earthquake occurred in southwestern Taiwan and caused moderate damage. Compared with other  $M_w$  6+ events in the world (e.g. 2004  $M_w$  6.1 Parkfield earthquake), this event has a smaller coseismic slip and no fault related surface rupture, reflecting an unusually deep source in west Taiwan. The reported focal depth is 23 km, below the fold and thrust belt of Taiwan. In this study, we inverted geodetic (GPS and InSAR) and seismic waveform (strong motion and broadband) data for finite-source models. We compare inversions from each individual data set to better understand their respective contributions and to determine the appropriate weights and smoothing parameters for a joint inversion. A joint inversion of the geodetic and seismic data reveals a preferred model that shows a primary slip patch that is approximately 20 km in diameter with a peak slip of 28 cm and total scalar seismic moment of  $3.65 \times 10^{25}$  dyne cm ( $M_w$  6.34).

## 15.2 Inversion and Preliminary Result

We use a linear least squares inversion code based on the method of *Hartzell and Heaton* (1983) in which the finite source is discretized with a finite distribution of point sources in both space and time. A damped, linear least squares inversion with a positivity constraint (allowing only for thrust dip-slip component) is used to determine the spatiotemporally distributed slip. A single time window is used with a fixed dislocation rise time (0.5 s) propagating away from the hypocenter with a constant rupture velocity (2.6 km/s). A spatial smoothing with linear equations minimizing differences in slip between subfaults is applied to stabilize the seismic and geodetic inversion. Different weighting and smoothing parameters are applied to the simultaneous inversion using the method proposed by *Kaverina and Dreger* (2002). The Green's functions for southern Taiwan are taken from *Chi and Dreger* (2004). For the geodetic inversion, the geodetic Green's functions are computed by assuming the same layered elastic structure as for the seismic inversion. A  $50 \times 50$  km NW dipping fault geometry with 625 subfaults was considered for the inversions. The coseismic slip distribution is estimated from the inversion of each data set separately and jointly.

Eight strong motion and three broadband seismic stations are used for the seismic inversion, and 108 GPS stations and three ALOS PALSAR interferograms are used for the geodetic inversion. Both geodetic and seismic in-

versions reveal a consistent pattern for the main rupture asperity near the hypocenter (Figure 2.31b). The joint inversion shows a coseismic slip covering a  $15 \times 20$  km area northwest of the hypocenter with an average slip of 15 cm and a peak slip of 28 cm.

## 15.3 Discussion and Future Work

Both seismic and geodetic inversions obtain good fits to the data, but the predicted moment magnitudes from the two inversions are slightly different ( $M_w$  6.3 for seismic;  $M_w$  6.34 for geodetic). The difference of the two predicted moments is equivalent to a  $M_w$  5.7 earthquake. We note that the geodetic inversion shows more slip near the largest ( $M_w$  5.0) aftershock (Figure 2.31b), which suggests that the difference may in part be due to deformation from the early aftershocks spanned by the geodetic data. Consideration of both seismic and geodetic inversions can provide information about the main shock and the early aftershocks.

Further work will focus on additional improvements of the seismic inversion and the aftershocks analysis. For example, the seismic inversion does not fit the directivity in station CHY089 well (Figure 2.31a), which might be due to an over-simplified fault geometry or improper Green's functions. With these improvements, we will aim to better understand the kinematic process of this event and its tectonic framework in west Taiwan.

## 15.4 Acknowledgements

We thank the Institute of Earthscience, Academia Sinica, Taiwan for providing seismic and geodetic data. We thank H.-H. Huang of National Taiwan University for providing the aftershock catalog.

## 15.5 References

- Chi, W.-C. and Dreger, D., Finite fault inversion of the September 25, 1999 ( $M_w = 6.4$ ) Taiwan earthquake: Implications for GPS displacements of Chi-Chi, Taiwan earthquake sequence, *Geophys. Res. Lett.*, 29, doi:10.1029/2002GL015237, 2002.
- Hartzell, S. H., and T. H. Heaton, Inversion of strong ground motion and teleseismic waveform data for the fault rupture history of the 1979 Imperial Valley, California, earthquake, *Bull. Seismol. Soc. Am.*, 73, 1553-1583, 1983.
- Kaverina, A., Dreger, D., and Price, E., The combined inversion of seismic and geodetic data for the source process of the 16 October 1999  $M_w$  7.1 Hector Mine, California earthquake, *Bull. Seismol. Soc. Am.*, 92, 1266-1280, 2002.

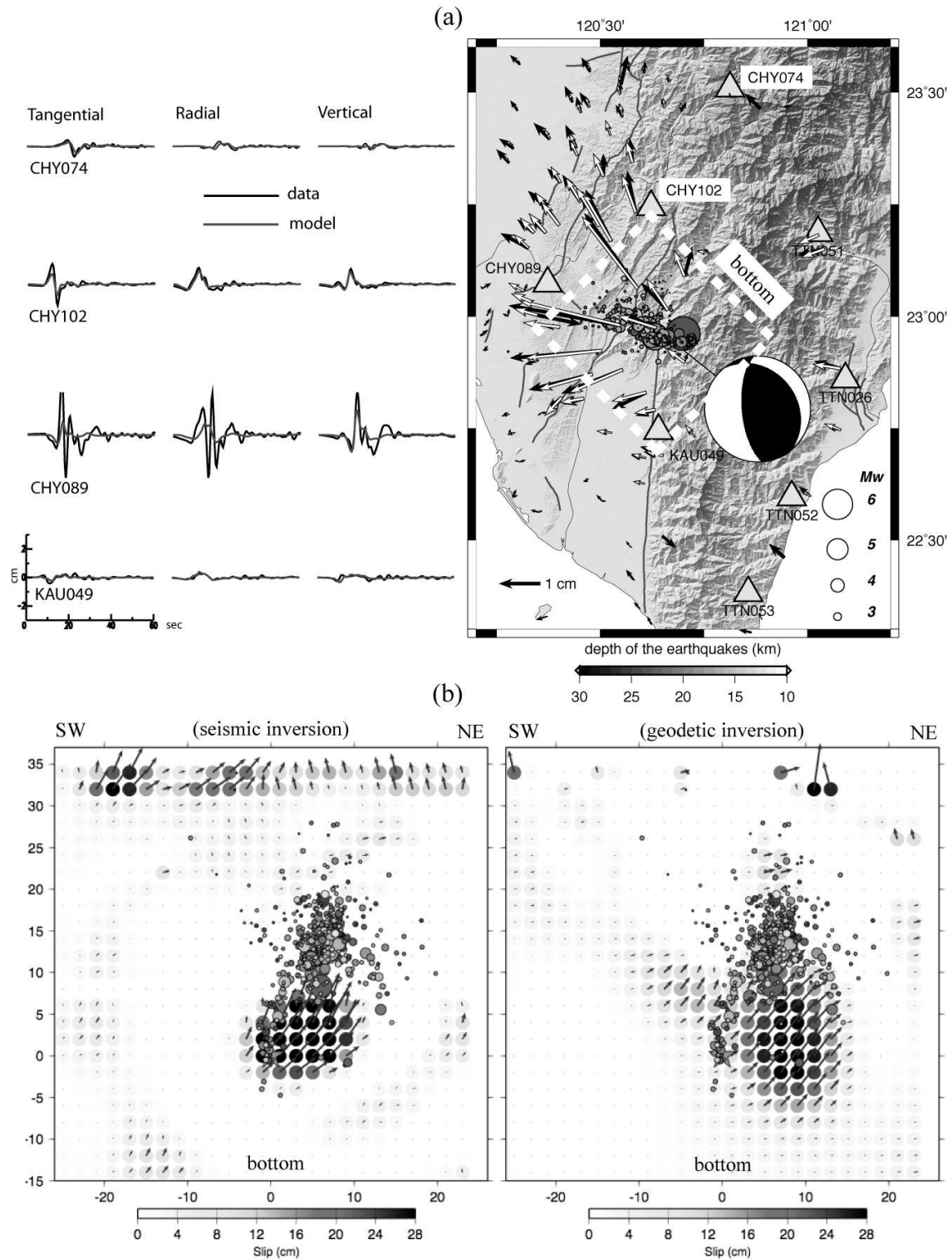


Figure 2.31: (a) Right: The study area and the comparison of the GPS data (black arrows) and model prediction (white arrows) using the finite source inversion. The circles are the aftershocks for the first 24 hours. The triangles show the locations of the seismic station. The white dashed rectangle shows the fault geometry. Left: The comparison of the strong motion seismic data (black) and the predicted models (gray) using the finite source inversion. Note that the larger amplitude of station CHY089 is due to the directivity of this event. (b) The comparison of the coseismic fault slip based on seismic (left) and geodetic (right) inversions. The arrows indicate the slip orientation of each subfault. The circles show the distribution of the aftershocks.

## 16 Tidal Triggering of LFEs near Parkfield, CA

Amanda M. Thomas, Roland Bürgmann, David Shelly, Nick Beeler, and Maxwell Rudolph

### 16.1 Introduction

We study the influence of the ocean and solid earth tides on low frequency earthquakes in Parkfield, CA. Several spatially localized families at  $\sim 25$  km depth seem to fail preferentially when the tides are inducing negative fault-normal stress, or clamping, inconsistent with conventional models of fault strength. The hypocenters of these earthquake families are spatially coincident with a right-stepping bend in the San Andreas Fault near Gold Hill. This observation argues that deformation can remain localized well below the brittle-ductile transition. High pore-fluid pressures provide a potential mechanism for maintaining localized, brittle deformation deep in the crust.

### 16.2 Data

The 2001- January 2010 low-frequency earthquake catalog of (*Shelly and Hardebeck, 2010*) is composed of  $\sim 550,000$  Low Frequency Earthquakes (LFEs) grouped into 88 different families based on waveform similarity. Locations of LFE families in Parkfield are tightly constrained by numerous P- and S-wave arrival times at densely distributed stations. The location procedure involves visually identifying individual LFE template event candidates and then cross-correlating and stacking those waveforms with continuous seismic data to detect other LFEs in the same family. The most similar events are stacked at all regional stations, and P- and S-wave arrivals are identified on these stacked waveforms. LFEs are located by minimizing travel time residuals in a 3D velocity model of the Parkfield area (for further details see *Shelly and Hardebeck, 2010*). Hypocenters of LFE families, shown in Figure 2.32, are distributed along  $\sim 150$  km of the San Andreas Fault, from Bitterwater to south of Cholame. Estimated source depths extend from just below the base of the seismogenic zone to the Moho (16-30 km depth) on the deep extension of the San Andreas Fault, a zone previously thought incapable of radiating seismic waves.

### 16.3 Methods

We compute tidally-induced strains at the centroid of the tremor source region (-120.525, 35.935, 25 km depth) using the tidal loading package Some Programs for Ocean Tide Loading (*Agnew, 1996*), which includes both solid earth and ocean tidal loading. Displacements from the solid earth tide are very long wavelength compared to the source region depth; thus we assume that the strains

modeled at the surface are not significantly different from those at 25km depth. At the surface in Parkfield, the ocean loading component is small compared to the solid earth tides; however, the magnitude of the ocean loading component should increase with depth, potentially impacting the validity of the strains computed at the surface. To resolve this potential issue, we calculate depth dependent, spherical Green's functions which are used to compute the strains from only the ocean loading component at depth. The dimension of the LFE source region is small with respect to the degree two pattern of the tides, but to validate the assumption that tidal stress changes are small over the  $\sim 140$  km section of the San Andreas Fault under consideration, we computed and compared strain timeseries at the center and end of the LFE source region and found that the difference was insignificant.

Assuming 2D plane strain (no depth dependence) in a homogenous medium, we convert strain to stress using a linear elastic constitutive equation. Stresses are then resolved onto the San Andreas Fault assuming a strike of  $N42^\circ W$ , parallel to the San Andreas Fault. The vast majority of the stress amplitudes are due to only the body tides, as the ocean loading contribution diminishes with distance inland. Also, the body tides induce largely volumetric stresses in the earth's lithosphere: thus the resulting shear stress on the SAF fault due to the tides is approximately an order of magnitude smaller than the normal stress.

### 16.4 Results

One spatially localized group of LFE families that exhibit statistically significant correlation with compression, or negative fault-normal stress (FNS), warrants further discussion. A simplified Coulomb friction model cannot explain preferential triggering during times of compression, as Coulomb failure stress depends positively on fault normal stress, meaning that earthquakes should preferentially trigger during times of extension and not clamping. However, appealing to a more complicated model seems unnecessary, as the remaining families have either insignificant, or positive significant correlations with the FNS and right-lateral shear stress (RLSS).

The mapped surface trace of the San Andreas Fault has a small releasing bend, in the Gold Hill region between Parkfield and Cholame where the fault orientation oscillates between  $N43^\circ W$  and  $N30^\circ W$  degrees west of north in a distance of  $\sim 10$  km. While the 88 hypocentral locations are too sparse to map fault geometry to depth over the 160 km section of the SAF, the majority

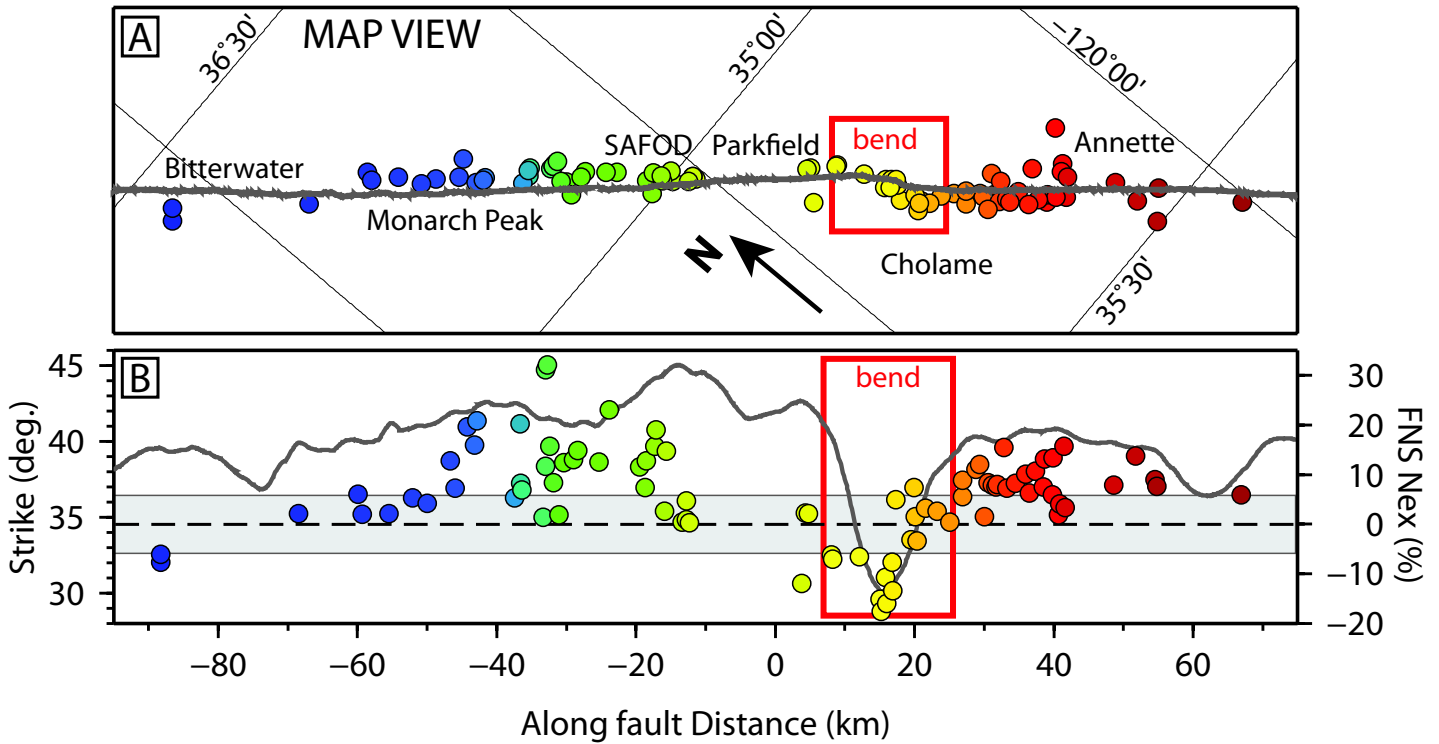


Figure 2.32: (a) A rotated map view of LFE locations color coded by family ID number as in figure 2. The stepover region is outlined in red to highlight the common morphology of the surface fault strike and the LFE hypocentral locations at depth. (b) The mapped fault strike, dark grey solid line, in degrees west of north (left axis) derived from the strike in Panel A as a function of distance along the fault. Colored circles correspond to families in Panel A. Their vertical position, measured relative to the right axis, is their FNS Nex value. Dark grey dashed line marks the zero FNS Nex value with 99% confidence intervals indicated in light grey. The stepover region is marked in red and correlates well with the negative FNS Nex values.

of locations seem to lie on one coherent fault strand with very few events deviating substantially from the mapped trace. This observation suggests that while some small amount of the total slip budget is accounted for off-fault, tremor-producing deformation largely remains localized at depths up to 25 km, and if hypocenters are closely spaced, their geometry may reflect the geometry of the San Andreas Fault at depth. If the majority of LFE hypocenters are on fault, the similar morphology of both the LFE hypocentral locations and the mapped fault trace within the fault-bend region suggests that roughness on length scales of ten kilometers is preserved at depth.

Panel B in Figure 2.32 compares the local fault orientation derived from the mapped surface trace of the San Andreas Fault to the observed FNS Nex values. The most striking feature of this comparison is that nearly all families within the fault bend have either insignificant or negative values of FNS Nex values, suggesting that fault geometry may be responsible for the mechanically implausible correlation with clamping. While changing the fault azimuth to account for local geometry in a 2D

plane strain model does not produce positive, or insignificant Nex values, variable fault strike is still a reasonable explanation for the anomalous Nex values, as the model may not be sufficiently complicated to adequately characterize the magnitude of stresses resulting from such a geometry.

## 16.5 Acknowledgements

This work is funded by the United States Geological Survey and a National Science Foundation Graduate Research Fellowship.

## 16.6 References

- Agnew, D.C., SPOTL: Some programs for ocean-tide loading, *SIO Ref. Ser.*, 96-8, 35 pp., Scripps Institution of Oceanography, La Jolla, CA, 1996.
- Shelly, D.R. and J.L. Hardebeck, Precise tremor source locations and amplitude variations along the lower-crustal central San Andreas Fault, *Geophys. Res. Lett.*, 37, L14301, 2010.
- Thomas, A.M., R.M. Nadeau, and R. Bürgmann, Tremor-tide correlations and near-lithostatic pore pressure on the deep San Andreas fault, *Nature*, 462, 1048-1051, 2009.

# 17 TremorScope: Imaging the Deep Workings of the San Andreas Fault

Roland Bürgmann, Richard Allen, Pascal Audet, Douglas Dreger, Robert Nadeau, Barbara Romanowicz, Taka'aki Taira, Margaret Hellweg

## 17.1 Introduction

Until recently, active fault zones were thought to deform via seismic earthquake slip in the upper, brittle section of the crust, and by steady, aseismic shear below. However, in the last few years, this view has been shaken by seismological observations of seismic tremor deep in the roots of active fault zones. First recognized on subduction zones in Japan and the Pacific Northwest, tremor has also been found to be very active on a short section of the San Andreas to the southeast of one of the most densely monitored fault segments in the world, near Parkfield (*Nadeau and Dolenc, 2005*). This deep (20-30 km) zone of activity is located right below the nucleation zone of the great 1857 Fort Tejon earthquake. Thus, understanding the temporally and spatially complex faulting process in this zone may help us better understand the conditions that lead to such large ruptures.

## 17.2 The Project Plan

Although the tremor source region is away from existing seismic networks in and around Parkfield, early studies of the deep tremor have led to dramatic revisions in our views about how faults behave at depth (e.g., *Nadeau and Guilhem, 2009; Thomas, Nadeau and Bürgmann, 2009; Shelly, 2010; Shelly and Hardebeck, 2010*). These studies reveal behavior of faulting in the deep crust that is complex and dramatically different from the “normal” earthquakes that occur in the shallow crust. By adding seismic stations around the tremor source zone, we will complement the existing monitoring around Parkfield. The result, the TremorScope network, will sharpen our ability to explore this fascinating natural laboratory of active lower crustal faulting.

The proposed network consists of eight new stations to be centered on the tremor source (Figure 2.33). Four sites will have borehole installations and an accelerometer at the surface. The target is to install the equipment in boreholes that are 300 m deep. Each hole will have a three-component set of gimballed, 2 Hz geophones cemented at the bottom that will be digitized at the surface. In three boreholes, a Guralp downhole sensor package, consisting of a three-component broadband seismometer, a three-component accelerometer and a digitizer, will also be deployed. The other four stations will be surface installations consisting of a broadband seismometer, an accelerometer and a digitizer. At all locations, data will be logged onsite and forwarded to Berkeley for real-time processing. The data will be used in real-time earthquake monitoring (see Operations Sec-

tion 8), as well as for tremor studies. The borehole sites (CASS, SCN, NC.PBP and NC.PPG) will be at some distance from the tremor source centroid, to offer low-noise, high quality recordings that offer good constraints on the tremor locations and depth. The four surface stations, closer to the tremor centroid, will have broadband seismometers, accelerometers and digitizers, as well as data loggers.

The project began in January 2011. We have ordered equipment and found sites for the stations (Figure 2.33). During the summer, we will be performing telemetry tests. We expect to install the stations in the fall of 2011.

## 17.3 Perspectives

Data from the TremorScope project will improve earthquake monitoring in the region south of Parkfield. Insights from the project will also contribute to understanding tremor and slip in other regions of the world where such phenomena have been observed, but are not nearly as accessible. Should a great San Andreas earthquake occur during this experiment, the network would also provide unprecedented and exciting insights into the seismic rupture process.

## 17.4 Acknowledgements

This work is funded by grant 2754 from the Gordon and Betty Moore Foundation.

## 17.5 References

- Nadeau, R., and D. Dolenc (2005), Nonvolcanic tremors deep beneath the San Andreas fault, *Science*, 307, 389, doi:10.1126/science.1107142.
- Nadeau, R.M. and A. Guilhem (2009), Nonvolcanic Tremor and the 2003 San Simeon and 2004 Parkfield, California Earthquakes, *Science*, 325, 191-193.
- Shelly, D. R., and J. L. Hardebeck (2010), Precise tremor source locations and amplitude variations along the lower-crustal central San Andreas Fault, *Geophys. Res. Lett.*, doi:10.1029/2010GL043672.
- Shelly, D. R. (2010), Migrating tremors illuminate deformation beneath the seismogenic San Andreas fault, *Nature*, 463, 648-652. doi:10.1038/nature0875.
- Thomas, A., R. M. Nadeau, and R. Bürgmann (2009), Tremor-tide correlations and near-lithostatic pore pressure on the deep San Andreas fault, *Nature*, 462, 24-31.

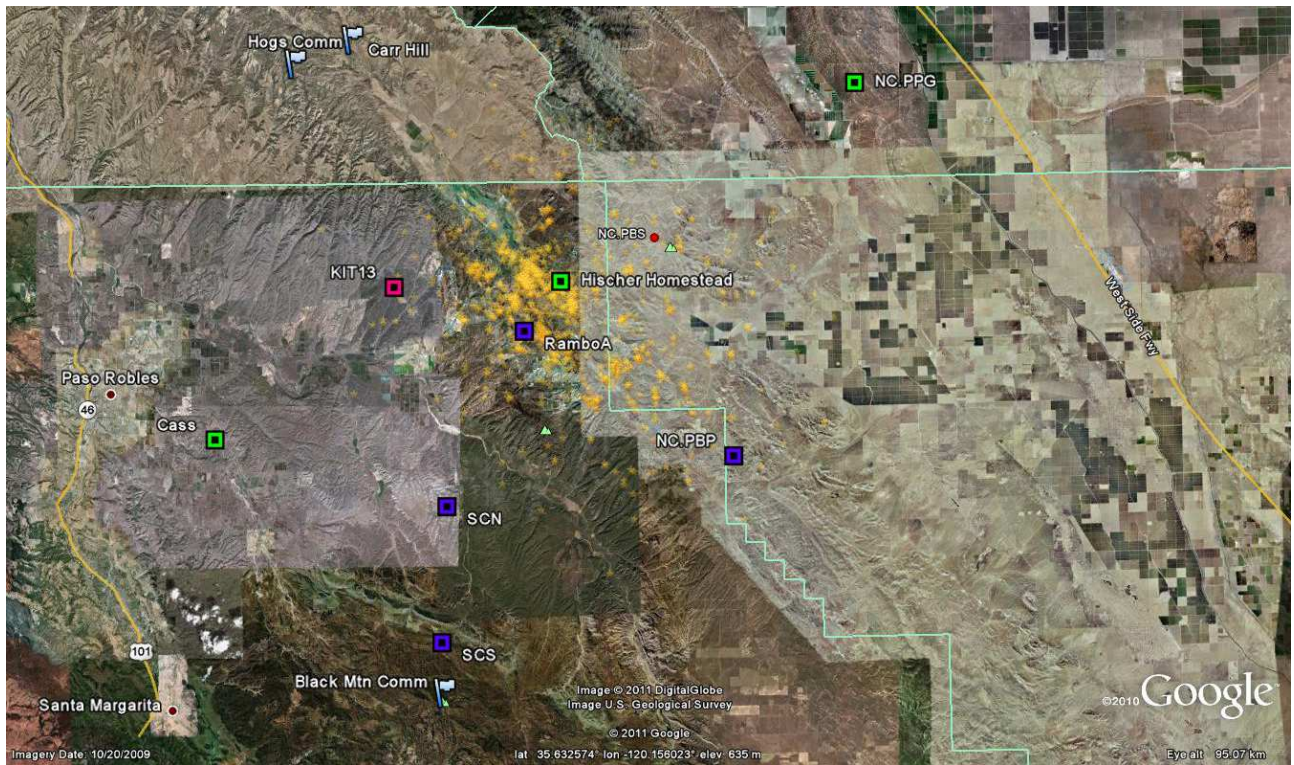


Figure 2.33: Planned locations for TremorScope stations. Gold stars: Tremor locations. Colored squares: TremorScope sites. NC.PBP and NC.PPG are currently operated by the USGS Menlo Park and have short period vertical geophones and analog telemetry. Sites Cass, SCS, NC.PBP and NC.PPG will be borehole stations. SCN and SCS are collocated with PBO GPS stations. Telemetry will go via radio to Carr Hill, Hogs Canyon Comm. or Black Mountain Comm.

# 18 Search for Transient Deformation Following an Earthquake Sequence near San Juan Bautista

Ingrid A. Johanson

## 18.1 Introduction

The San Juan Bautista segment of the San Andreas fault has a history of producing slow earthquakes of about the same size as its largest recorded seismic events. The largest of these is a slow earthquake that followed a  $M_w$  5.1 seismic event in 1998 and itself had a moment of  $M_w$  5.0 (Gwyther *et al.*, 2000). At the time, BARD station SAOB was the only continuous GPS station in the region, and it showed a  $\sim 5$  mm displacement due to the slow earthquake (Uhrhammer *et al.*, 1999). However, since completion of PBO installation, there are several more GPS stations and strainmeters that also would be capable of detecting a 1998-like slow slip event (Figure 2.34).

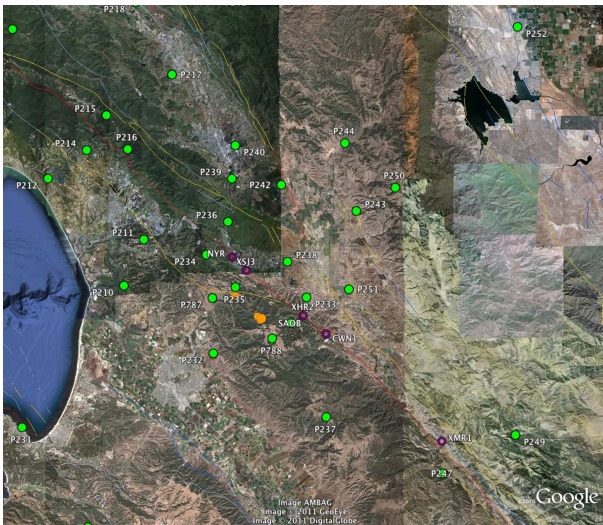


Figure 2.34: Location map of San Juan Bautista segment of the San Andreas fault. Purple circles are USGS and Univ. Colorado, Boulder creepmeters; green circles are PBO and BARD continuous GPS stations. Orange circles are the locations of M3 and higher earthquakes in January, 2011, which are assumed to have occurred on a southwest dipping San Andreas fault.

A recent series of earthquakes (Jan. 12-13, 2011) on the San Juan Bautista segment was followed several days later by a moderate creep event (Figure 2.35). We looked closely at the nearby continuous GPS data to determine how far the effect of the event could be detected and thereby constrain the extent of the possible slow earthquake. However, there was no clear evidence of transient deformation at any of the GPS stations in the area.

Possible deformation signals would appear to be either isolated to a single station (i.e. inconsistent with other stations) or part of repeating seasonal deformation.

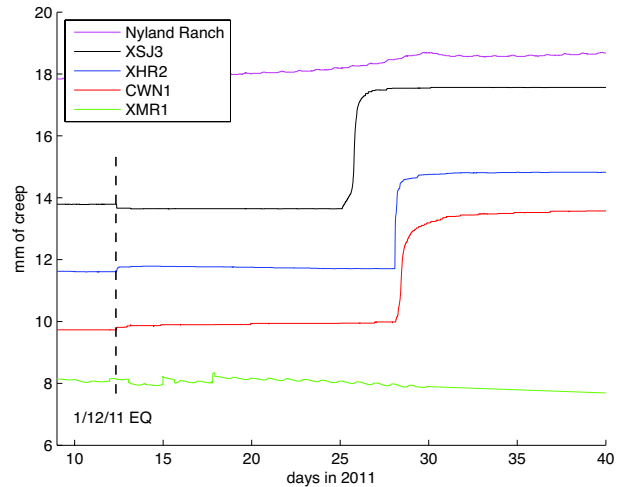


Figure 2.35: Creepmeter records from 1/9/2011 - 2/9/2011 for one U. Colorado (NYR) and four USGS creepmeters on the San Andreas fault. A small offset is seen at the time of the earthquake, likely due to shaking of the instrument during the event, rather than fault slip. A creep event occurs at SAOB 13 days after the M4.1 earthquake; after 4 more days, a creep event occurs at XHR2 and CWN1.

## 18.2 GPS Results

Figure 2.36 shows time series of baseline changes for two fault-crossing lines. P233 to SAOB seems to contain transient deformation following the January earthquakes; however baseline P233 to P788 does not have a similar pattern. P788 is further away from the San Andreas fault than SAOB, so the lack of transient deformation could imply that the slow slip event is very shallow. If this were the case, then there should still be some contribution from motion of P233, which is a similar distance from the fault as SAOB. The complete lack of post-earthquake motion in the P233 to P788 baseline suggests that the pattern observed in the P233 to SAOB time series is due to fortuitously shaped noise.

In fact, on a larger scale, the pattern in Figure 2.36A is minor in comparison to a larger decrease in the East component of the P233-SAOB baseline at the end of 2010

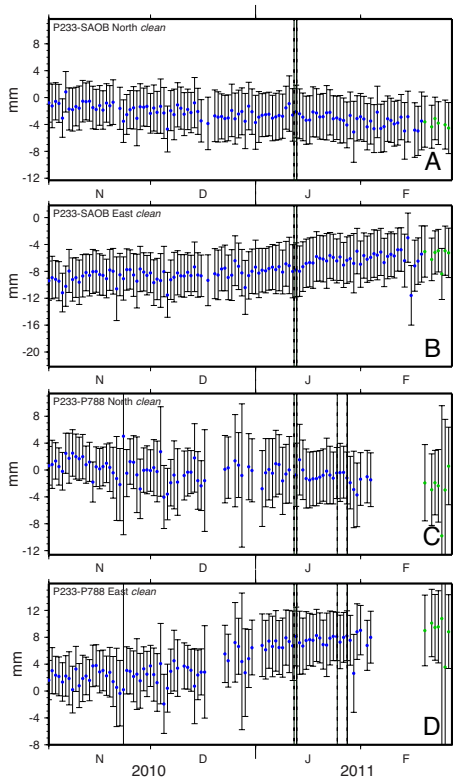


Figure 2.36: Time series of position differences for sites P233 to SAOB (A: North B: East) and sites P233 to P788 (C: North D: East). Both are fault-crossing baselines near the location of the 1/12/11 earthquake. Green points are those processed with IGS Rapid orbit files rather than Final orbits (black points). First set of black lines are the times of the two largest EQs in the SJB sequence; the second set is the creep events at XSJ3 and XHR2/CWN1.

(Figure 2.37B). This decrease and then resumption of eastward motion is also apparent in the P251 to P232 baseline, which also crosses the San Andreas fault, but has a longer distance. This suggests that the apparent motion is due to a regional process. However, from a multi-year time series, it is apparent that such a change in eastward motion occurs every year in the wintertime (Figure 2.37C). So while the motion may be consistent across several stations, it seems likely due to regional rainfall, rather than a slow slip event.

### 18.3 Acknowledgements

This work was supported by NSF-EarthScope Grant #EAR-0951430.

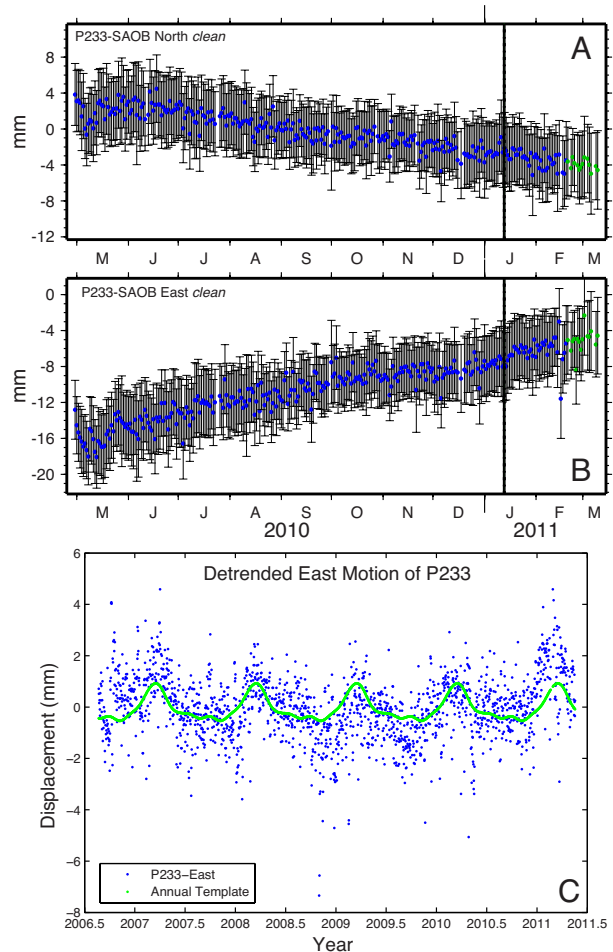


Figure 2.37: Time series of position differences for sites P233 to SAOB (A: North B: East) and C) detrended eastward motion of site P233 relative to stable North America, processed by PBO (<http://pboweb.unavco.org/shared/scripts/stations>).

### 18.4 References

Gwyther, R. L., C. H. Thurber, M. T. Gladwin, and M. Mee, Seismic and aseismic observations of the 12th August 1998 San Juan Bautista, California M5.3 earthquake, paper presented at *3rd San Andreas Fault Conference*, Stanford Univ., Stanford, Calif., 2000.

Uhrhammer, R., L. S. Gee, M. Murray, D. Dreger, and B. Romanowicz, The  $M_w$  5.1 San Juan Bautista, California earthquake of 12 August 1998, *Seismol. Res. Lett.*, 70, 10-18, 1999.

# 19 Probing the Deep Rheology of Tibet: Constraints from 2008 $M_w$ 7.9 Wenchuan, China Earthquake

Mong-Han Huang and Roland Bürgmann

## 19.1 Introduction

The 2008  $M_w$  7.9 earthquake occurred at Wenchuan of Sichuan Province, China, and studies of the earthquake and its postseismic relaxation give us an opportunity to examine the rheology of east Tibet. The surface motion after a large earthquake is a response to the redistribution of stresses induced by the earthquake and can be used to probe the viscous strength of the upper lithosphere. Various processes can contribute to the postseismic deformation, such as aseismic afterslip, aftershock related deformation, viscoelastic relaxation in the lower crust/upper mantle, and poroelastic rebound. In this study, we consider the viscous relaxation due to the coseismic stress redistribution that would primarily affect the middle- to far-field surface deformation.

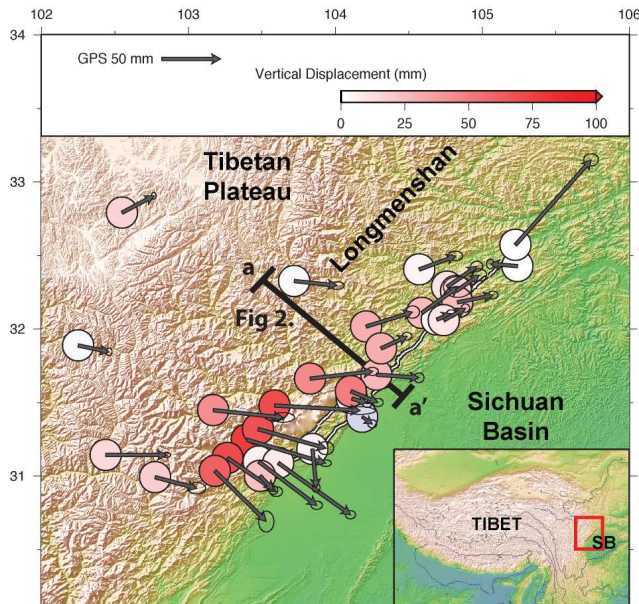


Figure 2.38: Wenchuan postseismic deformation from GPS. The arrows show horizontal motions, and colored circles are the vertical displacement (the scale is shown above). The inset shows the topographic contrasts between Tibet and the Sichuan basin (SB).

## 19.2 Method and Data

We apply an analytical solution (Pollitz, 1992) to calculate postseismic deformation due to viscoelastic relaxation of a layered spherical Earth, and include the effects of gravity and medium compressibility. Each layer can be represented with elastic or viscoelastic (Maxwell

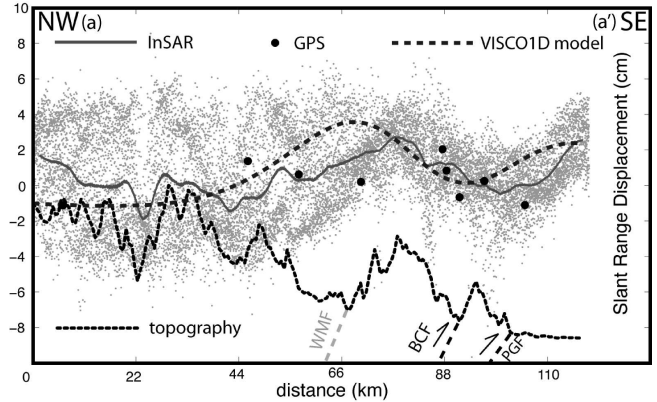


Figure 2.39: The slant range displacement along the profile in Figure 2.38. The mean SRD is the average of the dots representing extracted data from InSAR pair 2008/07/21-2009/09/08. The predicted model shows agreement with InSAR and GPS (projected to line of sight).

and Burgers) properties. In this study, the density, bulk modulus, and rigidity of each layer are based on the CRUST 2.0 model (<http://igppweb.ucsd.edu/~gabi/crust2.html>). The Wenchuan earthquake fault geometry is based on Shen et al., 2009, based on geodetic inversion of coseismic deformation. Our simplified fault geometry is composed of five segments with different slip rates, extends to a depth of 20 km, and runs along the 285 km Longmenshan fault zone oriented  $229^\circ$  (Figure 2.38).

Thirty one cGPS stations are deployed in eastern Tibet in the hanging wall of the Longmenshan fault zone. To obtain the first-year postseismic deformation, we fit the cGPS time series in terms of a linear least square fit with the assumption of zero displacement right after the main shock (Figure 2.39). We used more than 30 ALOS PALSAR L band (23.6 cm wavelength) data sets from May 2008 to October 2010 to measure the postseismic deformation. The ALOS PALSAR data from six paths (471-476) and seven frames (590-640) cover most of the Wenchuan postseismic deformation. All PALSAR data are processed using the software ROI PAC 3.0, and the 90 m SRTM DEM is used to correct the phase due to topography.

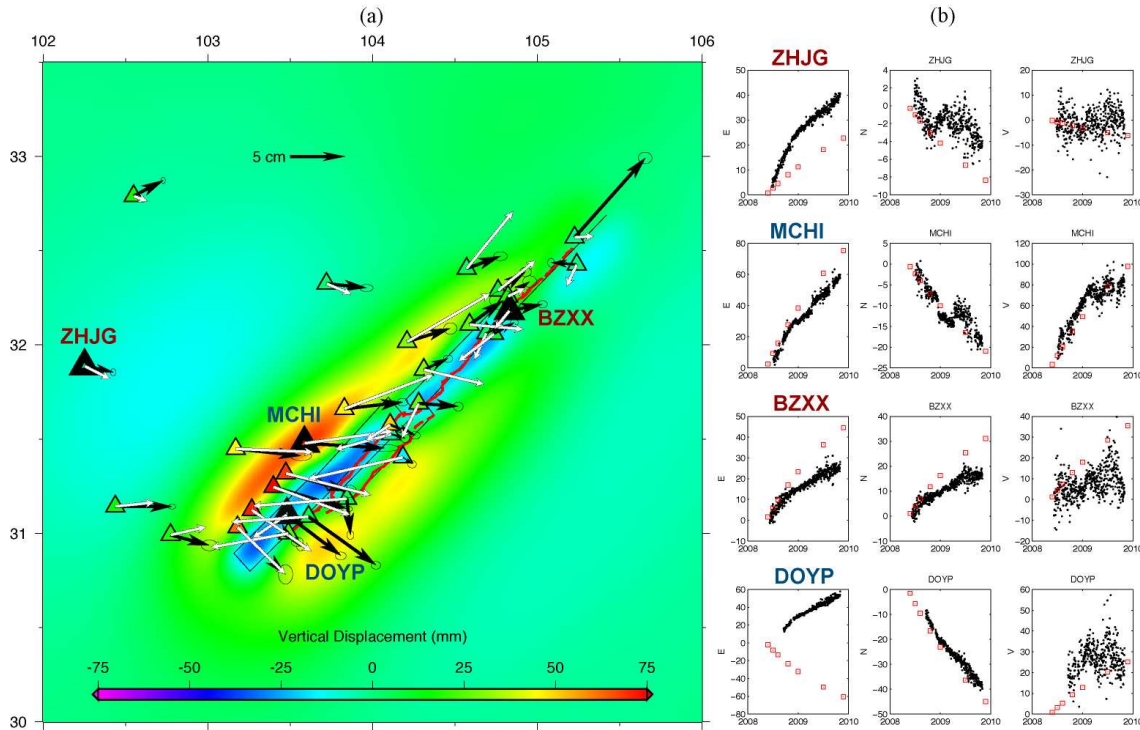


Figure 2.40: (a) The comparison of GPS and the forward model. The five fault planes that represent the Wenchuan coseismic fault geometry are shown by blue rectangles. The black arrows are the GPS horizontal measurements, and the white arrows are the model. The color in the triangles is the GPS vertical displacement, and the background color is the model uplift. (b) The cGPS time series. The black dots are the GPS and the red squares are the model.

### 19.3 Results

All cGPS time series data show transient displacements in the horizontal and vertical components. The 1.5-year observations (Figure 2.38) show southeastward displacement in the SW and northeastward displacement in the NE Longmenshan. Most of the interferograms have strong topographic and ionospheric correlated noise and low coherence in the mountains. The mean slant range displacement (SRD) of one 2.5-year interferogram of track 474 (Figure 2.39) shows postseismic deformation comparable with the cGPS measurements.

The best fitting forward model suggests that a Burgers body based lower crust with a steady-state viscosity of  $10^{19}$  Pa s and a transient viscosity of  $4 \times 10^{18}$  Pa s, with a 20 km elastic upper crust, can represent the rheology of Longmenshan. Figures 2.39 and 2.40 show the predicted viscoelastic relaxation and the comparison with the InSAR and cGPS data, respectively. Figure 2.40b shows the temporal fitting of 4 out of 31 cGPS stations representing far-field, middle-field, and near-field deformation, respectively. The prediction is generally of the same scale as the data and better fits the middle- to far-field data. The poor fit to the near field might be because of the lateral heterogeneity in the boundary of the plateau and the basin, which is not considered in our 1D model. Neither afterslip nor poroelastic deformation, either of which

could control the near-field postseismic deformation, are considered here.

Future work will focus on a reliable 3D rheological structure of eastern Tibet and the consideration of other processes such as afterslip and poroelastic deformation. Additional ENVISAT InSAR data will be considered in order to obtain the deformation in time series following the Wenchuan mainshock.

### 19.4 Acknowledgements

We thank prof. Z.-K. Shen of Beijing for providing the GPS time series. This work is supported by NSF grant EAR 0738298.

### 19.5 References

Pollitz, F., Postseismic relaxation theory on a spherical earth. *Bull. Seism. Soc. Am.*, 82, 1, 422-453, 1992.  
 Shen, Z.K., J. Sun, P. Zhang, Y. Wan, M. Wang, R. Bürgmann, Y. Zeng, W. Gan, H. Hiao, and Q. Wang, Slip maxima at fault junctions and rupturing of barriers during the 2008 Wenchuan earthquake, *Nat. Geosci.*, 2, 718-724, doi:10.1038/NCEO636, 2009.

# 20 Joint Seismic and Geodetic Analysis of the 2009 Padang, Sumatra Intraslab Earthquake

Kelly Wiseman, Roland Bürgmann, Doug Dreger, Paramesh Banerjee (EOS, Singapore) and Kerry Sieh (EOS, Singapore)

## 20.1 Introduction

The  $M_w$  7.6 Padang earthquake occurred on 30 September 2009 offshore of central Sumatra (Figure 2.42). Seismicity in the Sumatra region is driven by the oblique subduction of the Indian and Australian plates beneath the Burma forearc block and Sunda plate at the Sunda trench. The Sunda megathrust has been extremely active ever since the 2004  $M_w$  9.2 Sumatra-Andaman earthquake, with additional megathrust earthquakes in 2005, 2007, and 2010. The last remaining section of the Sunda megathrust without a modern great earthquake is the Siberut segment, which lies offshore of Padang. Thus, it is especially important to understand the fault mechanism of the 2009 Padang earthquake in order to assess how it affects the stress levels on the Siberut segment of the megathrust.

The Padang earthquake is an unusual event because it likely ruptured the subducting Australian plate. The Engdahl relocated earthquake catalog locates the earthquake at 78 km depth,  $\sim$ 250 km from the Sunda trench, where the Hayes *et al.* (2009) Sunda slab model places the interface at  $\sim$ 69 km depth. The Padang earthquake rupture mechanism is also consistent with an intraslab event. The strike is approximately perpendicular to the trench with significant left-lateral strike-slip motion. Possible candidates for the rupture plane could be subducted paleo transform faults, fractures, or ridges. We attempt to resolve the fault plane using regional broadband seismic data, GPS data, and aftershock locations.

## 20.2 Data and Processing

There are 7 three-component broadband stations located within 750 km of the epicenter, with useable data available on IRIS, operated by the GEOFON network, the Malaysian National Seismic Network, and the Singapore National Network. For our finite fault inversions, both the displacement waveform data and the Greens functions are bandpass filtered between 0.01 to 0.3 Hz. The maximum waveform amplitude for each component varies from about 0.5 to 1.5 cm at this frequency range. We also include data from 18 three-component permanent GPS stations, located within 380 km of the epicenter, from the SuGAR and ENS-INSU regional networks (Figure 2.42).

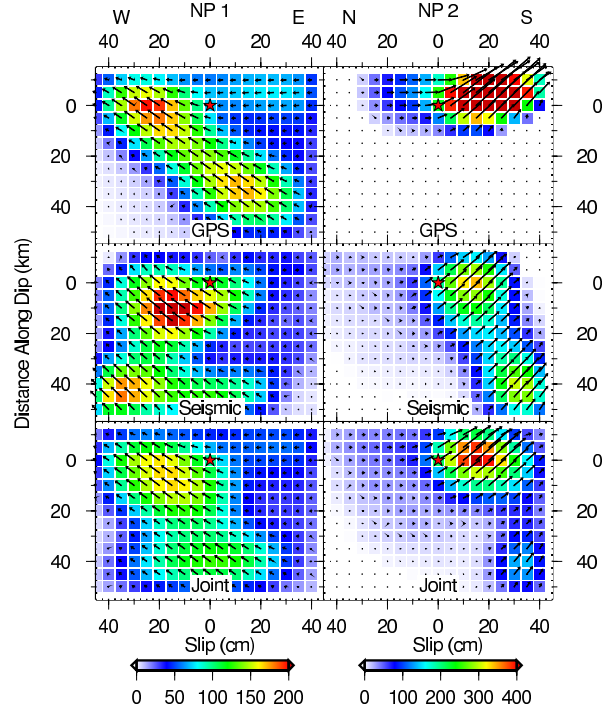


Figure 2.41: Left: Slip models for the east-west nodal plane using GPS, seismic, and joint data. Right: Slip models for the north-south nodal plane. The hypocenter is marked with a star and the arrows indicate the variable inverted rake direction.

## 20.3 Inversion Method

The Green's functions for our finite fault inversions are calculated using a 1D frequency-wavenumber integration method (Saikia, 1994). Our starting earth model consists of the Lange *et al.* (2010) velocity structure, PREM densities, and typical crustal attenuation values. To invert for finite fault slip, we use a least-squares inversion method that employs simultaneous smoothing and dampening (e.g. Kaverina *et al.*, 2002). We initially invert the GPS data for fault geometry, using a uniform slip model. Nodal plane (NP) 1 has a strike of  $80^\circ$  and dip of  $57^\circ$ , and NP2 has a strike of  $190^\circ$  and dip of  $60^\circ$ . Our optimal strike and dip values are very similar to the GCMT moment tensor solution geometry, and we allow variable rake in the finite fault inversions. Our fault plane extends 100 km along strike by 75 km downdip, divided into  $5 \times 5$  km patches. The hypocenter is located in the central

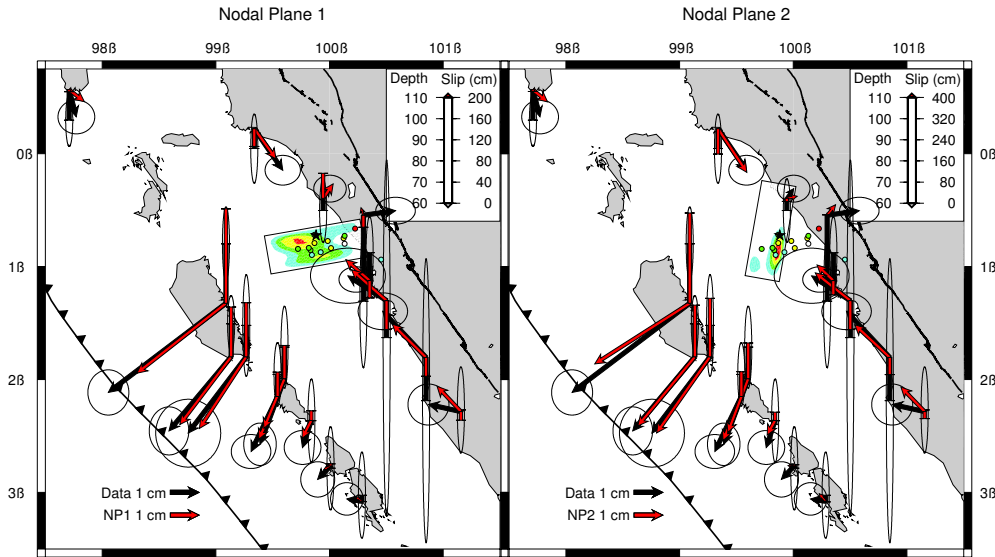


Figure 2.42: Map view of the joint inversion slip distributions (shown in Figure 2.41) with overlain GPS observation and model vectors.

position along strike and 3 patches downdip to prevent slip from propagating through the plate interface.

## 20.4 Inversion Results

The initial seismic finite fault inversion for both nodal plane geometries does a fairly good job of fitting the waveform amplitudes and polarities. However, all of the synthetics have significant phase shifts on the order of 10 seconds that cause the variance reductions to be negative. The highest variance reductions for each NP geometry are achieved using the Lange model with a uniform 10% increase in velocities across all depths. NP1 has a variance reduction (VR) of 56% and NP2 has a VR of 54%. For both inversions, there are two high slip regions, one near the hypocenter and the other  $\sim 40$  km downdip (Figure 2.41).

The NP1 GPS-only inversion also has two high slip regions, although the deeper slip extends further east than the seismic-only inversion and has a VR of 79%. The NP2 GPS-only inversion has one focused high slip region, south of the hypocenter, with a VR of 80%. The NP2 model has higher peak slip values than the NP1 model, but the total moment is  $\sim 20\%$  lower.

The joint inversions both have one high slip region. The east-west NP1 slip distribution is broader and extends 45 km downdip of the hypocenter, with a 40 x 55 km high slip region. The north-south NP2 slip distribution has a more focused depth range, and the high-slip region is constrained to 40 x 25 km. The seismic and GPS data are very compatible, and the joint variance reductions are within 95% of their individual inversion values.

## 20.5 Discussion

Our joint inversions of the Padang earthquake, using both regional seismic waveform and geodetic data, have shown that the two nodal planes have equivalent variance reductions and the total moment differs by only  $\sim 10\%$ , equal to  $M_w$  7.7 events. The north-south plane has a more focused slip distribution than the east-west plane. However, the NEIC aftershock sequence better aligns with the strike and depth range of the east-west plane (Figure 2.42). Therefore our preferred fault model is slip on the east-west nodal plane, primarily southwest of the hypocenter.

## 20.6 Acknowledgments

This work is supported by the National Science Foundation grant EAR 0738299.

## 20.7 References

- Hayes et al., Advancing techniques to constrain the geometry of the seismic rupture plane on subduction interfaces a priori: Higher-order functional fits, *Geochem. Geophys. Geosys.*, 10, 10.1029/2009GC002633, 2009.
- Kaverina et al., The combined inversion of seismic and geodetic data for the source process of the 16 October 1999  $M_w$  7.1 Hecator Mine, California, earthquake, *Bull. Seis. Soc. Am.*, 92, 1266-1280, 2002.
- Lange et al., The fine structure of the subducted investigator fracture zone in Western Sumatra as seen by local seismicity, *EPSL*, 298, 47-56, 2010.
- Saikia et al., Modified frequency-wave number algorithm for regional seismograms using Filon's quadrature-modeling of L(g) waves in eastern North America, *Geophys. J. Int.*, 118, 142-158, 1994.

# 21 Rapid Detection of Large Earthquakes Using Quasi-Finite-Source Green's Functions in Moment Tensor Analysis

Aurelie Guilhem and Douglas S. Dreger

## 21.1 Introduction

Rapid procedures (i.e. within 5 to 15 minutes) for earthquake and tsunami early warnings focus on earthquake location, depth, magnitude, and slowness, but initial tsunami early warnings are more often issued without knowing the mechanism of the earthquake. *Kawakatsu* (1998) proposed using a limited number of stations to automatically detect, locate and determine the source parameters of earthquakes occurring within a predefined region by computing moment tensors at each point of a grid from continuously streaming long-period waveform data. This method gives correct results in terms of detection and source characterization of up to M7 earthquakes offshore Japan (*Tsuruoka et al.*, 2009). For major earthquakes (M8+), we propose to improve the point-source moment tensor inversion by using QFS Green's functions (QFS GFs) that takes into account the finiteness of the rupture zone. Using a direct and single-step procedure, it becomes possible to monitor all  $M_w > 3.5$  earthquakes.

## 21.2 Method

*Kawakatsu* (1998) proposed to continuously invert the long period seismic wavefield ( $> 10$  sec) for moment tensors at grid points representing virtual sources distributed over a region. At each station, the data  $d$  are represented as the convolution of the GF tensor,  $G$ , describing the wave propagation between the source and the receiver, and the moment tensor components  $m$  of the source:

$$d = G \cdot m$$

The least-square solution for the moment tensor can be obtained:

$$M = (G^T G)^{-1} G^T d$$

where the  $(G^T G)^{-1} G^T$  matrix for each point-source can be computed in advance. The multiplication of this matrix with streaming data can be performed continuously. Earthquake detection is given when the variance reduction (VR), or fit between the data and the synthetics, exceeds a detection threshold.

We set up a moment tensor grid search for the Mendocino Triple Junction (MTJ) using four BDSN stations and virtual sources located every  $0.2^\circ$  in latitude and longitude and every 3 km in depth (Figure 2.43). We propose to run in parallel a system for small to moderate earthquakes (inversion of 380 seconds of 20-50 second period data) and a second one for large (M8+) earthquakes along the CSZ (inversion of 480 seconds

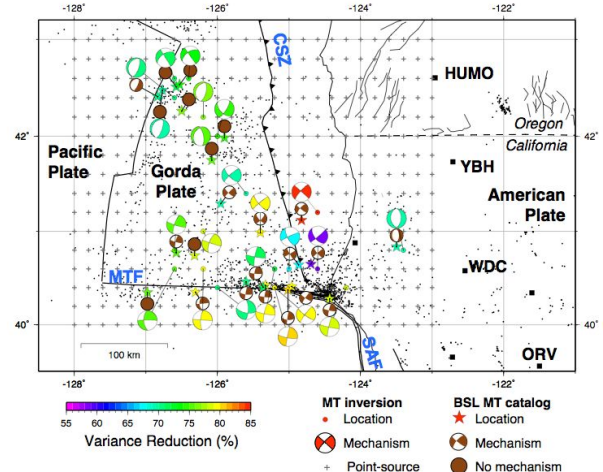


Figure 2.43: Map of the Mendocino Triple Junction region showing the grid of point sources (crosses), the four seismic stations (HUMO, ORV, WDC and YBH), the regional seismicity since 1990 (black dots), and the studied events that are shown in brown for the catalog solutions and are color-coded by the VR for the inversion solutions.

of 100-200 second period data). For large earthquakes, we also include an 84-second source time function in the GFs corresponding to the tested synthetic M 8.2 earthquake (Figure 2.44).

Because for large subduction zone earthquakes the problem grows into a near-field problem, we propose to employ quasi-finite-source adjusted GFs where GFs of  $n$  grid points are averaged in advance to generate composite GFs,  $G_{tot}$ , which take into account the source-receiver back-azimuth and by consequence the radiation patterns of each component (Figure 2.44):

$$G_{tot}(t) = \frac{\sum_{i=1}^n G_i(t)}{n}$$

Directivity can also be pre-included in the composite GFs, giving constraints on the nature of finite rupture (i.e. unilateral or bilateral) (Figure 2):

$$G_{tot} = \frac{\left[ G_1(t) + \sum_{i=2}^n G_i(t) \cdot \left( \frac{\Delta_{1-n}}{v_r} \right) \right]}{n}$$

where  $\Delta_{1-n}$  is the distance between Source 1 (reference source) and Source  $n$ , and  $v_r$  is the rupture velocity. The

moment tensor inversion itself is performed assuming a point-source analysis method, which maintains the computational speed.

### 21.3 Detection of large and potentially tsunamigenic earthquakes along the Cascadia Subduction Zone

We tested the concept on M4 to M7.1 earthquakes (Figure 2.43). The solutions obtained using a 1D velocity model (i.e. Gil7) agree well with the Berkeley moment tensor catalog solutions, confirming that this system is suitable for implementation in the MTJ region. However, because of the narrow band processing (0.02-0.05 Hz), the point-source inversion for a large M8.2 earthquake only fits a small part of the record. As a consequence, it does not recover the earthquake parameters. But we find that the 100-200 second passband gives a point-source location near the fault centroid, and the correct  $M_w$  and focal mechanism (VR= 54.6% in Figure 2.44). It is possible to improve the fit between the synthetics and the data (Figure 2.44c) after simultaneously summing the GFs of several grid points centered on the event centroid. Figure 2.44d shows that, by considering a northward rupture in the composite GFs and a rupture velocity of 3 km/sec, the corresponding earthquake solution has a larger VR and better estimates the focal parameters. Similar results are obtained for a M 8.4 synthetic seismic event, which presents an extended rupture (i.e. 480 km) and two major slip areas (Guilhem and Dreger, 2011). This method permits raising the detection level of large earthquakes and allows us to obtain more precise source parameters, by considering a range of QFS GFs for different directivity scenarios and source time durations.

### 21.4 Conclusion

We show that it is possible to rapidly detect and characterize the seismic activity of the MTJ region using an algorithm that performs moment tensor inversions. The QFS GFs allow more rapid detection of major events and more precise determination of their source parameters than is likely to be available using standard processing systems. Complete earthquake information is retrieved about 6 minutes after a M 4-7 earthquake and 8 minutes after a M 8+ earthquake and may allow for tens of minutes of warning in the near field.

### 21.5 Acknowledgements

Supported by the U.S. Geological Survey through external award G10AP00069.

### 21.6 References

Guilhem, A., and D. S. Dreger, Rapid detection and characterization of large earthquakes using quasi-finite-source

Green's functions in continuous moment tensor inversion, *Geophys. Res. Lett.*, 38, L13318, doi:10.1029/2011GL047550, 2011.

Kawakatsu, H., On the realtime monitoring of the long-period seismic wavefield., *Bull. Earth. Res. Inst.*, 73, 267-274, 1998.

Tsuruoka, H., H. Kawakatsu, and T. Urabe, GRiD MT (grid-based real-time determination of moment tensors) monitoring the long-period seismic wavefield, *Physics of the Earth and Planetary Interiors*, 175, 8-16, doi:10.1016/j.pepi.2008.02.014, 2009.

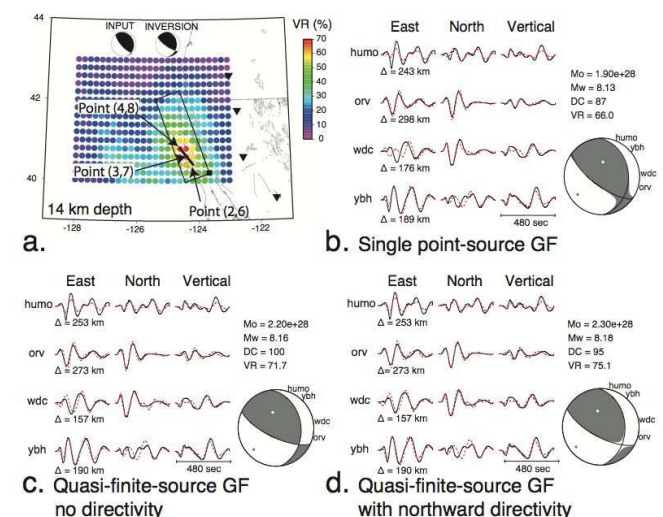


Figure 2.44: a) Map of the best VRs at 14 km depth obtained for a point-source moment tensor inversion for a synthetic M 8.2 earthquake (rectangle). The best mechanism (top, right) is compared to the input mechanism (top, left). Arrows point to the points that are considered in the multi-point source inversion. b) Best moment tensor solution obtained at Point (3,7). c) Moment tensor solution for the multi-point source inversion (no directivity). d) Moment tensor solution for the multi-point source inversion with a northward directivity.

## 22 Identifying Undetected Early Aftershocks Associated with the 12 August 1998 $M_w$ 5.1 San Juan Bautista Earthquake

Taka'aki Taira, Roland Bürgmann, Robert M. Nadeau

### 22.1 Introduction

Aftershocks are triggered by abrupt changes of stress induced by a larger earthquake. Detailed images of spatiotemporal changes in aftershock activity help delineate the mainshock rupture area. However, large numbers of early aftershocks are not detected because they are masked by large amplitudes and long duration of seismic coda waves from the mainshock and other aftershocks. *Peng and Zhao* (2009) have demonstrated that  $\sim 10,000$  aftershocks during the first three days following the 2004 M 6.0 Parkfield earthquake were undetected by the standard earthquake-detection algorithm of the Northern California Seismic Network (NCSN). We focus on the detection of uncatalogued aftershocks after the 12 August 1998  $M_w$  5.1 San Juan Bautista (SJB) earthquake. This event was the largest historic earthquake in the SJB area and was associated with a large slow slip event (*Uhrhammer et al.*, 1999). Additionally, *Nadeau and McEvilly* (2004) and *Templeton et al.* (2008) found accelerations in repeating microearthquake frequency accompanying the 1998 slow slip event.

### 22.2 Identification of Undetected Early Aftershocks

Following *Peng and Zhao* (2009), we have been identifying undetected early aftershocks with a cross-correlation based approach. We use waveforms from 248 SJB earthquakes detected by the NCSN during a 10-day period spanning the 1998 SJB earthquake (9 August through 18 August, 1998) as templates to identify additional, previously undetected earthquakes. Using continuous data recorded by the closest two seismic stations to the 1998 SJB event (BK.SAO and NC.BVY; less than 4 km from the mainshock), our preliminary analysis has detected  $\sim 900$  individual earthquakes, with the averaged cross-correlation threshold of 0.7 (Figure 2.45). We have identified four times more aftershocks than listed in the NCSN catalog (Figure 2.46). We also searched for small foreshocks immediately preceding the mainshock (e.g., *Dodge et al.*, 1996; *Bouchon et al.*, 2011), but no events were detected during the two minutes preceding the mainshock. We currently assign the locations of the detected events to that of the template events providing the highest cross-correlation values (Figure 2.46a).

With the detected early aftershocks, we find that a highly productive burst of aftershocks started 17 hours after the mainshock (Figure 2.46b). In this aftershock episode,  $\sim 100$  events occurred within a 3-hour period.

These aftershocks occurred in the northwest part of the rupture area (Figure 2.46b). This aftershock episode may be the result of the redistribution of stress induced by the 1998 SJB earthquake. Apparently strain and creepmeter data of the associated slow slip event do not resolve an acceleration of slip associated with this accelerated aftershock activity.

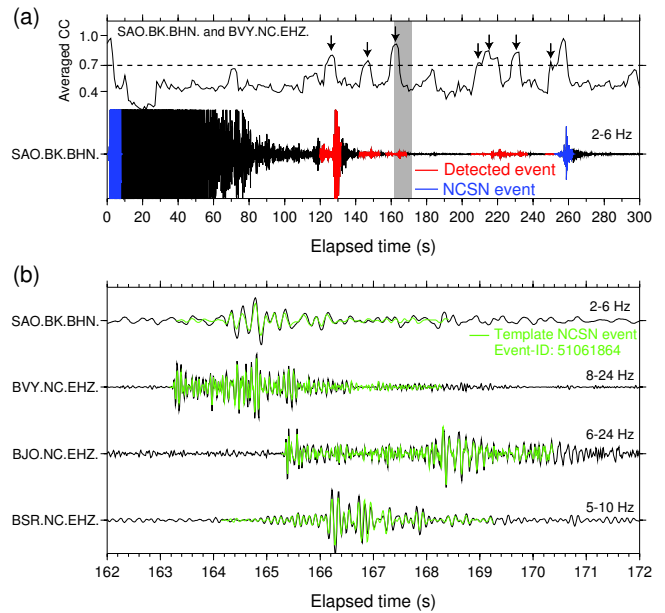


Figure 2.45: (a) Top panel shows averaged cross-correlation functions based on SAO.BK.BHN and BVY.NC.EHZ data. Highest cross-correlation values were plotted at individual time steps from cross-correlation functions for the 248 template events. Black arrows indicate identified events using the threshold with averaged cross-correlation value of 0.7 (dashed line). Bottom panel shows observed seismograms (black) recorded at BK.SAO in the N-S component with a 2-6 Hz bandpass filter. Waveforms shown in red and blue are the newly detected events and the NCSN events (the first 10-s data). (b) Detected early aftershock at  $\sim 160$  s after the mainshock shown in grey area in Figure 2.45a using the template event nc51061864 (M 0.85) occurring  $\sim 4$  days after the mainshock. Waveforms shown in black and green are the continuous and the template waveforms, respectively.

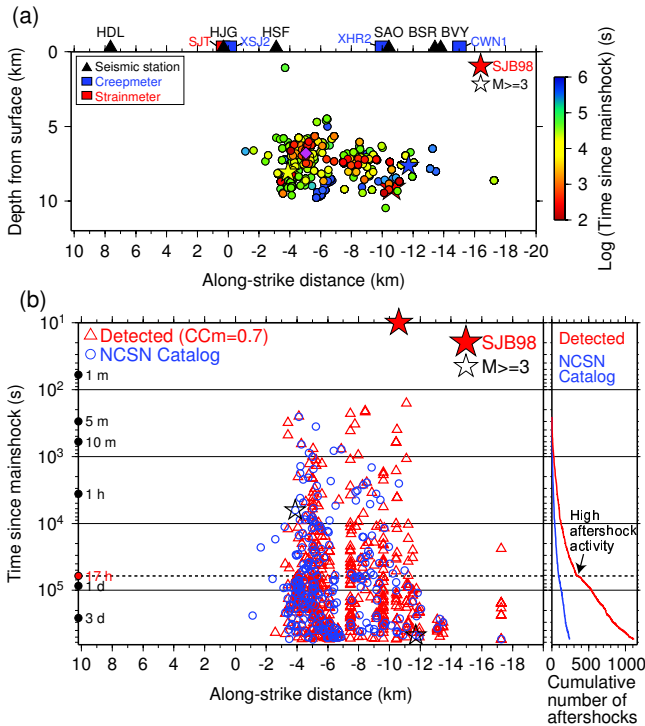


Figure 2.46: (a) Cross-section view of the newly detected and NCSN events (circles) along the San Andreas fault in the SJB area (NW to SE) color-coded by the logarithmic time after the mainshock (red star). The purple diamond is the location of the characteristically repeating earthquake sequence shown in Figure 2.47. (b) Left panel shows the occurrence times of aftershocks since the 1998 SJB mainshock as a function of the along-strike distances. The blue circles are the events listed in the NCSN catalog and the red triangles are newly detected events from the cross-correlation analysis. Right panel shows the cumulative numbers of aftershocks from the NCSN catalog (blue) and this study (red).

### 22.3 Characteristically Repeating Microearthquakes

As a complementary study to *Nadeau and McEvilly (2004)* and *Templeton et al. (2008)*, we are identifying smaller characteristically repeating earthquakes around the rupture area of the 1998 SJB earthquake. We have analyzed  $\sim 6,000$  SJB earthquakes in the NCEDC earthquake catalog between 1984 and June 2011 and found  $\sim 350$  candidate repeating earthquake sequences. By integrating the early aftershock and repeating microearthquake catalogs, we found that some of the newly identified early aftershocks are characteristically repeating microearthquakes (Figure 2.47). We now focus on completing the repeating microearthquake catalog in the vicinity of the 1998 SJB earthquake, to better characterize the accelerated deep fault creep induced by the 1998 SJB mainshock.

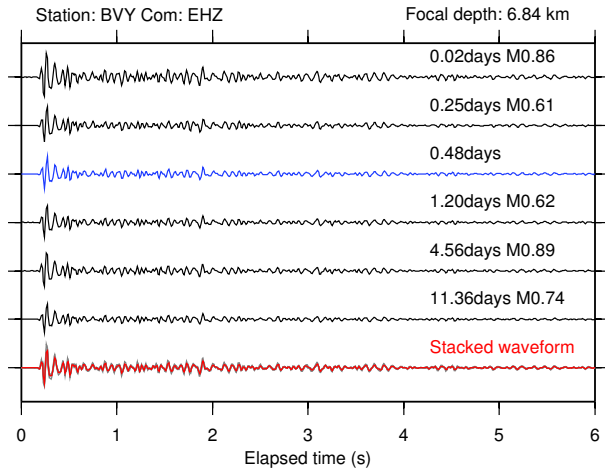


Figure 2.47: Characteristically repeating earthquakes identified from our preliminary analysis. An example of vertical seismograms recorded at station BVY. Blue waveform is from a newly identified early aftershock that is not listed in the NCEDC catalog. The bottom waveform shown in red is a stack of the six seismograms (gray in the bottom trace) for six individual repeating earthquakes shown as the first to sixth traces. Also shown are the elapsed times (days) since the 1998 SJB mainshock and the NCEDC magnitudes.

### 22.4 Acknowledgements

We thank R. Turner, P. Audet, and I. Johanson for discussion, and NCEDC for data collection and distribution. This work is supported by the National Science Foundation EAR-0951430.

### 22.5 References

Bouchon, M., H. Karabulut, M. Aktar, S. Özalaybey, J. Schmittbuhl, and M.-P. Bouin, Extended nucleation of the 1999 Mw 7.6 Izmit earthquake, *Science*, 331, 877-880, doi:10.1126/science.1197341, 2011.

Dodge, D.A., G.C. Beroza, and W.L. Ellsworth, Detailed observations of California foreshock sequences: Implications for the earthquake initiation process, *J. Geophys. Res.*, 101(B10), 22,371-22,392, 1996.

Nadeau, R. M. and T.V. McEvilly, Periodic pulsing of characteristic microearthquakes on the San Andreas Fault, *Science*, 303, 220-222, 2004.

Peng, Z. and P. Zhao, Migration of early aftershocks following the 2004 Parkfield earthquake, *Nature Geosci.*, 28, 877-881, 2009.

Templeton, D., R.M. Nadeau, and R. Bürgmann, Behavior of repeating earthquake sequences in Central California and the implications for subsurface fault creep, *Bull. Seismol. Soc. Am.*, 98, 52-65, 2008.

Uhrhammer, R., L.S. Gee, M. Murray, D. Dreger, and B. Romanowicz, The Mw 5.1 San Juan Bautista, California earthquake of 12 August 1998, *Seismol. Res. Lett.*, 70, 10-18, 1999.

# 23 Persistent Scatterer InSAR Analysis of Berkeley Hills Landslides

Ling Lei and Roland Bürgmann

## 23.1 Introduction

Over the past decade, InSAR has been proven to be a powerful tool for studying earth processes such as volcano deformation, tectonic deformation, and land subsidence. InSAR provides a spatially continuous observation of the change in line of sight between the satellite and the ground over the time period of an interferogram. It has the potential to resolve spatially and temporally complex deformation. But the geometrical and temporal de-correlation with atmospheric error has long been its limitation. Persistent Scatterer InSAR (PS-InSAR) has the advantage of overcoming these limiting factors. The persistent scatterer, which can keep the phase stable in the temporal series, can be used

to get surface deformation by analyzing the time-series differential phase variation. They are typically radar-bright and phase stable structures such as building corners, telephone poles and rock spars. PS-InSAR is an approach that estimates several contributions: atmospheric disturbances, orbital errors, deformation signal, and topographical errors. It is particularly well suited to monitoring deformation over urban areas, where an abundance of man-made structures results in large numbers of suitable radar-bright and phase-stable reflectors.

## 23.2 Study Area and Data Set

The Berkeley Hills are located in the eastern San Francisco Bay area. The active Hayward Fault (HF) bounds

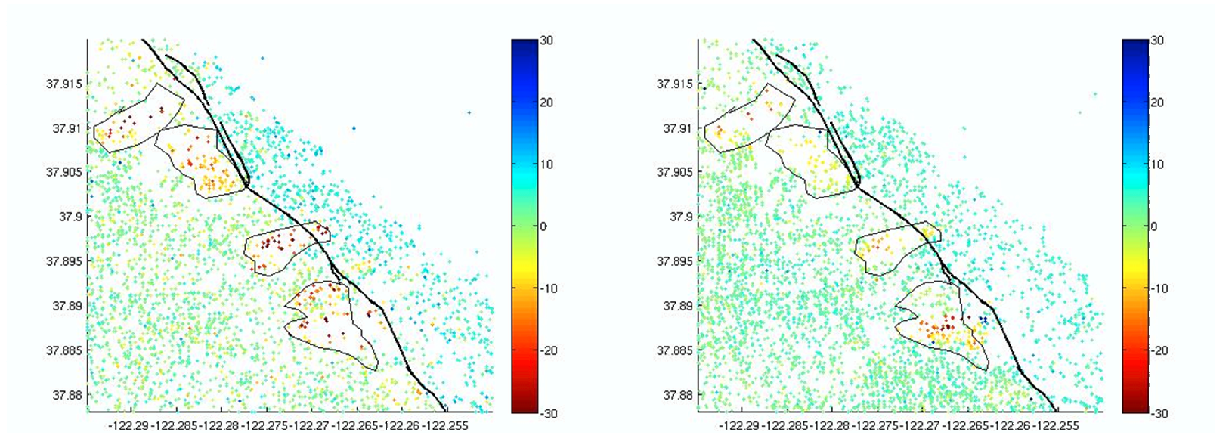


Figure 2.48: Mean LOS velocity with ERS and RST Data

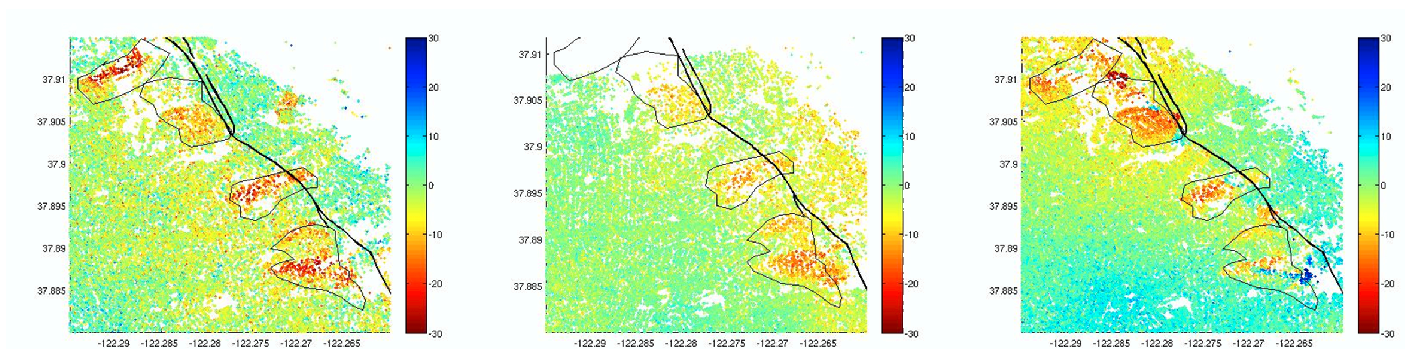


Figure 2.49: Mean LOS velocity with TSX Data

the western margin of the East Bay Hills (EBH), which rises to about 370 m above sea level. On the Berkeley Hills there are four large, slow moving, deep-seated landslides. All the landslides extend through residential areas and move on the order of cm/year, each covering an area of roughly 0.25-1.00 km<sup>2</sup>. These slides are located in a rapidly uplifting zone adjacent to the Hayward fault. A lot of damage to homes, breakage of underground utility pipes, and confusion over property lines has been caused by landslides over the years, although deformation on these landslides is typically small and slow. It is currently not well understood how the landslides respond to seismic activity on the Hayward fault, but significant deformation is conceivable under wet conditions and given a moderate to large seismic event. Resolving the kinematics of landslides is a pre-requisite for improving understanding of the mechanics of these potentially hazardous features. Here we will evaluate the potential and limitations of TerraSAR-X data for monitoring deformation of landslides. The TerraSAR-X satellite operates in an 11 day repeat orbit at an altitude of 514 km. The rather short orbit repeat cycle and the electronically steerable antenna allow fast and frequent imaging of a particular site. The frequent interferometric coverage can help especially with monitoring events in shorter time scales. Fast events can be detected and atmospheric delay errors can be reduced by averaging many interferograms. The interferometric processing for the study area was performed based on three sets of TerraSAR-X Spotlight SLC images and Stripmap SLC images delivered by DLR. Table 2.2 shows their beam numbers, incidence angles and pass directions. The TerraSAR-X images were acquired over the Bay Area, particularly around the active landslides, coastal subsidence and shallow Hayward fault creep near the city of Berkeley. The data acquisition interval is from May 2009 to August 2010.

Beam No.	Inc. Angle	Track Type	No. of Data
Strip_003	21	Descending	21
Spot_038	38	Descending	17
Spot_049	49	Descending	18

Table 2.2: Data sets information

### 23.3 Data Processing

The processing was started from SLC data and then coregistered to the same geometry. To minimize the effect of topography on interferograms, we applied a two-pass differential interferometry approach using SRTM 1-arc-second DEM heights as a reference. The Stanford Method for Persistent Scatterers (StaMPS) was applied. It was developed in Stanford University by Andy Hooper. It is a public-domain tool of InSAR processing. All of these images were used to identify persistent and coherent pixels. The wrapped phase of the PS pixels was

selected and the improved phase unwrapping algorithm adopted.

### 23.4 Results and Analysis

A previous study by *Hilley et al.* used InSAR data from European Remote Sensing satellites (ERS-1,2) from 1992-2000 and Radarsat from 2001 to 2006 to image the landslides and estimate rates of motion (Figure 2.48). The Permanent Scatterer InSAR analysis was utilized. The slow-moving landslides of the Berkeley Hills are clearly indicated by the faster moving yellow and red pixels. Since all the results rates were measured in the direction of the look angle of the satellite, it was hard to compare them with different satellite data or the same satellite data with different look angles. However, assuming that most of the displacement along these landslides follows the average four degree downhill slope, we projected the LOS velocity to downslope velocity, shown in Figure 2.49. You can see that the PS density of TerraSAR-X data is much higher than ERS or Radarsat, and most of the results are consistent with southwest motion of the landslides. The negative mean LOS velocity in the landslides area is consistent with landslide motion moving away from the satellite. For future work, we hope the four beams of TerraSAR-X data from different viewing geometries will significantly improve our ability to fully characterize the kinematics and temporal patterns of the landslides.

### 23.5 Acknowledgements

We thank the German Aerospace Centre (DLR) for providing TerraSAR-X data for this project. We thank Andy Hooper for supporting StaMPS software.

### 23.6 References

- Hilley, G., R. Bürgmann, A. Ferretti, F. Novali and F. Rocca, Dynamic of slow-moving landslides from permanent scatterer analysis, *Science*, 304, 1952-1955, 2004.
- TerraSAR-X Ground Segment Basic Product Specification Document, TX-GS-DD-3302.
- TerraSAR-X Ground Segment Level 1b Product Format Specification, TX-GS-DD-3307.
- Bürgmann, R., E. Fielding, and J. Sukhatme, Slip along the Hayward fault, California, estimated from space-based synthetic aperture radar interferometry, *Geology*, 26, 559-562, 1998.
- Eineder, M., N. Adam, and R. Bamler, Spaceborne Spotlight SAR Interferometry With TerraSAR-X, *IEEE Trans. Geosci. Remote Sense.*, 5, 1524-1535, 2009.
- Hooper, A., H. Zebker, P. Segall and B. Kampes, A new method for measuring deformation on volcanoes and other natural terrains using InSAR persistent scatterers, *Geophys*, 31, 2004.

# 24 Toward Global Waveform Tomography with the SEM: Improving Upper-Mantle Images at Shallow Depths

Scott French, Vedran Lekic, and Barbara Romanowicz

## 24.1 Introduction

The SEMum upper-mantle  $V_S$  model (Lekic and Romanowicz, 2011) was developed using the spectral element method (SEM: e.g. Komatitsch and Vilotte, 1998) to invert long-period ( $T \geq 60$  s) waveforms of fundamental and overtone mode surface waves. SEM global waveform inversion was made feasible partly through use of a mode-coupled SEM (Capdeville et al., 2003), combined with an innovative smooth crustal model. The 60 km crustal layer allows the SEM to take long time steps, thus speeding computation, at the expense of complicating interpretation of the shallowest upper-mantle structure.

Our goal has been to produce an updated model (SEMum2) using a more geologically-plausible fictitious Moho for the crustal layer. This update would have the immediate benefit of easing interpretation of some uppermost upper-mantle structure. In the future, we intend to include SEMum2 in the initial model for a forthcoming whole-mantle inversion, using shorter period waveform data ( $T \geq 40$  s). Thus, it is advantageous to perform the update *now*, while still using the 60 s data set so that SEM simulation is comparatively inexpensive.

## 24.2 Crustal model development

SEM solution accuracy is strongly affected by mesh fidelity to the underlying earth model, requiring interior boundaries (Moho, 410 km, etc...) to be matched with element faces. Time-stability of the SEM is determined by the minimum ratio between spatial discretization and wave speed (the Courant-Friedrichs-Lewy, or CFL condition), with the maximum stable time-step determining the overall cost of time-integration.

In a pure global SEM (e.g. Tromp, et al., 2008), the CFL condition is dominated by high  $V_P$  in the *core*. If the core is replaced with a modal solution (Capdeville, et al., 2003), then small spatial discretization in the thin *oceanic crust* dominates - leading to a less restrictive, but still prohibitively small, time-step. As a solution, Lekic and Romanowicz (2011) developed a new crustal model: a radially-anisotropic smooth crustal layer of uniform 60 km thickness, designed to fit observed surface-wave dispersion maps (Shapiro and Ritzwoller, 2002). This scheme provides a simpler alternative to a true “homogenization” of an *a priori* crustal model (e.g. Capdeville and Marigo, 2007), while also supplying independent constraints on the effect of crustal structure on the wavefield.

For SEMum2, we adopt a more geologically plausible

laterally-varying layer thickness, at the expense of a more restrictive CFL condition. Starting from Crust2.0 Moho depth (Bassin and Masters, 2000), we restrict crustal thickness  $H$  to the interval  $H \in [30, 60]$  km and filter at 2x lateral resolution of the SEM mesh. We seek “crust-equivalent” *anisotropic*  $V_S$  structure (e.g. Backus, 1962) that fits observed surface-wave dispersion and is parameterized with depth in Gauss-Lobatto-Legendre interpolants (GLL), as used in the SEM. The crustal layer is generated following a two-step procedure:

(1) We define a space of admissible radially-anisotropic GLL models  $V_{S,iso} \in [3, 4.5] \text{ km s}^{-1}$ ,  $V_{SH}^2/V_{SV}^2 \in [0.8, 1.2]$  from which we draw  $\sim 20\text{k}$  realizations  $\{\mathbf{m}_i\}$  and calculate dispersion curves for layer thickness  $H \in [30, 60]$  km and bathymetry  $h \in [0, 6]$  km. Group-velocity dispersion maps (25 - 60 s) are resampled on a uniform grid of knots, and dispersion curves are estimated for all  $\{\mathbf{m}_i\}$  through interpolation to local seafloor and Moho topography ( $H, h$ ). Best-fitting GLL models are selected for each knot, where misfit is measured in the  $L_1$  norm to reduce sensitivity to outlier measurements common at short periods, with additional weighting by measurement uncertainty and tunable anisotropy regularization.

(2) We next perform a linearized inversion in a neighborhood surrounding the selected model using the generalized least-squares formalism (Tarantola and Valette, 1982). We use individual group-velocity kernels for each model knot, reflecting local bathymetry and fictitious Moho, which are recalculated following each iteration. Upper-mantle structure from SEMum is assumed. After 3 iterations, mean absolute misfit over all periods and model knots fell into the target range of 50 - 60  $\text{m s}^{-1}$ . The resulting model allows a **5x** time-step prolongation over direct meshing of Crust2.0.

## 24.3 Preliminary update and discussion

We refer the reader to Lekic and Romanowicz (2011) for a detailed discussion of the waveform inversion scheme. The SEM is used to forward model fundamental and overtone mode surface waves ( $T \geq 60\text{s}$ ), which are inverted for upper-mantle structure using NACT waveform sensitivity kernels following the generalized least-squares formalism. Group-velocity data ( $T \leq 150\text{s}$ ) is included in the inversion for consistency. We follow an identical procedure, substituting the new crustal model as well as new crustal corrections for use with NACT, developed in a manner similar to that of Lekic, et al. (2010).

To date, we have performed one update iteration, and SEM simulation for the second is ongoing. We antici-

	L		T		Z	
fund	0.360	0.388	0.283	0.413	0.326	0.354
high	0.248	0.327	0.293	0.385	0.275	0.310
mixed	0.299	0.320	0.212	0.316	0.283	0.296

Table 2.3:  $\|u_{obs} - u_{pred}\|^2 / \|u_{obs}\|^2$  for SEMum2 and [SEMum] by data-type and component. Values reflect 80 % of the total data set, but are considered representative.

pate two iterations will be required for the full update. Preliminary results show mantle structure highly consistent with that of SEMum. Using the East Pacific Rise as an example, Figure 2.50 demonstrates that (first-iteration) SEMum2 achieves its goal of improving shallowest upper-mantle structure, while further enhancing agreement with regional studies already exhibited by SEMum. Waveform relative square residuals are shown in Table 2.3 above for SEMum and SEMum2. These values reflect only the portion of the data set with the most recent SEM synthetics completed, or approximately 80 % thereof. We consider these values representative.

In the near future, we will complete the second update iteration, at which point we anticipate SEMum2 will have stabilized. Thereafter, we will begin data collection for the whole-mantle inversion, potentially using new ( $T \geq 40$  s) SEMum2 synthetics for waveform selection.

## 24.4 Acknowledgements

This work was supported by the National Science Foundation (EAR-0738284). SF acknowledges support from the NSF Graduate Research Fellowship Program. SEM computations were performed at the DOE National Energy Research Scientific Computing Center (NERSC). We thank Yann Capdeville for providing us with the mode-coupled SEM implementation.

## 24.5 References

Backus, G., Long-wave elastic anisotropy produced by horizontal layering, *J. Geophys. Res.*, 67, 4427-4440, 1962.

Bassin, C.G.L. and G. Masters, The current limits of resolution for surface wave tomography in North America, *EOS, Trans. Am. Geophys. Un.*, 81, F897, 2000.

Capdeville, Y. and Marigo, J., Second order homogenization of the elastic wave equation for non-periodic layered media, *Geophys. J. Int.*, 170(2), 823-838, 2007.

Capdeville, Y., E. Chaljub, J.P. Vilotte, and J.P. Montagner, Coupling the spectral element method with a modal solution for elastic wave propagation in global earth models, *Geophys. J. Int.*, 152, 34-67, 2003.

Harmon, N., D.W. Forsyth, and D.S. Weeraratne, Thickening of young Pacific lithosphere from high-resolution Rayleigh wave tomography: A test of the conductive cooling model, *Earth Planet. Sci. Lett.*, 278, 96-106, 2009.

Komatitsch, D. and J.P. Vilotte, The spectral element method: an efficient tool to simulate the seismic response of 2D and 3D geological structures, *Bull. Seism. Soc. Am.*, 88(2), 368-392, 1998.

Kustowski, B., G. Ekstrom, and A. Dziewonski, Anisotropic shear-wave velocity structure of the Earth's mantle: a global model, *J. Geophys. Res.*, 113, B06306, 2008.

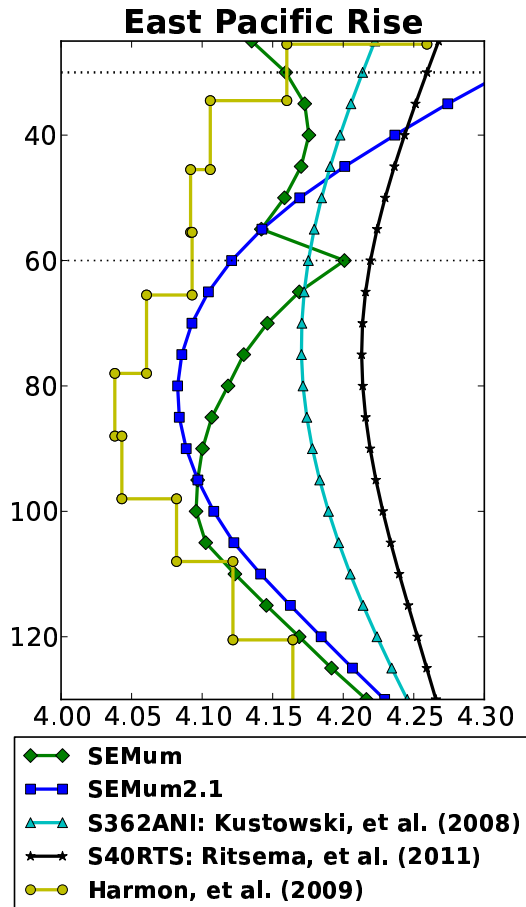


Figure 2.50: Comparison of  $V_S$  profiles at an arbitrary point beneath the EPR. Dotted lines at 30 and 60 km indicate Moho depth in the old and new crustal models. (Mean of *Harmon, et al. (2009)* regional  $V_{SV}$  model shown)

Lekic, V. and B. Romanowicz, Inferring upper-mantle structure by full waveform tomography with the spectral element method, *Geophys. J. Int.*, 185(2), 799-831, 2011.

Lekic, V., M. Panning, and B. Romanowicz, A simple method for improving crustal corrections in waveform tomography, *Geophys. J. Int.*, 182(1), 265-278, 2010.

Li, X.D. and B. Romanowicz, Comparison of global waveform inversions with and without considering cross-branch modal coupling, *Geophys. J. Int.*, 121, 695-709, 1995.

Ritsema, J., A. Deuss, H. J. van Heijst and J. H. Woodhouse, S40RTS: a degree-40 shear-velocity model for the mantle from new Rayleigh wave dispersion, teleseismic traveltime and normal-mode splitting function measurements. *Geophys. J. Int.*, 184, 1223-1236, 2011.

Shapiro, N. and M. Ritzwoller, Monte-Carlo inversion for a global shear-velocity model of the crust and upper mantle, *Geophys. J. Int.*, 151(1), 88-105, 2002.

Tarantola, A. and B. Valette, Generalized nonlinear inverse problems solved using the least squares criterion, *Rev. Geophys. Space Phys.*, 20, 219-232, 1982.

Tromp, J., D. Komatitsch, and Q. Liu, Spectral-element and adjoint methods in seismology. *Comm. Comp. Phys.*, 3(1), 1-32, 2008.

# 25 On the Interpretation of SKS Splitting Measurements in the Presence of Several Layers of Anisotropy

Barbara Romanowicz and Huaiyu Yuan

## 25.1 Summary

Concerns over the validity of expressions derived by *Montagner et al.* (2000; referred to as MGL00) that link SKS splitting measurements to the variation with depth of anisotropic parameters in the upper mantle have been recently expressed (*Silver and Long, 2011*; referred to as SL11), pointing out that the long period approximations applied by these authors may not be valid for the frequency range commonly used in SKS studies, and in particular, that the anisotropy splitting parameters should depend on the order in which different anisotropy layers are arranged with depth. We show that measurements of splitting time  $\delta t$  and fast axis direction  $\psi$  performed at individual azimuths do depend on the order of layering; however, the expressions of MGL00 concern station averaged quantities that do not depend on the order of layers. It is therefore correct to use these expressions in joint inversions of surface waveforms and SKS station averaged splitting measurements. On the other hand, the depth-dependent sensitivity of surface waveforms naturally provides constraints on the order of layering.

We extend the expressions of MGL00 to the case of a tilted axis of symmetry and non vertical incident waves, and show that station averaged estimates of "effective" splitting parameters: splitting time, fast axis direction and tilt of the fast axis, can be related to the integral with depth of quantities which now depend not only on the local splitting time and fast axis direction, but also on the local tilt of the fast axis, thus also providing constraints also on the variation of the tilt with depth. Thus, combining body wave and surface wave observations also has the potential for constraining the variation with depth of the tilt of the fast axis of anisotropy, a geodynamically important parameter.

## 25.2 Two Layer Examples

We first consider a two layer case and show that the formalism of MGL00 can also lead to exactly the same derivation of azimuthal dependent individual SKS parameters as in (*Silver and Savage, 1994*). Detailed derivation is seen in *Romanowicz and Yuan (2011*; referred to as RY11). Figure 2.51 shows the two-layer anisotropic models and Figure 2.52 shows synthetic splitting parameters  $\delta t$  and  $\psi$  computed using Equation 12 of RY11 and the approximated terms with 1st order and 2nd order of  $\omega\delta t$ , where  $\omega$  is the peak period of the SKS waveform and  $\delta t$  is the splitting time. Synthetic waveforms generated by the two-layer models (Figure 2.52) are also measured for

splitting parameters, which are also plotted for comparison. In all models, Equation 12 of RY11 gives the same azimuthal dependent variation of  $\delta t$  and  $\psi$  shown in SL11 (red), which is confirmed by individual event measurements of the synthetic waveforms (dashed black). Note the splitting parameters computed using expressions up to 2nd order terms (green) follow the back-azimuthal pattern, but blow up near the one-layer equivalent apparent "fast" (vertical gray line) and "slow" axis directions. Using the first terms only, Equation 12 of RY11, which is equivalent to Equations 21 and 22 in MGL00 in the two layer case, gives azimuthally invariant effective  $\delta t$  and  $\psi$  (solid black), which are identical to the measured station averages (dashed blue).

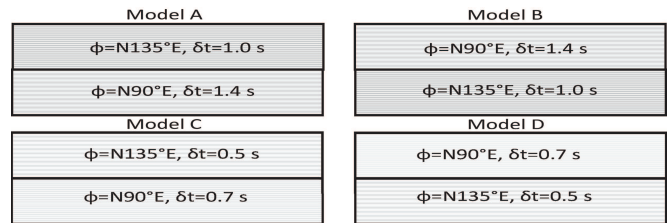


Figure 2.51: Two layer test models with  $\psi$  and  $\delta t$  shown for each layer. A and B have flipped layer order, and C and D are identical to A and B with only half  $\delta t$ .

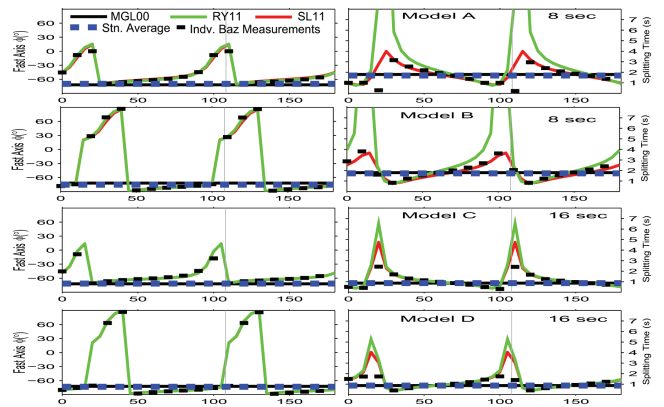


Figure 2.52: Predicted (solid) and measured (dashed) splitting parameters for model A&B at 8 s period and C&D at 16 s.

## 25.3 Harmonic Decomposition

Figure 2.52 also shows that individual splitting measurements tend to become singular near particular az-

imuths  $\psi$ ; therefore it is not wise to apply the long period approximation to Equation 12 in RY11. Neither MGL00 nor we use any azimuthally dependent individual event splitting data in the joint tomographic inversion. As shown in RY11, after extending to the case of multiple layers, the transverse component displacement at the top of the anisotropic model can be decomposed as  $u_T^n = A \cos 2\psi + B \sin 2\psi + C$ , in which  $\psi$  is event back-azimuth, A and B take the form of summation over layers of splitting time  $\delta t_i$  and fast axis direction  $\psi_i$  within each layer, and C is independent of the event back-azimuth  $\psi$ . Equating A and B to the one-layer effective splitting time  $\delta \hat{t}$  and fast axis direction  $\hat{\psi}$  (Equations 16 to 18 of RY11):  $A = 0.5 \sin(2\hat{\psi}) \delta \hat{t} \dot{u}_{R_0}$  and  $B = 0.5 \cos(2\hat{\psi}) \delta \hat{t} \dot{u}_{R_0}$ , which eventually leads to the expression used in MGL00 and in our joint inversion (Eqn. 19 of RY11):

$$\sin(2\hat{\psi}) \frac{\delta \hat{t}}{2} = \int_0^a \frac{G(z)}{V_s(z)L(z)} \sin 2\Psi_G(z) dx$$

$$\cos(2\hat{\psi}) \frac{\delta \hat{t}}{2} = \int_0^a \frac{G(z)}{V_s(z)L(z)} \cos 2\Psi_G(z) dx$$

G and L are the anisotropic parameters of the model at depth (z) to be solved for. Noteworthy is that using tabulated values of the station averaged splitting time  $\delta \hat{t}$  and fast axis direction  $\hat{\psi}$  avoids instability in the individual splitting measurements and yields a robust quantity which can also be obtained from measurements of the splitting intensity (Chevrot, 2000) when measurements in a wide enough back-azimuth range are available (Figure 2.53). Note these quantities are independent of the order of layers; in the joint inversion the layering constraints come naturally from the surface waves, at least for the shallow upper mantle.

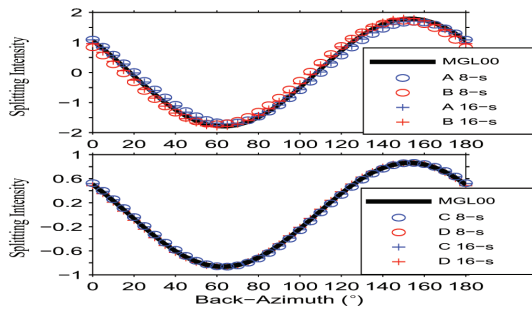


Figure 2.53: Predicted (solid line;  $\sin 2(\hat{\psi} - \psi) \frac{\delta \hat{t}}{2}$ ) and measured (symbols) splitting intensity for models A-D at 8 s period (top) and 16 s (bottom).

## 25.4 Dipping symmetry axis

The formalism of RY11 can also be generalized to the case of tilted fast symmetry axis (Equations 20-32 of RY11). After the same type of analysis as for the horizontal axis of symmetry, but with  $\Theta$  and  $\Phi$  for the tilt from

the horizontal plane and azimuth from north, by defining  $x = \cos(\pi - 2\Theta)$ , the tomographic system of equations can be written as:

$$\sin(2\hat{\psi}) \frac{\delta \hat{t}}{2} \cos^2 \hat{\Theta} = \int_0^a \frac{G(z)(1-x) \sin 2\Psi_G(z)}{2V_s(z)L(z)} dx$$

$$\cos(2\hat{\psi}) \frac{\delta \hat{t}}{2} \cos^2 \hat{\Theta} = \int_0^a \frac{G(z)(1-x) \cos 2\Psi_G(z)}{2V_s(z)L(z)} dx$$

$$\sin(2\hat{\Theta}) \frac{\delta \hat{t}}{2} \sin^2 \hat{\psi} = \int_0^a \frac{G(z)\sqrt{(1-x^2)} \sin 2\Psi_G(z)}{2V_s(z)L(z)} dx$$

$$\cos(2\hat{\Theta}) \frac{\delta \hat{t}}{2} \sin^2 \hat{\psi} = \int_0^a \frac{G(z)\sqrt{(1-x^2)} \cos 2\Psi_G(z)}{2V_s(z)L(z)} dx$$

Here also the one-layer effective splitting time  $\delta \hat{t}$ , fast axis symmetry axis  $\hat{\psi}$  and the newly introduced apparent tilt  $\hat{\Theta}$  can be obtained from measurements and can be used to form the splitting intensity in the presence of a tilted symmetry axis (Equations 31 and 32 of RY11). Figure 2.54 shows that the analytic prediction of the splitting intensity agrees with the measurements of the synthetic waveforms generated by the two-layer models very well.

To conclude, the results presented here provide a framework for the extension of the joint inversion of surface waveforms and SKS splitting data to constrain the tilt of the fast axis as a function of depth.

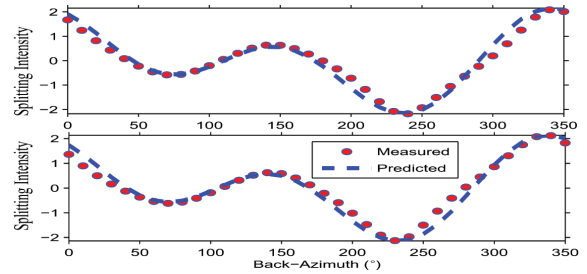


Figure 2.54: Predicted (dashed line) and measured (dots) splitting intensity for models at 8 s period (top) and 16 s (bottom). Note the break of  $180^\circ$  symmetry by introducing  $\Theta$ .

## 25.5 References

- Chevrot, S., Multichannel analysis of shear wave splitting, *J. Geophys. Res.*, *105*, 21579-90, 2000.
- Montagner, J.-P., Griot-Pommeroy, D.-A., and Lave, J., How to relate body wave and surface wave anisotropy?, *J. Geophys. Res.*, *105*, 19,015-19,027, 2000.
- Romanowicz, B., and Yuan, H., On the interpretation of SKS splitting measurements in the presence of several layers of anisotropy, *Geophys. J. Int.*, submitted, 2011.
- Silver, P.G., and Long, M.D., The non-commutativity of shear wave splitting operators at low frequencies and implications for anisotropy tomography, *Geophys. J. Int.*, *184*, 1415-1427, 2011.
- Silver, P.G., and Savage, M.K., The interpretation of shear-wave splitting parameters in the presence of two anisotropic layers, *Geophys. J. Int.*, *119*, 949-963, 1994.

## 26 Anisotropic Stratification in the Continental Upper Mantle

Huaiyu Yuan and Barbara Romanowicz

### 26.1 Introduction

The Berkeley North American regional azimuthal anisotropy model reveals the presence of three anisotropic layers throughout the stable part of the North American cratonic upper mantle (*Yuan and Romanowicz, 2010*). While in the bottom asthenospheric layer the fast axis direction is parallel to the current plate motion direction, the top two lithospheric layers have distinct fast axis directions, with ancient suture zone trending directions in the top layer and a general north-south direction in the bottom layer, respectively. The boundary between the two lithospheric layers, as defined by systematic changes in the direction of azimuthal anisotropy, correlates well with the sharp mid-lithospheric negative velocity boundary found by available S-wave receiver function measurements. This spatial correlation suggests that the two boundaries, found by the surface wave inversion and receiver functions, may share a common origin, possibly during the lithosphere formation, which indicates that accretion by shallow subduction may have played an important role in the North American craton formation (*Yuan and Romanowicz, 2010; Yuan et al., 2011*).

In this study, we look for upper mantle anisotropy signatures globally. Is the anisotropy stratification observed in North America a common feature in the cratons worldwide? If so, can we infer systematic anisotropy domains in the continents' and oceans' upper mantle (i.e. lithosphere and asthenosphere)? What about the anisotropy directions within each domain? Can we see the plate shear under continents? Answers to these imminent questions would put tighter constraints on evaluating how plate tectonics works and the rules of shallow subduction versus plume underplating in early stage craton formation worldwide (e.g. *Lee, 2006; O'Reilly and Griffin, 2006*).

### 26.2 Global Inversion

Taking advantage of a global isotropic and radially anisotropic shear wave velocity model developed using the Spectral Element Method (SEMum; *Lekic and Romanowicz, 2011*), we expand our regional azimuthal anisotropy inversion to the globe. We start with the global dataset of *Lekic and Romanowicz (2011)*, in order to cross-validate the results in North America (developed using a different dataset that utilizes the USArray; *Yuan and Romanowicz, 2010*). Following the ray path density and azimuthal coverage, we parameterize the globe approximately in nodes of 400- and 800-km spacing in continents and oceans, respectively. The vertical node spacing varies from 30-50 km above the transition zone to 100-150 km down to 1000 km depth. We perform a

two-step inversion: in the first step both isotropic Vs and radial anisotropy  $\xi = (V_{sh}/V_{sv})^2$  are allowed to vary in our new model mesh while azimuthal anisotropy remains zero, and in the second step the inverted Vs and  $\xi$  from the first step remain fixed and azimuthal anisotropy parameters Gc and Gs are inverted.

### 26.3 Preliminary Results

Our preliminary results indicate that globally the upper mantle is clearly stratified (Figure 2.55). The 1D depth profile of the azimuthal anisotropy strength shows that under the continents the anisotropy strength (thick blue line) peaks above 100 km in the shallow upper mantle. A secondary local maximum develops around 150 km, and the anisotropy decreases rapidly to 200-250 km depth. This layered shallow upper mantle is consistent with our previous observations in the North American craton. In fact, the mean values of the anisotropy strength in North America from this study (right panel in Figure 2.55b) are nearly identical to those of our regional study (Figure 3c in *Yuan et al., 2011*) in the upper 250 km, which are constrained by different waveforms recorded only at North American stations. The difference below 250 km is due to the enhanced depth sensitivity by the SKS dataset in the regional study (Figure 2.553a in *Yuan et al., 2011*). We will soon include the SKS dataset in the global study.

In North America, the averaged anisotropy direction (left panel in Figure 2.55b) reaches the averaged absolute plate motion (APM) direction (HS3-NUVEL 1A; *Gripp and Gordon, 2002*) at  $\sim 250$  km. This suggests that 1) well developed plate shear occurs in the North American asthenosphere at this depth (250 km), and 2) the anisotropic domains associated with local maxima in anisotropy strength (right panel in Figure 2.55b) are within the lithosphere. These were confirmed independently in our NA regional study (*Yuan and Romanowicz, 2010*). Obviously Figure 2.55c shows the same conclusions can be drawn for the Australian plate, except that the plate shear occurs at shallower depth ( $\sim 200$ km), suggesting thinner Australian lithospheric thickness than in North America.

Another interesting feature comes from the 1D oceanic anisotropy strength profile (thin red line in Figure 2.55a). In addition to a shallow depth (60-70km) secondary peak that may be associated with the plate shear between the young oceanic lithosphere and underlying asthenosphere, the major peak of anisotropy occurs below 150 km. Close examination of the 3D global anisotropy variations (Fig-

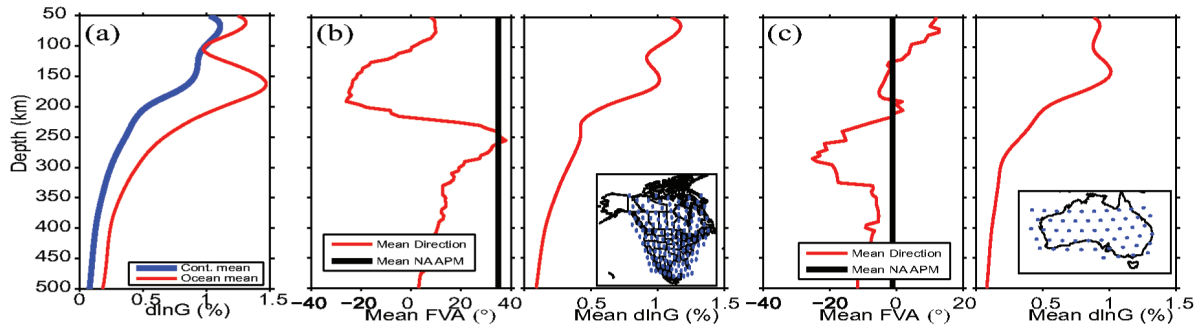


Figure 2.55: (a) Global depth profiles of azimuthal anisotropy strength ( $d\ln G$ ) averaged for continents and oceans, respectively. (b) Regional depth profiles of anisotropy fast axis direction (North at 0; in a clockwise direction) and strength for North America averaged from model nodes shown in the inset. Vertical black line is the averaged absolute plate motion direction (HS3-NUVEL 1A) of these model points. (c) Same as (b) but for the Australian continent.

ure 2.56) shows this signature is closely related to the prominent positive radial anisotropy  $\xi$  in the Pacific and India/Australia plates.

## 26.4 Future Work

We are working on including a global SKS dataset, which will significantly improve the depth sensitivity to anisotropy down to the transition zone (Romanowicz and Yuan, 2011; Yuan *et al.*, 2011). In addition, the new version of the global model SEMum is available (French *et al.*, this volume), which includes a more realistic crust and will allow us to better constrain anisotropy in the uppermost upper mantle. Upon finalizing the global inversion, our results will be compared with global dynamic models.

## 26.5 References

Gripp, A.E. and Gordon, R.G., Young tracks of hotspots and current plate velocities, *Geophys. J. Int.*, 150, 321-361, 2002.

Lee, C.T., Geochemical/petrologic constraints on the origin of cratonic mantle. in *Archean Geodynamics and Environments*, pp. 89-114, eds. Benn, K., Mareschal, J. C. and Condie, K. C. American Geophysical Union Monograph, Washington, 2006.

Lekic, V. and Romanowicz, B., Inferring upper-mantle structure by full waveform tomography with the spectral element method, *Geophys. J. Int.*, 185, 799-831, 10.1111/j.1365-246X.2011.04969.x, 2011.

O'Reilly, S.Y. and Griffin, W.L., Imaging global chemical and thermal heterogeneity in the subcontinental lithospheric mantle with garnets and xenoliths: Geophysical implications, *Tectonophysics*, 416, 289-309, 2006.

Romanowicz, B. and Yuan, H., On the interpretation of SKS splitting measurements in the presence of several layers of anisotropy, *Geophys. J. Int.*, 2011.

Yuan, H. and Romanowicz, B., Lithospheric layering in the North American craton, *Nature*, 466, 1063-1068, 10.1038/nature09332, 2010.

Yuan, H., Romanowicz, B., Fischer, K.M. and Abt, D., 3-D shear wave radially and azimuthally anisotropic velocity model of the North American upper mantle, *Geophys. J. Int.*, 184, 1237-1260, 10.1111/j.1365-246X.2010.04901.x, 2011.

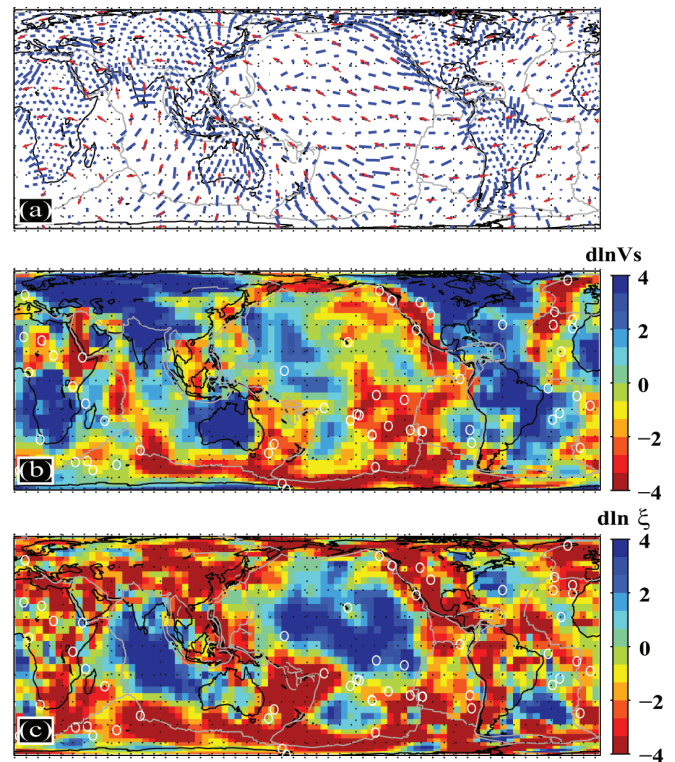


Figure 2.56: Preliminary results of our global inversion at 150 km. (a) Azimuthal anisotropy. Blue bars show the anisotropy strengths and fast axis directions. Red arrows are APM directions (HS3-NUVEL 1A). Continents are outlined in black and plate boundaries shown in gray. (b) Isotropic Vs variations. White circles are hotspots. Note at this depth thick cratons beneath North and South America, Australia, west and south Africa, India and most of Eurasia. High velocities are visible beneath the >150Ma west Pacific and north-west Atlantic regions. (c) Radial anisotropy  $\xi$  variations. Note significant positive  $\xi$  anomalies in the western-central Pacific and the Indian/western Australia plates, which correlate with the large azimuthal anisotropy strength in (a).

## 27 Refining the Cratonic Upper Mantle Using RegSEM

Huaiyu Yuan, Paul Cupillard and Barbara Romanowicz

### 27.1 Introduction

Our regional tomographic model has revealed a rapid change of anisotropic directions at middle depth in the North American craton (Yuan and Romanowicz, 2010). Intriguingly, shear wave receiver functions also report a bright negative velocity gradient in this depth range for many of the cratonic stations (Abt et al., 2010; Fischer et al., 2010). This negative velocity gradient, referred to as the mid-lithospheric-discontinuity (MLD; Fischer et al., 2010) is also found in other continents (e.g., Ford et al., 2010) and may reflect a global feature associated with the shear wave velocity drop around 100 km (Thybo, 2006; Romanowicz, 2009). Further exploring the nature of this mid-lithospheric boundary, and better constraining the absolute values of shear velocities of the lithospheric layers therefore becomes a timely endeavor when the Transportable Array (TA) sweeps the continental US.

The TA coverage in the middle and eastern parts of the continent also opens up an opportunity to address a fundamental aspect of the North American continent's formation, i.e. the welding and growing processes. This portion of the continent is overall characterized by high velocities indicating less deformed cratonic upper mantle, although it was the site of very unique episodes in the history of the creation of the North American continent: e.g. the 1.92-1.77 Ga Trans-Hudson orogeny represented the plate collision between Archean Wyoming and Superior, analog to the present day Himalayas; the 1.71-1.68 Ga Yavapai and 1.70-1.65 Mazatzal Orogeny represented the accretional addition of juvenile volcanic arcs to the cratonic core (Hoffman, 1988), and to the east, the 1.1 Ga

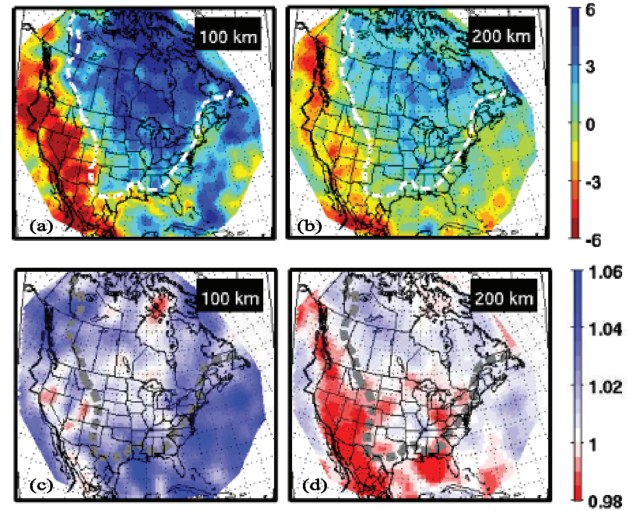


Figure 2.58: Preliminary results for the first iteration inversion for  $V_s$  and  $\xi$ . Top, isotropic velocity  $V_s$  variations with respect to SEMum global average at 100 and 200 km (a and b). White line demarcates the cratonic region. Bottom, radial anisotropy  $\xi$  variations with respect to isotropy. Craton boundary is shown in dashed gray.

Grenville and 260 Ma Appalachian Orogeny marked the formation and breakup of super continents Rodinia and Pangea (Thomas, 2006). A hypothesis to test is whether the signature of the distinct continent assembling processes may have been frozen in and well preserved in the crust and upper mantle. High resolution isotropic and anisotropic shear wave velocity tomography images may help address this question.

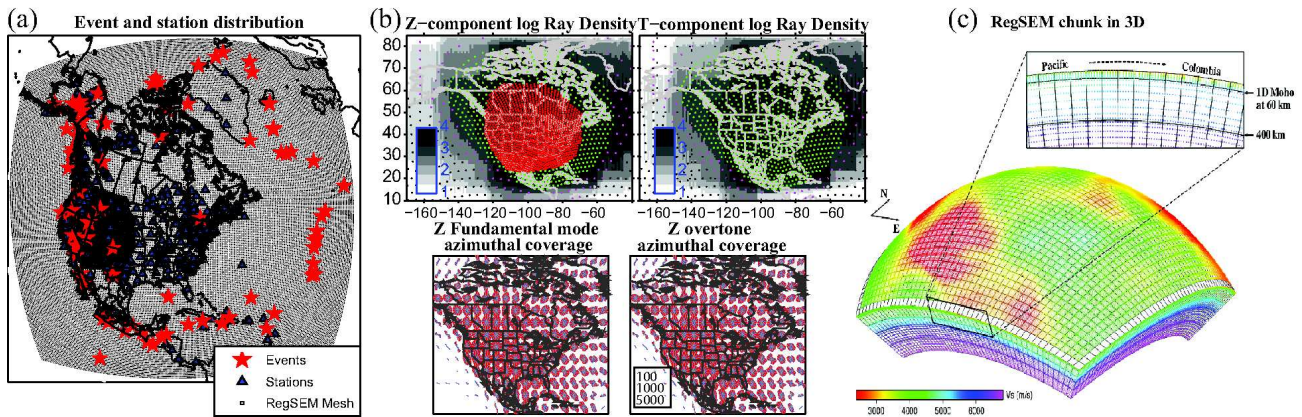


Figure 2.57: (a) RegSEM inversion setup. (a) Local and Regional events (red stars), broadband stations (black triangles) and RegSEM mesh (dotted background). (b) Ray density and azimuthal coverage for Z- and T-component and fundamental mode and overtones. (c) RegSEM mesh for 60-km crust and upper mantle used in the current inversion. The S-wave speed at each GLL point on the vertical and horizontal borders of the domain is plotted. A zoom into the upper part of the model shows the Moho and 410-km discontinuities.

## 27.2 RegSEM Inversion

We conduct a refined 3D tomographic inversion of the cratonic North American upper mantle. The new inversion utilizes shorter period waveforms (down to 40 s) from over 100 local and regional events (Figure 2.57) to improve both horizontal and vertical resolution, and a regional Spectral Element code, RegSEM (Cupillard *et al.*, 2011) to compute the forward synthetics. RegSEM includes ellipticity, attenuation, arbitrary anisotropy, and non-conformal mapping of discontinuities, and can accurately represent scattering and focusing/defocusing effects caused by the 3D Earth structure. We apply a hybrid iterative inversion approach that uses accurate RegSEM synthetics and approximate but computationally efficient 2D finite frequency kernels based on NACT normal model perturbation theory (Li and Romanowicz, 1995). We also test a much more time-consuming but accurate inversion scheme in which we consider Frechet kernels computed using RegSEM and the adjoint formalism.

A good crust model is essential in all SEM simulations. By combining a suite of 1D and 3D crust models with several North American upper mantle velocity models, we compare with real data the RegSEM simulations to evaluate effects of different types of crust models. Starting models are selected based on waveform fits to both Z- and T-component data waveforms. In this inversion, we choose the Berkeley global model SEMum (Lekic and Romanowicz, 2011), in which a homogenized 60-km uniform crust (thickness compensated by radial anisotropy; Backus, 1962) is used to speed up the SEM simulations.

We parameterize our model space with a range of 100-400km horizontal nodes (Figure 2.58bc) according to the ray path coverage. The inversion problem is then solved iteratively: 1) compute RegSEM synthetics; 2) compute NACT partial derivative kernels; 3) invert for isotropic Vs and radial anisotropy  $\xi$  structure; 4) repeat 2)-3) due to using approximated partial derivatives kernels; and 5) repeat 1)-4) for the next iteration. Frechet kernels computed using RegSEM and the adjoint formalism will be included after obtaining stable inversions.

## 27.3 Initial Results and Ongoing Work

The iteration tomographic inversion results for Vs and  $\xi$  variations are shown in Figure 2.58a-d. The isotropic Vs images confirm the thick root of the craton down to 200 km. Along the east margin of the craton, a noticeable band of low velocity structure closely follows the Grenville/Appalachian orogens down to 100 km, indicating persistent influence of orogeny boundaries deep in the lithosphere. In contrast, the northwestern Atlantic plate shows large positive velocity perturbations, consistent with the over 150 Ma age of this portion of the oceanic lithosphere.

We are currently migrating to the second version of

our global model SEMum (French *et al.*, this volume), in which in oceans the homogenized crust is 30 km thick while in continents the crust remains of realistic thickness constrained by a fundamental mode surface wave group and phase velocity dataset (Shapiro and Ritzwoller, 2002). Upon finalizing the new RegSEM inversion for Vs and  $\xi$ , we will move on to the joint inversion of azimuthal anisotropy with both surface and body waveforms (down to 20 s) and a more robust SKS dataset.

## 27.4 References

- Abt, D.L., Fischer, K.M., French, S.W., Ford, H.A., Yuan, H. and Romanowicz, B., North American lithospheric discontinuity structure imaged by Ps and Sp receiver functions, *J. Geophys. Res.*, 115, B09301, DOI: 10.1029/2009jb006914, 2010.
- Backus, G.E., Long-Wave Elastic Anisotropy Produced by Horizontal Layering, *J. Geophys. Res.*, 67, 4427-4440, DOI: 10.1029/JZ067i011p04427, 1962.
- Cupillard, P., Delavaud, E., Burgos, G., Festa, G., Villotte, J.-P., Capdeville, Y. and Montagner, J.P., RegSEM : a versatile code based on the Spectral Element Method to compute seismic wave propagation at the regional scale, *Geophys. J. Int.*, submitted.
- Fischer, K.M., Ford, H.A., Abt, D.L. and Rychert, C.A., The Lithosphere-Asthenosphere Boundary, *Annu. Rev. Earth Planet. Sci.*, 38, 551-575, doi:10.1146/annurev-earth-040809-152438, 2010.
- Ford, H.A., Fischer, K.M., Abt, D.L., Rychert, C.A. and Elkins-Tanton, L.T., The lithosphere-asthenosphere boundary and cratonic lithospheric layering beneath Australia from Sp wave imaging, *Earth Planet. Sci. Lett.*, 300, 299-310, DOI: 10.1016/j.epsl.2010.10.007, 2010.
- Hoffman, P.F., United Plates of America, The Birth of a Craton: Early Proterozoic Assembly and Growth of Laurentia, *Annu. Rev. Earth Planet. Sci.*, 16, 543-603, DOI: 10.1146/annurev.ea.16.050188.002551, 1988.
- Lekic, V. and Romanowicz, B., Inferring upper-mantle structure by full waveform tomography with the spectral element method, *Geophys. J. Int.*, 185, 799-831, DOI: 10.1111/j.1365-246X.2011.04969.x., 2011.
- Li, X.-D. and Romanowicz, B., Comparison of global waveform inversions with and without considering cross-branch modal coupling, *Geophys. J. Int.*, 121, 695-709, 1995.
- Romanowicz, B., The Thickness of Tectonic Plates, *Science*, 324, 474-476, DOI: 10.1126/science.1172879, 2009.
- Thomas, W.A., Tectonic inheritance at a continental margin, *GSA Today*, 16, DOI: 10.1130/1052-5173, 2006.
- Thybo, H., The heterogeneous upper mantle low velocity zone, *Tectonophysics*, 416, 53-79, 2006.
- Whitmeyer, S.J. and Karlstrom, K.E., Tectonic model for the Proterozoic growth of North America, *Geosphere*, 3, 220-259, DOI: 10.1130/ges00055.1, 2007.
- Yuan, H. and Romanowicz, B., Lithospheric layering in the North American craton, *Nature*, 466, 1063-1068, DOI: 10.1038/nature09332, 2010.

## 28 Investigating Upper Mantle Discontinuities Beneath Subduction Zones

Ruiqing Zhang and Barbara Romanowicz

### 28.1 Introduction

Subduction zones can be regarded as natural laboratories because of the wide variety of processes involved. Macquarie Island is an exposed portion of the Macquarie Ridge, and is located where the Australian plate meets the Pacific plate. To its north is the Tonga trench, where the old Pacific floor subducts at a rapid rate below the Indo-Australia plate, producing a deep slab of former oceanic lithosphere.

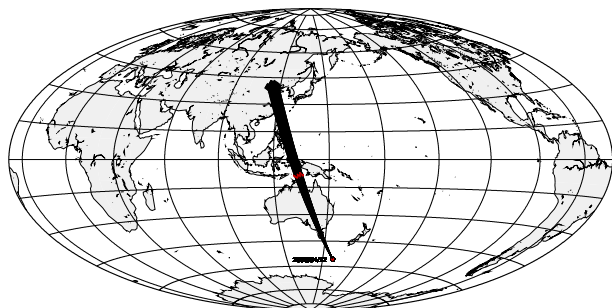


Figure 2.59: Raypath from the event to stations in the array.

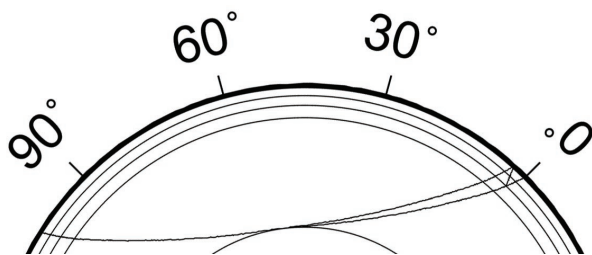


Figure 2.60: Raypaths of Sdiff and S410sSdiff.

Study of seismic velocity anomalies in the transition zone (TZ) is an approach to investigating variations in temperature or petrology. Travel time tomography shows that the Pacific plate deflects in the transition zone (between about 400 and 700km depth) before continuing into the lower mantle beneath the Tonga trench. However, beneath the Kermadec Trench, penetration into the lower mantle occurs without a link (*Van der Hilst, 1995*). Moreover, the depth observations of the 410 and 660-km discontinuities, which are sensitive to temperature, also provide a reference point for investigating properties of the transition zone. The receiver function has become a commonly used tool for constraining the depth of the

upper mantle discontinuities. However, due to the limitation of recording stations installed in the oceans, it seems difficult to constrain the depth of discontinuities beneath subduction zones.

### 28.2 Data and preliminary results

From 2006 to 2009, a 150 station broadband seismic array (Figure 2.59) was deployed in north China by the Institute of Geophysics, China Earthquake Administration (CEA). Figure 2.61 is a high quality seismic profile of a shallow event (16 km depth) with a magnitude of  $M_w$  7.2 which occurred in Macquarie Ridge, recorded by the CEA array. The epicentral distance is from about  $99\sim 105^\circ$ .

In the distance range larger than  $100^\circ$ , SS precursors should be observed. Considering the location of the event and seismic array shown in Figure 1, the corresponding SS bounce points mainly sample the Arafura Basin between Papua New Guinea and the Australian Gulf of Carpentaria. It is common to map discontinuity topography by constraining the relative travel time between the S660S (S410S) and the reference SS phase. Because precursor phases have amplitudes that are typically  $\sim 5\text{-}10\%$  (or less) of the amplitude of the SS phase, stacking of data is required to bring the precursors out of the background noise (*Schemerr, 2006*).

Figure 2.61 is a seismic profile of SS precursors (band-pass filtered between  $20\sim 100$ s), in which the maximum amplitude of SS in each record has been normalized and the timing of the peak is defined with a reference time of zero. From Figure 2.61, it can be seen that precursors of S660S ( $-200$ s) and S410S ( $-150$ s) are relatively difficult to identify, compared with the S210S ( $-70$ s) precursor.

It should be noted that in Figure 2.61, there is a phase in the time window of about  $-250$ s, with a relatively high signal-to-noise ratio and which can be clearly observed across the whole seismic profile. It is suggested by Taup that this is the S410sSdiff phase. The S410sSdiff phase is the upside reflection from the 410km discontinuity beneath the source region (Figure 2.60). It is surprising that S410sSdiff is so clearly observed.

### 28.3 Future work

1. Stacking methods – enhancing the signals of S660S (S410S): How to increase the signal of the precursors of interest is a challenge. In future research, we want to use a phase weighted stack (*Schimmel, 1997*).

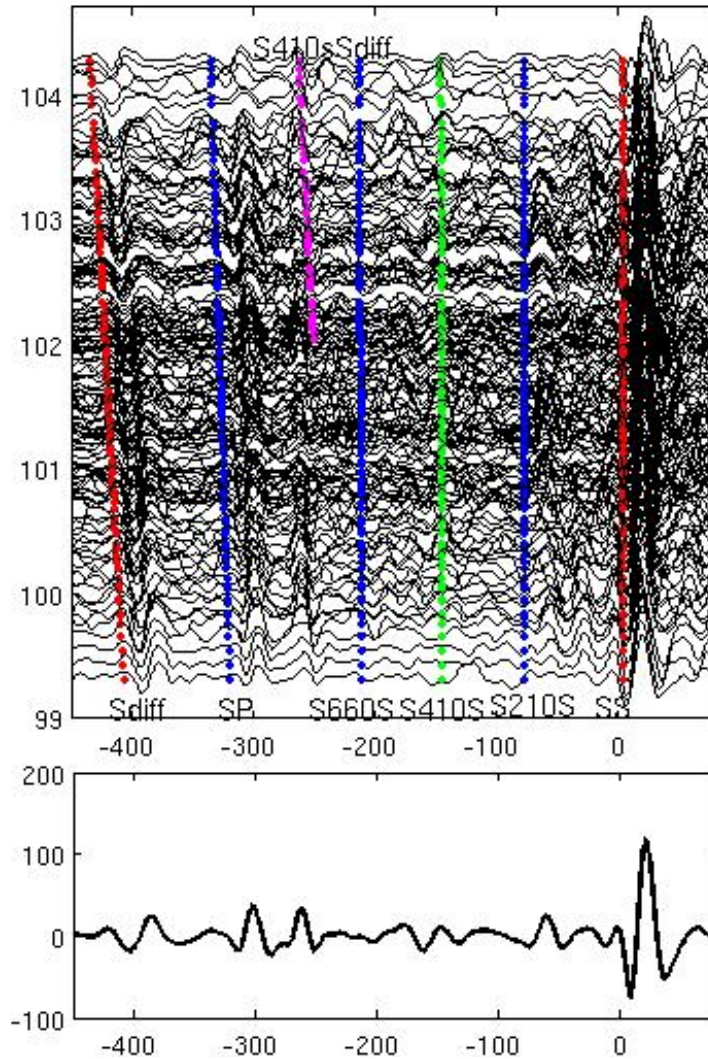


Figure 2.61: Top: Seismic profile of SS precursors with predicted traveltime of the IASP91. Bottom: Stacked data using the SS phase as a reference.

2. Mapping the 410-km discontinuity beneath Macquarie Ridge: In the future, we will focus on how to use the relative time difference between the Sdiff and S410sSdiff to constrain the depth of 410-km discontinuity beneath Macquarie trench.

## 28.4 References

Schmerr, N., and E. Garnero, Investigation of upper mantle discontinuity structure beneath the central Pacific using SS precursors, *J. Geophys. Res.*, **111**, doi:10.1029/2005JB004197, 2006

Van der Hilst, R.D, Complex morphology of subducted lithosphere in the mantle beneath the Tonga trench, *Nature J.*, **374**, 154-157, 1995.

Schimmel, M. and Paulssen, H. Noise reduction and detection of weak, coherent signals through phase-weighted stacks. *Geophys. J. Int.*, **130**, 497-505, 1997

## 29 Small-scale Variation of SS Precursors Observed by US Transportable Array

Zhao Zheng and Barbara Romanowicz

### 29.1 Introduction

SS precursors are the underside reflections from the upper mantle discontinuities (400 and 670 primarily) at half distance. They have almost identical ray paths as SS except in the vicinity of the bounce point; therefore their differential travel times (with reference to SS) and amplitudes provide ideal constraints on the discontinuity topography and the impedance contrast across it. They have been extensively used to investigate the discontinuities, mainly on the global scale (for a review, see *Deuss, 2009*) but also in regional studies if there is enough coverage (e.g. *Schmerr and Garnero, 2006; Cao et al., 2011*).

SS precursors are usually at or below noise level. Therefore, they are difficult to identify on individual seismograms. In most previous studies, stacking (including non-linear) techniques are employed to bring out a clear phase, which results in robust travel time measurements. The amplitude information, however, is usually distorted or lost after stacking. In addition, constrained by data

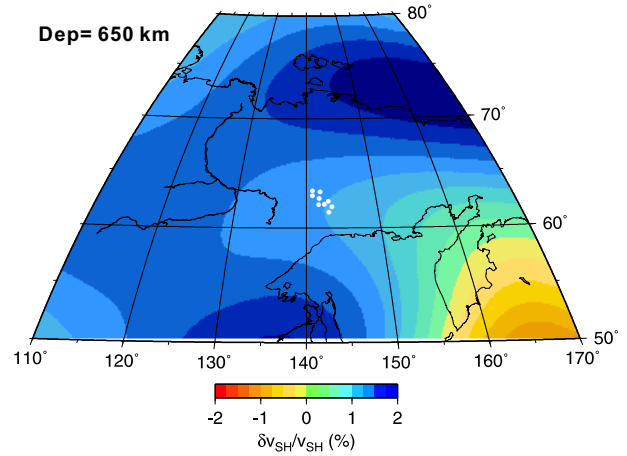


Figure 2.63: A map view of the 3D model S362ANI (*Kustowski et al., 2008*) in the study region at a depth of 650 km.  $V_{SH}$  is plotted as relative perturbation to the 1D reference model STW105 (*Kustowski et al., 2008*). The white circles represent the locations of precursor bounce points of the stations shown in Figure 2.62.

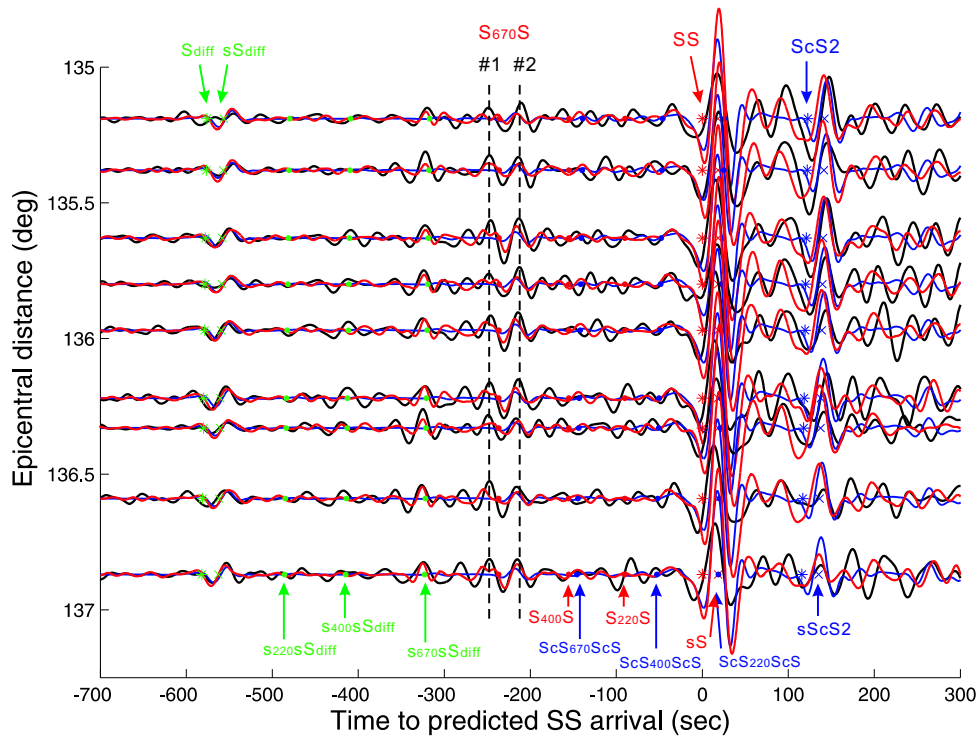


Figure 2.62: Transverse component waveforms of stations with azimuth  $i20-23^\circ$  and distance in  $135-137^\circ$ : data (black lines), 1D (blue) and 3D synthetics (red). All traces are normalized to a common factor. PREM predicted arrivals are labeled with colored arrows. The two phases associated with S670S are marked out by dash lines.

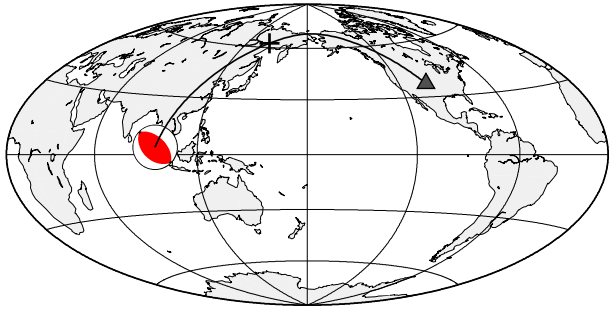


Figure 2.64: SS ray path from a shallow event ( $m_b$  6.7; depth 38 km) to a station (T28A) in the US Transportable Array. The location of the bounce point is denoted by a cross.

coverage, the bin size for stacking is usually 10 or 5° in radius at best, putting a limit on the resolution.

## 29.2 Data

Owing to the high quality recordings from the US Transportable Array (TA), it is now feasible to identify clear and coherent SS precursors on individual seismograms across a distance profile, allowing resolution for small-scale lateral variations in discontinuity characteristics. As a rule of thumb, if the station interval in the array is  $\sim 70$  km, the interval between bounce points is half of that, i.e.  $\sim 35$  km.

In this study, we show the observation from an  $m_b$  6.7 event that occurred in Northern Sumatra, whose SS bounce points of the TA stations sample the northern coast of Okhotsk Sea (Figure 2.64), a previously understudied location. A tomographic study of this region has revealed two subducted slabs sinking into the transition zone and ponding at the 670 discontinuity (Gorbatov *et al.*, 2000). For this event, we collect broadband waveforms from the IRIS data center, rotate (here we look at transverse component only), remove instrument response, integrate to displacement, bandpass filter 20-100 seconds (shorter periods are also tried), and visually inspect trace by trace to exclude the noisy waveforms. We then bin the array data by azimuth and epicentral distance of 2-3°. Within each bin, there are approximately 10 traces of high quality. Figure 2.62 shows the record section (observed traces plotted in black lines) of one such bin. It is not possible to discuss all the interesting observations in this short report; here we focus on S670S. The most striking feature is the large amplitude (on the order of the main phases) of this precursor throughout the profile. In addition, two pulses can be identified around the predicted S670S arrival time.

## 29.3 Modeling

We try to model the observations with synthetic seismograms from 1D and 3D earth models. The 1D synthetics are computed for PREM (Dziewonski and Anderson, 1981) by normal mode summation, accurate at periods  $>10$  seconds. The 3D synthetics are made available from the Global ShakeMovie project of Princeton University (<http://global.shakemovie.princeton.edu>). In that simulation, the Earth model is S362ANI (Kustowski *et al.*, 2008) for the mantle plus Crust2.0 (Bassin *et al.*, 2000); the Spectral Element Method (SEM) is used; and the synthetics are accurate between 17 and 500 seconds (Tromp *et al.*, 2010).

Figure 2.62 shows the 1D (blue) and 3D (red) synthetics plotted against observations (black), with emphasis on S670S. The 1D synthetics fail by far to reproduce the precursor observations. In particular, they fail to model the first one of the two S670S arrivals. The 3D synthetics, on the other hand, are able to model the precursor waveforms much better. However, even the 3D synthetics are unable to fully reproduce the large S670S amplitude observed. To explain the remaining discrepancy may require focusing effects caused by complex geometry of the slab interacting with the 670 discontinuity. A map of  $V_{SH}$  perturbation at 650 km is shown in Figure 2.63. It is interesting to notice that the precursor bounce points of these stations fall in a "valley" between two strong high velocity anomalies, which might serve to focus the precursor energy. A thorough investigation of the 3D model is necessary in order to fully understand what structure enables the improvement with respect to the 1D model in fitting the precursor observations.

## 29.4 References

- Bassin, C., G. Laske and G. Masters, The current limits of resolution for surface wave tomography in North America, *EOS, Trans. Am. Geophys. Un.*, **F897**, 81, 2000.
- Cao, Q. et al., Seismic Imaging of Transition Zone Discontinuities Suggests Hot Mantle West of Hawaii, *Science*, **332**, 1068, 2011.
- Deuss, A., Global observations of mantle discontinuities using SS and PP precursors, *Surv. Geophys.*, **30**, 301-326, 2005.
- Dziewonski, A. and D. Anderson, Preliminary reference Earth model, *Phys. Earth Planet. Inter.*, **25**, 297-356, 1981.
- Gorbatov, A. et al., Signature of remnant slabs in the North Pacific from P-wave tomography, *Geophys. J. Int.*, **142**, 27-36, 2000.
- Kustowski, B., G. Ekstrom, and A. Dziewonski, Anisotropic shear-wave velocity structure of the Earth's mantle: a global model, *J. Geophys. Res.*, **113**, 2008.
- Tromp, J. et al., Near real-time simulations of global CMT earthquakes, *Geophys. J. Int.*, **183**, 381-389, 2010.

## 30 Investigation of Cascadia Segmentation with Ambient Noise Tomography

Robert W. Porritt and Richard M. Allen

### 30.1 Introduction

Several lines of evidence suggest that simple subduction with one downgoing and one overriding plate is an insufficient model of the Cascadia Subduction Zone. Instead, the subduction zone and arc are segmented, exhibiting variations in multiple characteristics along strike. One line of evidence comes from the analysis of seismicity. The subduction zone is atypical everywhere in that the Wadati-Benioff zone is sparsely defined and shallow. There are a few subduction interface events deeper than the continental crust at the northern and southern ends of the subduction zone in Washington and California, but only to 75km depth. However, there are almost no sub-crustal (>30km depth) earthquakes beneath Oregon. In contrast, Episodic Tremor and Slip (ETS) events have been mapped throughout the subduction zone (*Brudzinski and Allen, 2007*). The recurrence rate of ETS, consisting of many non-volcanic (or tectonic) tremors at the same time as geodetically measured back-slip, varies along strike with similar segment boundaries as observed by the variation in seismicity and topography.

Other evidence for segmentation along the arc comes from the composition of arc volcanism. Detailed analysis of primitive basalt families in the main volcanic arc reveals variable mantle domains and melting regimes attributed to the effects of the slab window to the south, impingement of the Basin and Range terrain, and interaction with the Siletzia Terrane (*Schmidt et al., 2008*). In addition, measurements of total heat production from volcanic fumaroles, thermal springs, and slightly thermal springs (*Ingebritsen and Mariner, 2010*) show significantly higher total heat production in the southern part of the arc where Basin and Range extension is thought to create permeable zones in the crust (*Ingebritsen and Mariner, 2010*).

### 30.2 Data Processing

Our dataset focuses on two Flexible Array experiments, FlexArray along Cascadia Experiment for Segmentation (FACES) and the Flexible Array Mendocino Experiment (Mendocino), while also including data from the Berkeley BDSN, Canadian Seismic Network, USArray Transportable Array, and the Advanced National Seismic System (ANSS) backbone seismic network. The dataset extends temporally from July 2007 through September 2010. While we focus on the Pacific Northwest, the dataset extends spatially throughout the entire

United States with some coverage in Canada.

Detailed processing flow for computing phase velocity maps can be found in *Benson et al. (2007)* and the updates applied here are described in *Porritt et al. (in press)*.

### 30.3 Implications for tremor

*Brudzinski and Allen (2007)* identify a variation in the recurrence interval of ETS along the arc with a recurrence interval of 14 months in the north, 20 months in the center, and 11 months in the south. The cross section in Figure 2.65 is constructed by extracting the velocity values along a profile aligned to the 30 km slab contour from *Audet et al. (2010)*, which is thought to represent the up-dip limit of ETS. Superimposed on this image are the long-term ETS segmentation boundaries at 43°N and 46.7°N (*Brudzinski and Allen, 2007*). These boundaries, based on the recurrence interval for ETS events, are aligned with both the location of the high velocity Siletzia Terrane in the mid-crust (15 km depth) and also the deeper three-way segmentation in the subducting oceanic lithosphere between the Gorda, Southern Juan de Fuca, and Northern Juan de Fuca at 60-120 km depth. Thus the segmentation of ETS is aligned with structural boundaries in both the continental crust and the subducting oceanic lithosphere.

### 30.4 Implications for volcanic activity

Figure 2.66 shows a set of observations along the axis of the Cascades volcanic range. Figure 2.66a is modified from *Ingebritsen and Mariner (2010)* showing cumulative heat production from the north to the south. Comparing this to PNW10-S shows a strong correlation between the high heat production south of 45°N and a large zone of low velocities between 40.5°N and 45°N. The extension of the Basin and Range, and the associated clockwise rotation of the Cascadia margin, could explain the lower velocities in the southern half of the subduction zone at all depths (Figure 2.66c; anomalies SM1, SM2, and SM5). The rotation leads to extension at the southern end, which promotes melting and results in the larger low velocity zone. The center of this low velocity zone is also located at the slab segmentation boundary (at 43°N, Figure 2.66c, anomaly SM5) associated with the continuation of the Blanco Fracture Zone separating the Gorda and Juan de Fuca portions of the plate.

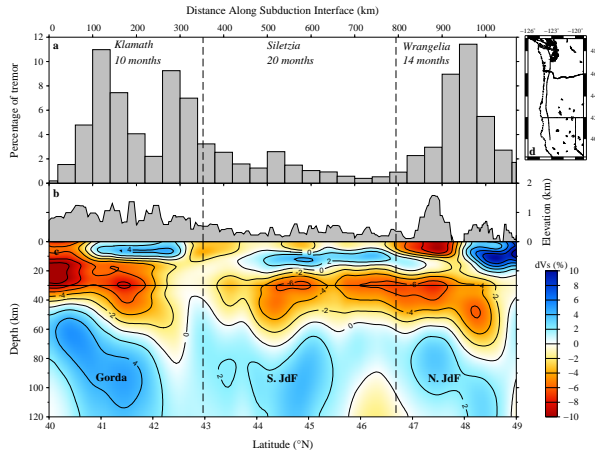


Figure 2.65: Fence diagram along the 30km slab contour as defined by *Audet et al.*, 2010. Panel (a) is the distribution of tremor from *Boyarko and Brudzinski*, 2010. Panel (b) is the topography along the profile. Panel (c) is the relative velocity extracted from PNW10-S and panel (d) gives the location in map view. Panel (a) labels the 3 segmented zones based on the tremor recurrence with their given recurrence interval. Panel (c) labels the high velocity centers of the Gorda, Southern Juan de Fuca, and Northern Juan de Fuca slabs.

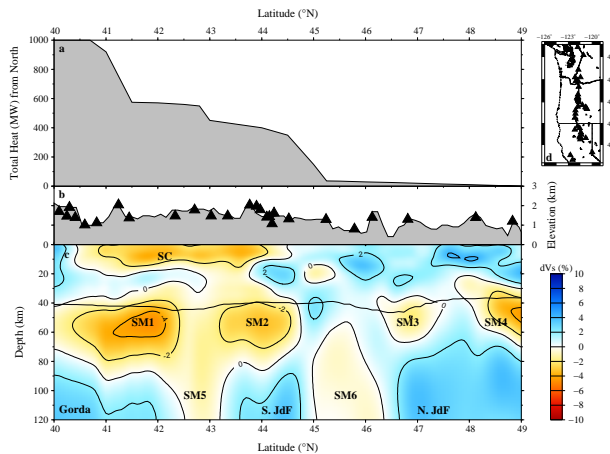


Figure 2.66: Fence diagram comparing PNW10-S with heat production measured in *Ingebritsen and Mariner*, 2010. Panel (a) is cumulative heat production from north, panel (b) shows the topography with volcanic centers (black triangles), panel (c) is the structure along the arc, and panel (d) gives a reference location for the profile. Thick black line in (c) is the Moho. Major anomalies are labeled as: SC- slow crust; SM1-6 - low velocity mantle anomalies; Gorda - Gorda plate; S. JdF and N. JdF - south and north Juan de Fuca plates, respectively.

### 30.5 Acknowledgements

We would like to acknowledge our co-PIs and collaborators on the flexible array experiments. The Mendo-

cino Broadband Experiment was made possible through NSF grants EAR0643392 and EAR0745934, with help from Gene Humphreys, Leland O'Driscoll, Alan Levander, and Yongbo Zhao for fieldwork and discussions. The FlexArray Along Cascadia was funded through NSF grant EAR0643007 with co-PI Mike Brudzinski and his students Devin Boyarko and Stefany Sit.

Data from this study came from the Earthscope US-Array/Transportable Array, the Canadian National Seismic Network through the AutoDRM system, the Berkeley Digital Seismic Network, and the Southern California Earthquake Center.

This work has been made possible with the resources available through the PASSCAL instrument center at New Mexico Tech.

### 30.6 References

Audet, P., Bostock, M. G., Boyarko, D. C., Brudzinski, M. R., and Allen, R. M., Slab morphology in the Cascadia forearc and its relation to episodic tremor and slip, *Journal of Geophysical Research*, *115*, B00A16, 2010.

Benson, G.D., Ritzwoller, M.H., Barmin, M.P., Levshin, A.L., Lin, F., Moschetti, M. P., Shapiro, N.M., Yang, Y., Processing seismic ambient noise data to obtain reliable broadband surface wave dispersion measurements. *Geophysical Journal International*, *169*, 1239-1260, 2007.

Boyarko, D. C. and Brudzinski, M. R., Spatial and temporal patterns of nonvolcanic tremor along the southern Cascadia subduction zone. *J. Geophys. Res.*, *115*, B00A22, DOI:10.1029/2008JB006064, 2010.

Brudzinski, M. and Allen, R. M., Segmentation in Episodic Tremor and Slip All Along Cascadia. *Geology*, *35*(10) 907-910, 2007.

Ingebritsen, S. E., and Mariner, R. H., Hydrothermal heat discharge in the Cascade Range, northwestern United States, *Journal of Volcanology and Geothermal Research*, *196*(3-4), 208-218, 2010.

Levander, A., Niu, F., Miller, M.S., Zhai, Y. and Liu, K., USArray Receiver Function Images of the Lithosphere in the Western U.S., *EOS Trans. AGU* *82*(52), Fall Meet. Suppl., Abstract S44B-01, 2007.

Obrebski, M., Allen, R. M., Xue, M., Hung, S-H., Slab-plume interaction beneath the Pacific Northwest, *Geophys. Res. Letters*, *37*, 114305, 2010.

Porritt, R. W., Allen, R. M., Boyarko, D. C., and Brudzinski, M. R., Investigation of Cascadia Segmentation with Ambient Noise Tomography, *EPSL*, accepted, 2011.

Pollitz, F. F., Observations and interpretation of fundamental mode Rayleigh wave-fields recorded by the Transportable Array (USArray), *J. Geophys. Res.*, *113*, B10311, 2008.

Schmidt, M. E., Grunder, A.L., and Rowe, M., Segmentation of the Cascades Arc as indicated by Sr and Nd isotopic variation among primitive basalts, *Earth and Planetary Science Letters*, *266*, 166-181, 2008.

# 31 Characterization of the Pacific Superplume Boundary

Sanne Cottaar and Barbara Romanowicz

## 31.1 Introduction

The lowermost lower mantle, also called the D<sup>''</sup>, is a thermo-chemical boundary layer, exposing many intriguing observations. Global tomography of shear velocities show strong degree 2 and 3, dominated by two large low shear velocity provinces (LLSVP): one under Africa and one under the Pacific. Local studies show that the boundaries of these superplumes are sharp, sharper than can be explained by temperature variations. Another complication of the D<sup>''</sup> is the occurrence of localized ultra-low velocity zones (ULVZ), suggesting the possible presence of partial melt and/or iron enrichment.

## 31.2 Data and observations

Data is collected for recent events in Southeast Asia towards the Transportable Array in the USA. The main event studied is a  $M_w$  6.6 and 414 km deep event on the 20th of March 2010 in New Ireland Region, Papua New Guinea. Paths of this event towards the Transportable Array and other arrays in the USA travel on both sides of the Pacific LLSVP boundary. The radiation pattern of the main event is opportune, with strong non-nodal SH amplitudes in the azimuthal direction covered here. Amplitudes in the favorable radiation pattern decrease slightly towards the south, but less significantly than the data shows. The strong decrease in amplitude and wave broadening occurs as the paths to the south cross into the Pacific mantle plume. Center points for ScS and Sdiff for all events are plotted in Figure 2.67 and for some waveforms in Figure 2.68.

The striking observation is the occurrence of a post-cursor, most visible for periods between 10 and 20 seconds. The post-cursors are delayed by more than 30 seconds for the southernmost stations and move out to almost 50 seconds for stations around the plume boundary, as can be seen in the waveforms in Figure 2.68. The occurrence and move-out of the phase is mainly a function of azimuth, and there is little variation in timing with distance. The ratio in amplitude between post-cursor and main phase does increase with distance. For the further diffracted phases, the post-cursor becomes stronger than the main phase. Two additional events with less coverage but similar features can be found in *Toh et al.*, 2011.

Additionally, the SVdiff waveforms are stronger outside of the superplume. Future work will concentrate on constraining anisotropic behavior across the superplume boundary to explain these observations. The P-wave arrivals also show delay and wave broadening towards the south, although this is less significant. This can constrain

the  $V_p/V_s$  ratios across the boundary, and will be part of future work.

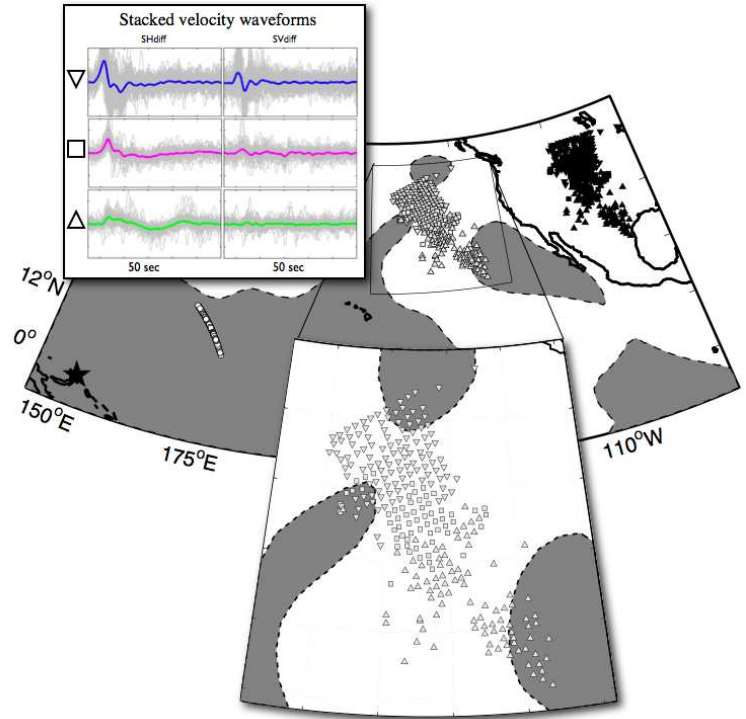


Figure 2.67: Location of clusters and stacked waveforms for each cluster.

## 31.3 Clustering

Clustering the waveforms provides an objective way to bin the data. We choose a 60 s window around the predicted arrival time of Sdiff for PREM. The measure of coherence is the correlation between the two waveforms. We apply hierarchical clustering with complete linkage (see Matlab manual). Initially, each waveform is considered a single cluster, which is then combined stepwise for the highest correlation. For each new cluster, the correlation to other clusters is defined by the minimum correlation between two waveforms from each cluster. This is repeated until three significant clusters remain. Results for the clustering are shown by the symbols in Figure 2.67. Clear clusters that vary with azimuth also result for ScS, sSdiff and Pdiff waveforms for the same event. This method has also proven to work for rays traveling parallel to the African plume boundary, while waveforms

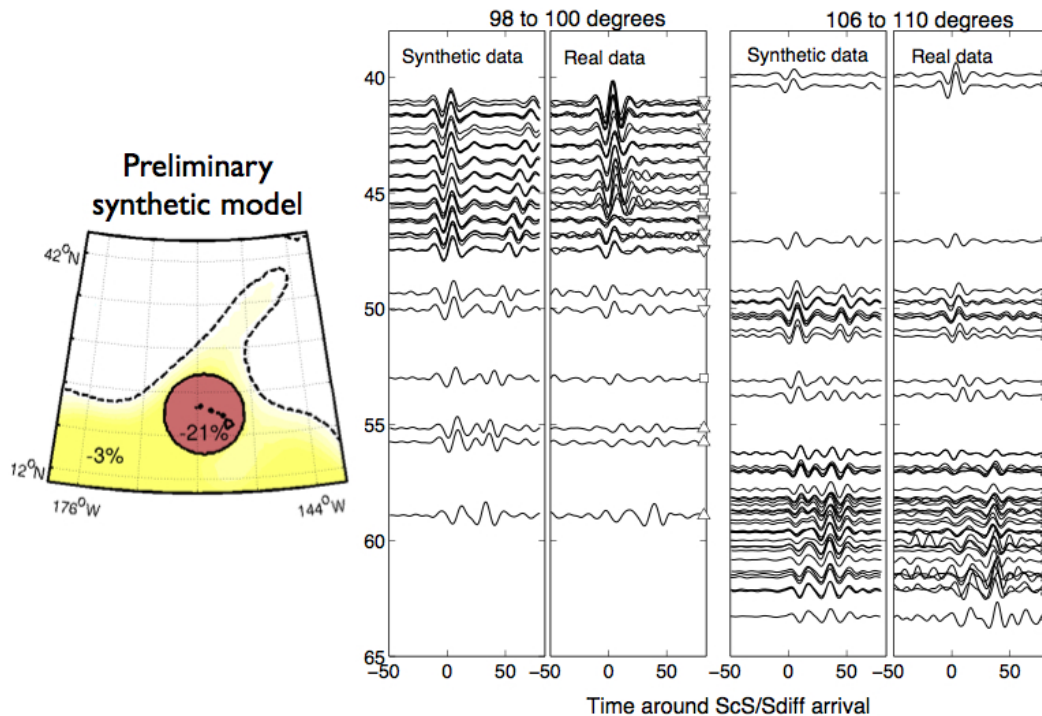


Figure 2.68: Preferred ULVZ input model, and synthetic data next to real data, filtered between 10 and 22 seconds. Symbols next to the real waveforms denote the clusters shown in Figure 2.67

cluster as a function of distance for rays that travel solely outside of the superplume.

### 31.4 Forward modeling

Synthetic data are forward modeled using a sandwiched version of CSEM (Coupled Spectral Element Method, *Capdeville et al.*, 2003). This method is computationally effective, solving only for the full 3D model, which can include sharp boundaries and anisotropy, in the lowermost part of the mantle and coupling to a normal mode solution for a 1D model in the rest of the Earth. The data can constrain the best fitting model by comparing observed and synthetic full waveforms. Based on the move-out of the postcursors, we rule out that the main boundary of the superplume, as defined by global S tomographic models, can be the cause. A ULVZ with a sharp velocity decrease within the superplume is required. However, with the many possible parameters and their different trade-offs, we cannot claim to find a unique solution. Waveforms for one of our (preliminary) preferred models are shown in Figure 2.68, alongside the real data. This model contains a circular ULVZ with a radius of 600 km and a shear wave velocity reduction of -21%. The height is poorly constrained.

### 31.5 Summary

Here we present a data set with several striking features. The rays from this event in Southeast Asia travel parallel to the northern boundary of the Pacific superplume up to stations in North America, making it ideal for mapping changes across the boundary. We illustrate this by objective clustering of the waveforms. SHdiff and SVdiff waveforms indicate changes in velocity, attenuation and anisotropy across the plume. Secondly, there are postcursors with a clear move-out, indicating the presence of an ULVZ on the superplume side. The superplume boundary itself is not sharp enough to cause postcursors.

### 31.6 Acknowledgements

This project is funded by NSF's CSEDI program under grant number NSF EAR-0757608.

### 31.7 References

- Capdeville, Y., B. Romanowicz, and A. To, Coupling spectral elements and modes in a spherical earth: an extension to the "sandwich" case, *Geophys. J. Int.*, 154, 44-57, 2003
- To, A., Fukao, Y., Tsuboi, S., Evidence for a thick and localized ultra low shear velocity zone at the base of the mantle beneath the central Pacific, *Earth Plan. Sci. Lett.*, 184, 119-133, 2011

## 32 An Automated Despiking Algorithm for Seismic Normal Mode Data

Shan Dou and Barbara Romanowicz

### 32.1 Introduction

The normal modes spectra of the Earth's free oscillations contain valuable information on the longest wavelength three dimensional structure of the Earth's interior. *Dahlen* (1982) first showed that the optimum record length for measuring eigenfrequencies and decay rates of normal modes using a Hanning taper is 1.1 Q cycles. Since typical modal Q values lie in the range  $10^2$  of to  $10^3$ , optimum window lengths are on the order of days to weeks. However, it is difficult even today to retrieve clean continuous time series spanning days or weeks following a large earthquake: in addition to aftershocks and other seismic events, data spikes due to transient disturbances at the station or temporary data storage failures are often unavoidable. Therefore, it is necessary to edit seismograms prior to the spectral analysis. Spikes are usually difficult to identify by existing algorithms because they have features which often are quite similar to those of real earthquake signals. The majority of conventional despiking algorithms require empirical tuning of associated parameters. The required parameter tuning often degrades the efficiency of automated algorithms, which in the end do not save much time and effort when compared with manual approaches. Hence, most despiking is done by direct manual editing, which can be a rather monotonous task, especially when one deals with a large dataset. Ideally, to be helpful, an automated despiking algorithm should not require users to manually intervene.

In this report, we describe a 3D phase space thresholding despiking algorithm which was first developed in the hydraulic engineering community and which we have adapted to our needs. The method was originally used to remove spikes from acoustic Doppler velocimeter data. It makes use of several ideas: (1) Differentiating a signal can enhance the high-frequency components (e.g. *Roy et al.*, 1999); (2) The Universal Threshold (*Donoho and Johnstone*, 1994; *Katul and Vodakovic*, 1998) provides the maximum of a white noise sequence; (3) Valid data tend to cluster into a dense cloud in a three-dimensional Poincaré map and data points lying outside that cloud should be suspected as spikes (e.g. *Abarbanel*, 1995; *Addison*, 1997). In this study, we examine the validity of the 3D phase space thresholding despiking algorithm for preparing long seismic time series for normal mode analysis. Synthetic tests shown below demonstrated that spikes can be successfully detected and removed by the 3D phase space thresholding despiking algorithm.

### 32.2 Description of the Algorithm

The process of removing spikes comprises two steps: detection and replacement. In principle, these two parts are independent of each other, but the method described here is iterative and thus a proper spike replacing approach is also important for spike detection in the subsequent iterations.

#### (a) Universal Threshold:

As mentioned in the last section, Donoho and Johnstone (1994b) introduced the Universal Threshold, which is given by

$$\lambda^U = \sigma\sqrt{2\log n}$$

where  $\sigma$  is the standard deviation of the noise sequence and  $n$  is the number of data points.

#### (b) Differentiating and Calculating the Correlation Coefficients:

We calculate first and second derivatives of the original time series  $\Delta u_i$  and  $\Delta^2 u_i$  and the associated three sets of standard deviations  $\sigma_u$ ,  $\sigma_{\Delta u}$  and  $\sigma_{\Delta^2 u}$ . The correlation coefficients between  $u - \Delta u$ ,  $u - \Delta^2 u$  and  $\Delta u - \Delta^2 u$  are calculated as follows:

$$\alpha_{u-\Delta u} = \tan^{-1}\left(\frac{\sum u_i \Delta u_i}{\sum u_i^2}\right) = 0;$$

$$\alpha_{u-\Delta^2 u} = \tan^{-1}\left(\frac{\sum u_i \Delta^2 u_i}{\sum u_i^2}\right);$$

$$\alpha_{\Delta u-\Delta^2 u} = \tan^{-1}\left(\frac{\sum \Delta u_i \Delta^2 u_i}{\sum (\Delta u_i)^2}\right) = 0;$$

#### (c) 3D Phase-Space Map:

Each set of three variables  $\{u_i, \Delta u_i, \Delta^2 u_i\}$  determines a point  $\{\rho, \theta, \phi\}$  in spherical coordinates, where  $\rho_i^2 = u_i^2 + (\sum u_i)^2 + (\sum^2 u_i)^2$ . For each pair of  $\theta, \phi$ , we can then calculate a threshold ellipsoid determined by:

$$\frac{1}{\rho_0^2} = \frac{(\sin\phi\cos\theta\cos\alpha + \cos\phi\sin\alpha)^2}{a^2} + \frac{(\sin\phi\cos\theta\cos\alpha - \cos\phi\cos\alpha)^2}{b^2} + \frac{(\sin\phi\sin\theta)^2}{c^2}$$

Where  $a = \lambda_u^U = \sigma_u\sqrt{2\log n}$ ,  $b = \lambda_{\Delta^2 u}^U = \sigma_{\Delta^2 u}\sqrt{2\log n}$ ,  $c = \lambda_{\Delta u}^U = \sigma_{\Delta u}\sqrt{2\log n}$  and  $\alpha$  is the rotation angle calculated from the correlation coefficient of  $\alpha_{u-\Delta^2 u}$ . The valid data points will then cluster inside of the threshold ellipsoids, while the data points that fall outside of the ellipsoids will be suspected as spikes.

The 3D phase-space map has been used broadly in fractal geometry and chaotic dynamics studies. In phase-space, the transient high frequency component of the time series, which is much less random, can be separated from the chaotic regime that is featured as a compact cluster that is associated with chaotic oscillations. Because the time series needs to appear random for the Universal Threshold approach to be valid, the despiking procedure is not applied to the portion of data that are recorded within the first 21 hours after the origin time of the target event, during which strong coherent energy would not have the needed apparent randomness.

**(d) Replacement:**

Windows containing spikes can be considered as having gaps in the data stream. As one can already see, the shape of the threshold ellipsoid will vary when spikes are removed from a given segment of time series. Therefore, the entire despiking procedure needs to be repeated for several iterations until the number of detected spikes goes to zero. To ensure that the data cleaning procedure is complete and avoid introducing biases, it is important to develop a replacing strategy that can preserve the low frequency mode information contained in the time series.

The Discrete Fourier Transform (DFT) can be used to interpolate any data set that exhibits a periodic behavior. It consists of dividing the input signal into its major frequencies, determining the DFT coefficients (weights of each major frequency component), and then using the DFT coefficients and the associated frequencies to re-compose the signal. This is the same process as is used for transmitting signals over telephone lines.

**32.3 Application Examples**

To explore the effectiveness of the automated despiking procedure while verifying that no significant bias is introduced during despiking, a set of spikes extracted from a noisy record is added to a raw time series free of spikes. The automated despiking algorithm is then applied on the artificially contaminated time series. We then compare the originally clean record with that obtained after applying the despiking procedure both in the time and frequency domain so as to check the preservation of the valid signal. Figure 2.69 shows the associated power spectra: The contaminated spectra (thick black line) and the post-despiking spectra (solid grey line) are plotted together. The striking effect of the added spikes is the severely elevated baseline level in the pre-despiking spectra. In Figure 2.69b, we compare the original uncontaminated power spectra (black dashed line) and the power spectra generated from the post-despiking time series (solid grey line). The fact that they are indistinguish-

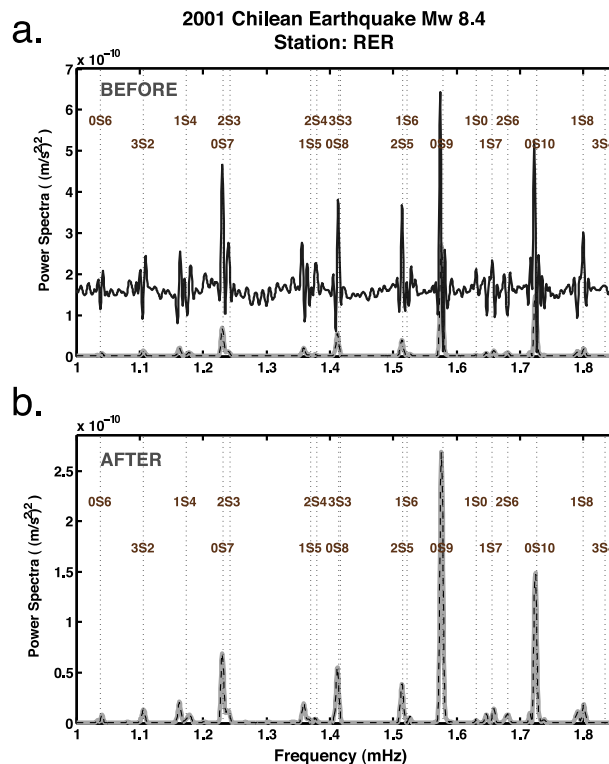


Figure 2.69: Frequency domain illustration of the effect of despiking algorithm. Panel a: The spectra shown in solid black line are generated from an artificially contaminated seismogram (i.e. clean seismogram + spikes extracted from another noisy record). Panel b: To examine whether any significant biases could be caused by the despiking algorithm, the original spectra associated with the clean seismogram are plotted (black dash line) on top of the post-despiking spectra (solid light grey line). The consistency of the two spectra indicates that valid information of the data is well maintained by the despiking algorithm. A noticeable feature is the scale differences between the two panels due to the high noise floor in Panel a.

able confirms that the despiking procedure is working well.

**32.4 References**

Donoho, D. L and Johnston, I. M., Ideal spatial adaptation by wavelet shrinkage, *Biometrika*, 81, 425-455, 1994.  
 Roy, M., Kumar, V. R., Kulkarni, B. D., Sanderson, J., Rhodes, M. and van der Stappen, M., Simple denoising algorithm using wavelet transform, *J. Am. Ins. Chem. Eng.*, 45, 2461 - 2466, 1999.  
 Abarbanel, H. D. I., *Analysis of Observed Chaotic Data*, Springer, New York, 1995.  
 Dahlen, F. A., The effect of data windows on the estimation of free oscillation parameters, *Geophys. J. R. astr. Soc.*, 69, 537-549, 1982.

# 33 Seismic Imaging of the San Andreas Fault in Northern California using Receiver Functions

Pascal Audet

## 33.1 Introduction

Scattering of teleseismic body waves is conventionally used to investigate crustal and mantle structure using the so-called “receiver function” technique. This approach makes use of the fact that teleseismic events have near-vertical incidence upon horizontally layered structure, ensuring minimum phase, and assumes that source-time functions can be approximated by energy on the  $P$  component of motion. This approach has been successful in countless applications, including the characterization of layered crust and mantle, anisotropy and dipping structure.

Results from a recent application of the receiver function method near Parkfield in Northern California suggest that crustal structure is highly anisotropic with some indication of shallow offset in crustal discontinuities across the San Andreas Fault (SAF) (Ozacar and Zandt, 2009). Here we use receiver functions to analyze crustal structure around the SAF near San Juan Bautista in Northern California by decomposing radial and transverse signals into first order harmonic modes. Variations of energy of the different modes with depth are then used to characterize teleseismic wave scattering from velocity contrasts across the San Andreas Fault.

## 33.2 Data and method

We use data from the broadband station SAO, located 3 km from the surface trace of the SAF. Three-component seismograms are collected for all events with  $M > 5.5$  in the epicentral distance range  $30^\circ$ - $100^\circ$ . Vertical and horizontal (both radial and transverse) components of motion are decomposed into upgoing  $P$ ,  $S_V$  (radial) and  $S_H$  (transverse) wave components. Individual single-event seismograms are processed using the receiver function method, which employs the  $P$  component as an estimate of the source to deconvolve the  $S_V$  and  $S_H$  components using a modified Wiener spectral deconvolution technique and recover receiver-side  $S$  velocity structure (Audet, 2010).

Resulting  $S_V$  and  $S_H$  receiver functions represent mostly forward-scattered  $P_S$  waves from planar discontinuities in physical properties. For horizontal layering, timing and amplitude of each converted phase constrain overlying velocity structure (depth and  $V_P/V_S$  of the overlying column) and velocity contrasts at discontinuities, respectively. For isotropic, horizontal layering, no energy is converted onto the  $S_H$  component; any energy observed on this component must therefore repre-

sent either structural heterogeneity (e.g., dipping interface), anisotropy, or both. In either case, periodic polarity reversals of converted  $S_H$  phase amplitude with back-azimuth are expected; a plane dipping layer will produce a  $1-\theta$  periodicity, whereas anisotropy may produce more complicated patterns with higher order harmonics due to various degrees of symmetry of the elastic tensor and its orientation in space.

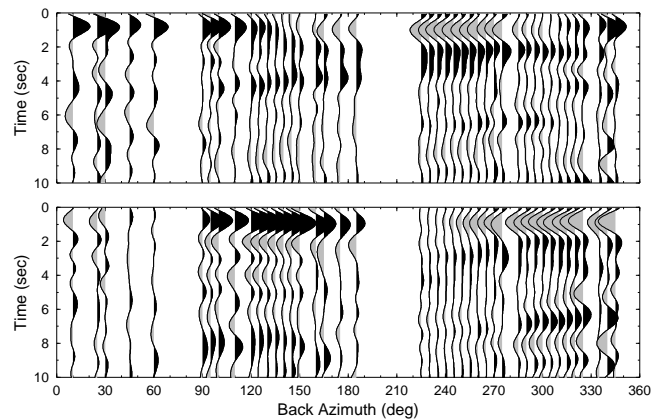


Figure 2.70: Receiver functions from station SAO near San Juan Bautista, Northern California.  $S_V$  (top) and  $S_H$  (bottom) components sorted by back-azimuth of incoming wavefield. Black is positive and grey is negative.

Results are shown in Figure 33.2. A number of features can be readily identified:

- $S_V$  signals at 1-2 seconds show strong  $1-\theta$  back-azimuthal variations in amplitude, with polarity reversals at  $130^\circ$  and  $310^\circ$ , which cannot be explained by simple, horizontal isotropic layering and must involve shallow anisotropy and/or a dipping structure.
- Corresponding  $S_H$  waves at 1-2 seconds also show similar  $1-\theta$  back-azimuthal variations, with polarity reversals shifted by 90 degrees.
- Typical crust-mantle (Moho) conversions, normally appearing at 3-5 seconds as strong positive arrivals on the  $S_V$  component of motion, are lacking, indicating that the Moho may be invisible to high-frequency waves, or that it is highly complex.

These first-order observations can be further refined by decomposing the amplitude of migrated  $S_V$  and  $S_H$  signals at each depth increment as a function of back-azimuth using the equation

$$S_{V,H}(z, \phi) = A_{V,H}(z) + B_{V,H}(z) \cos(\phi + C_{V,H}(z)). \quad (2.2)$$

For  $S_V$ , energy on the  $A$  component should reflect bulk, isotropic velocity contrasts. Any signal on the  $B$  component represents dipping or anisotropic structure, and is seen on both  $S_V$  and  $S_H$ . Higher order harmonics (not analyzed here) are diagnostic of anisotropy. The  $C$  component represents the phase of the fitted cosine function. Results are shown in Figure 33.2. The fit appears to be best between 2-6 km depth, where the  $A$  component is close to 0 on the  $S_V$  component and negligible on the  $S_H$  component. The energy arises from the purely sinusoidal terms ( $B$  and  $C$ ) on both components. Amplitudes are very high ( $<-0.5$ ), and components are  $90^\circ$  out of phase, with maximum  $S_V$  signal from back-azimuths perpendicular to strike of the SAF ( $128^\circ$  or  $308^\circ$ ). Absence of energy on the  $A$  component strongly suggests that structure other than horizontal layering is responsible. Anisotropy is also unable to explain the absence of energy on the  $A$  component, especially at the large amplitude of the  $B$  component. Instead, these signals can be easily explained by near-vertical velocity contrast of the San Andreas Fault.

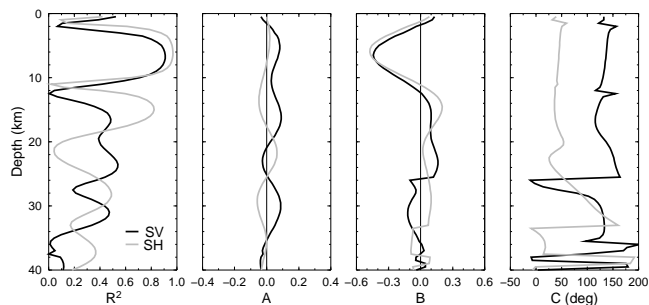


Figure 2.71: First order harmonic decomposition of receiver function amplitude as a function of inferred depth (Equation 2.2). Results for  $S_V$  and  $S_H$  are shown in black and grey, respectively.  $R^2$  shows the fit to Equation (2.2). The  $A$  component represents a constant amplitude term.  $B$  and  $C$  are amplitude and phase of a fitted cosine term.

### 33.3 Discussion and conclusion

Receiver functions for station SAO near San Juan Bautista show signals related to scattering from a near-vertical SAF. These signals indicate strong velocity contrasts, possibly related to major structural differences across the fault, or to the presence of a low-velocity zone

caused by fault damage and/or elevated pore-fluid pressure. Future work will involve modeling of these fault-scattered waves using a finite-difference technique (e.g., Levin *et al.*, 2007). In addition, the method presented here will allow characterization of time variations in fault scattering structure by analyzing residuals of the fitted Equation 2.2 as a function of time. This technique could prove to be a powerful tool for the analysis of transient fault properties following major earthquakes.

### 33.4 Acknowledgements

This work was funded by the Miller Institute for Basic Research in Science (UC Berkeley).

### 33.5 References

- Audet, P, Temporal variations in crustal velocity structure near Parkfield, California, using receiver functions, *Bull. Seism. Soc. Am.*, 100, 1356-1362, 2010.
- Levin, V., D. Okaya, and J. Park, Shear wave birefringence in wedge-shaped anisotropic regions, *Geophys. J. Int.*, 168, 275-286, 2007.
- Ozacar A. A., and G. Zandt, Crustal structure and seismic anisotropy near the San Andreas fault at Parkfield, California, *Geophys. J. Int.*, 178, 1098-1104, 2009.

